AECOM

Site-Specific Seismic Hazard Analysis

Pardee and Camanche Dams

East Bay Municipal Utility District

Project number: 60696828

July, 14, 2023

Delivering a better world

Prepared for:

East Bay Municipal Utility District

Prepared by:

Mark Dober
Senior Seismologist
T: 510-874-3085
E: mark.dober@aecom.com

AECOM
300 Lakeside Drive
Suite 400
Oakland
CA 94612
aecom.com

Table of Contents

Figures

Tables

Acronyms and Abbreviations

ASK14	Abrahamson et al. (2014)
BSS14	Boore et al. (2014)
CB14	Campbell and Bozorgnia (2014)
CR	Coast Ranges
CRGVB	Coast Ranges-Great Valley Boundary
CRSB	Coast Ranges-Sierran Block
CY14	Chiou and Youngs (2014)
DRS	Design Response Spectrum
DSHA	deterministic seismic hazard analysis
DSOD	Division of Safety of Dams
EBMUD	East Bay Municipal Utility District
FERC	Federal Energy Regulatory Commission
g	acceleration due to gravity
HID	hazard input document
km	kilometer
km/sec	kilometer per second
m	meter
M	moment magnitude
M	unspecified magnitude
m/sec	meter per second
Ma	one million years
MCE_R	risk-targeted maximum considered earthquake
M_D	duration magnitude
mm/yr	millimeter per year
NGA-West2	Next Generation of Attenuation – West (version 2)
PEER	Pacific Earthquake Engineering Research center
PGA	peak ground acceleration
PSHA	probabilistic seismic hazard analysis
R_{JB}	closest distance to surface projection of coseismic rupture
R_{RUP}	closest distance to coseismic rupture
R_X	horizontal distance from top of rupture measured perpendicular to fault strike
SA	spectral acceleration
SNGV	Sierra Nevada-Great Valley
UCERF3	Unified California Earthquake Rupture Forecast (version 3)
UHRS	uniform hazard response spectrum
USGS	United States Geological Survey
V_S	shear-wave velocity
V_{S30}	The time average shear-wave velocity over a subsurface depth of 30 m
$Z_{1.0}$	depth to Vs=1.0 km/sec
$Z_{2.5}$	depth to Vs=2.5 km/sec
WL	Walker Lane

1. Introduction

At the request of the East Bay Municipal Utility District (EBMUD), a site-specific seismic hazard analysis has been performed at the Pardee and Camanche Dams, located in the western foothills of the Sierra Nevada (Figure 1-1).

Pardee Dam and the associated Pardee Reservoir, along with Camanche Dam and Reservoir are part of the Lower Mokelumne River Project, Federal Energy Regulatory Commission (FERC) Project No. 2916-CA. The Lower Mokelumne River Project was completed in 1963-64 to provide for multiple water uses. Pardee Reservoir is operated jointly with Camanche Reservoir to maintain numerous downstream obligations, including stream-flow regulation, water for fisheries and riparian habitat, flood control, and the municipal water supply transported through EBMUD Aqueducts. Both reservoirs also provide power generation and recreation opportunities.

Pardee Dam (120.8501°W, 38.2573°N) is approximately 38 km east-northeast of Lodi (Figure 1-1). It is a curved concrete gravity structure 105 m high, plus a 2.0 m high parapet wall, as measured from the lowest level downstream toe of the dam. The crest length is 407.5 m. It is classified as a High-Hazard Dam according to FERC criteria. The dam hazard is classified as Extremely High by the California Division of Safety of Dams (DSOD).

Camanche Main Dam (121.0235°W, 38.2246°N) is approximately 24 km east-northeast of Lodi (Figure 1-1). It is a zoned compacted earthfill dam with a maximum height of 52.1 m above streambed, a crest length of 804.7 m and a crest width of 10.5 m. Camanche Dam is classified as a High-Hazard Dam according to FERC criteria. The dam hazard is classified as Extremely High by the California DSOD.

As both dams are regulated by FERC and DSOD, the hazard analysis was performed to conform with Chapter 13 of FERC's Engineering Guidelines (FERC, 2018), as well as DSOD's Inspection and Reevaluation Protocols (DSOD, 2018).

The dam sites have been and will be subjected to strong earthquake ground shaking due to their location in seismically active central California. The objectives of this analysis are to estimate the levels of ground motions that could be exceeded at specified annual frequencies (or return periods) at the dam sites based on a probabilistic seismic hazard analysis (PSHA). The PSHA methodology used in this study allows for the explicit inclusion of the range of possible interpretations in components of the seismic hazard model, including seismic source characterization and ground motion estimation. Uncertainties in models and parameters are incorporated into the PSHA through the use of logic trees. A deterministic seismic hazard analysis (DSHA) was performed for regulatory requirements and to compare against the PSHA results.

Neither FERC (2018) nor DSOD (2018) specify a return period for use in seismic design. Therefore, a large range of return periods for the uniform hazard response spectra (UHRS) have been provided (Section 5). Return periods of 144-years, the operating basis earthquake, and 950-years, the maximum design earthquake, are used by the United States Army Corps of Engineers (Engineer Regulation ER 1110-2-1806). A return period of 10,000-years, the safety evaluation earthquake, is recommended by the International Committee on Large Dams (ICOLD). FERC and DSOD rely more on the deterministic approach, with the statistical level (percentile) determined by the hazard class of the dam and/or the slip rate of the fault being considered, as discussed in Sections 5.2 and 5.4.

This seismic hazard analysis incorporates the recently developed hazard input document (HID) developed for Pardee Dam (LCI, 2020). Their characterization includes a review and update of local fault sources associated with the Foothills fault system and an updated background seismicity. A review of site-specific issues that would change the evaluations and logic tree weights adopted from the LCI (2020) report was performed and several modifications were identified and incorporated into the seismic source model as discussed in Section 4.

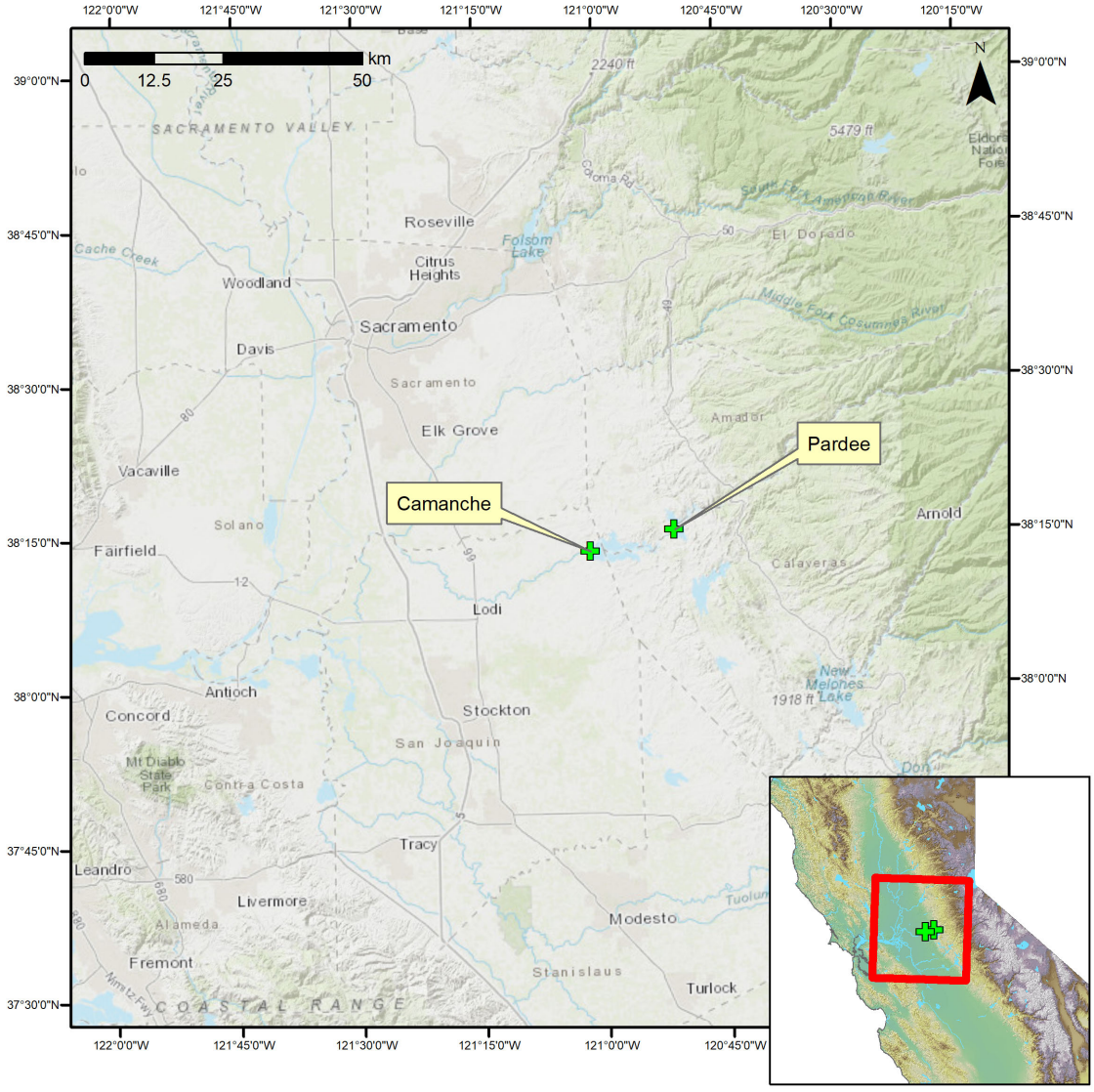

Figure 1-1. Site Location

2. Seismic Hazard Analysis Methodology

General methodologies used in the DSHA and PSHA are presented in this section.

2.1 Deterministic Seismic Hazard Analysis

The deterministic approach involves the following steps:

- Identification of the potential seismic sources that could produce ground motions of engineering significance at the site and estimation of the maximum earthquake that could reasonably be expected from these sources.
- Characterization of the seismic sources, including fault-to-site distances (rupture distance, Joyner-Boore distance), fault dip, and sense of slip. Note: In a deterministic analysis, no earthquake recurrence rate information is used, while in a PSHA, this information is essential.
- Development of the range of ground motions (median, 84th percentile) that are likely to occur at the site due to the maximum earthquake for each seismic source. As discussed in Sections 5.2 and 5.4, regulatory agencies allow for the median for low slip rate faults and requires the 84th for high slip rate faults.
- Enveloping the ground motions from each seismic source to develop the controlling maximum earthquake with the potential for generating the strongest ground motions at the site.

The first step requires a characterization of all significant seismic sources which could produce ground motions of engineering significance at the site. A description of the deterministic analysis is contained in Section 5.2 and 5.4.

2.2 Probabilistic Seismic Hazard Analysis

The probabilistic seismic hazard approach used in this study is based on the model developed principally by Cornell (1968). The occurrence of earthquakes on a fault is assumed to be a Poisson process (i.e., when a random process generates events at some average rate and the occurrence of an event does not depend on the time since the last event). The Poisson model is widely used and is a reasonable assumption in regions where data are only sufficient to provide an estimate of average recurrence rate (Cornell, 1968). When there are sufficient data to permit a real-time estimate of the occurrence of earthquakes, the probability of exceeding a given value can be modeled as an equivalent Poisson process in which a variable average recurrence rate is assumed. The occurrence of ground motions at the site in excess of a specified level is also a Poisson process if (1) the occurrence of earthquakes is a Poisson process, and (2) the probability that any one event will result in ground motions at the site in excess of a specified level is independent of the occurrence of other events.

The probability that a ground motion parameter "*Z*" exceeds a specified value "*z*" in a time period "t" is given by:

$$p(Z > z) = 1 - e^{-\nu(z)\cdot t} \qquad (1)$$

where:

$\nu(z)$ = the annual mean number (or rate) of events in which *Z* exceeds *z*.

It should be noted that the assumption of a Poisson process for the number of events is not critical. This is because the mean number of events in time t, $\nu(z)$•t, can be shown to be a close approximation on the probability p(*Z* > *z*) for small probabilities (less than 0.10) that are generally of interest for engineering applications. The annual mean number of events is obtained by summing the contributions from all sources, that is:

$$\nu(z) = \sum_n \nu_n(z) \qquad (2)$$

where:

$\nu_n(z)$ = the annual mean number (or rate) of events on source n for which *Z* exceeds *z* at the site.

The parameter $\nu_n(z)$ is given by the expression:

$$v_n(z) = \sum_i \sum_j \beta_n(m_i) \cdot p\left(R = r_j \middle| m_i\right) \cdot p\left(Z > z \middle| m_i, r_j\right) \quad (3)$$

where:

$ß_n(m_i)$ = annual mean rate of recurrence of earthquakes of magnitude increment m_i on source n;

$p(R=r_j|m_i)$ = probability that given the occurrence of an earthquake of magnitude m_i on source n, r_j is the closest distance increment from the rupture surface to the site;

$p(Z > z|m_i,r_j)$ = probability that given an earthquake of magnitude m_i at a distance of r_j, the ground motion exceeds the specified level *z*.

For all sources a minimum magnitude of **M** 5.0 was used for the hazard calculations.

The PSHA calculations were made using the computer program HAZ45. The basis for HAZ45 was developed by Norm Abrahamson and has been validated using test cases of the Pacific Earthquake Engineering Research (PEER) Center-sponsored “Probabilistic Seismic Hazard Analysis Code Verification” Project (Hale et al., 2018).

2.3 Seismic Source Characterization

Two types of earthquake sources are characterized in this seismic hazard analysis: (1) fault sources (Section 4.1.1); and (2) areal source zones (Section 4.1.2). Fault sources are modeled as three-dimensional fault surfaces and details of their behavior are incorporated into the source characterization. Areal source zones are regions where earthquakes are assumed to occur randomly. Seismic sources are modeled in the hazard analysis in terms of geometry and earthquake recurrence.

The geometric source parameters for faults include fault location, segmentation model, dip, and thickness of the seismogenic zone. The recurrence parameters include recurrence model, recurrence rate (slip rate or average recurrence interval for the maximum event), slope of the recurrence curve (*b*-value), and maximum characteristic magnitude. For areal source zones, only the areas, maximum characteristic magnitude, and recurrence parameters (based on the historical earthquake record) are defined.

Uncertainties in the seismic source parameters, which were sometimes large, were incorporated into the PSHA using a logic tree approach. In this procedure, values of the source parameters are represented by the branches of logic trees with weights that define the distribution of values. A sample logic tree is shown in Figure 2-1. In general, three values for each parameter were weighted and used in the analysis. Statistical analyses by Keefer and Bodily (1983) indicate that a three-point distribution of 5th, 50th, and 95th percentiles weighted 0.185, 0.63, and 0.185 (rounded to 0.2, 0.6, and 0.2), respectively, is accurate in estimating means and variances of distributions typical of those elicited via judgmental assessments when using a discrete approximation of a continuous distribution. Alternatively, they found that the 10th, 50th, and 90th percentiles weighted 0.3, 0.4, and 0.3, respectively, can be used when limited available data make it difficult to determine the extreme tails (i.e., the 5th and 95th percentiles) of a distribution. These guidelines were generally applied in developing distributions for seismic source parameters with continuous distributions (e.g., M_{max}, fault dip, slip rate or recurrence) unless the available data suggested otherwise. Estimating the 5th, 95th, or even 50th percentiles is typically challenging and involves subjective judgment given limited available data. The background seismicity maximum characteristic magnitude was modeled with a five-point discrete approximation to an arbitrary continuous distribution, with weights of 0.101, 0.244, 0.310, 0.244 and 0.101.

2.3.1 Source Geometry

In a PSHA, it is assumed that earthquakes of a certain magnitude may occur randomly along the length of a given fault or segment. The distance from an earthquake to the site is dependent on the source geometry, the size and shape of the rupture on the fault plane, and the likelihood of the earthquake occurring at different points along the fault length. The distance to the fault is defined to be consistent with the specific ground motion model used to calculate the ground motions. The distance, therefore, is dependent on both the dip and depth of the fault plane, and a separate distance function is calculated for each geometry and each ground motion model. The size and shape of the rupture on the fault plane are dependent on the magnitude of the earthquake; larger events rupture longer and wider portions of the fault plane. The rupture dimensions were modeled following the magnitude-rupture area and rupture width relationships of Wells and Coppersmith (1994).

2.3.2 Fault recurrence

The recurrence relationships for the faults are modeled using the exponentially truncated Gutenberg-Richter, characteristic earthquake, or the maximum magnitude recurrence models. These models are weighted (see example in Figure 2-1) to represent our judgment on their applicability to the sources. For the areal source zones, only an exponential recurrence relationship is assumed to be appropriate.

The general approach of Molnar (1979) and Anderson (1979) was used to arrive at the recurrence for the exponentially truncated model. The number of events exceeding a given magnitude, *N(m)*, for the truncated exponential relationship is:

$$N(m) = \alpha(m^o)\frac{10^{-b(m-m^o)} - 10^{-b(m^u-m^o)}}{1 - 10^{-b(m^u-m^o)}} \quad (4)$$

where $\alpha(m^o)$ is the annual frequency of occurrence of earthquakes greater than the minimum magnitude, m^o; *b* is the Gutenberg-Richter parameter defining the slope of the recurrence curve; and m^u is the upper-bound magnitude event that can occur on the source. A m^o of moment magnitude (**M**) 5.0 was used for the hazard calculations because smaller events are not considered likely to produce ground motions with sufficient energy to damage well-designed structures.

The characteristic recurrence model is described by Aki (1983) and Schwartz and Coppersmith (1984) in which the faults rupture with a “characteristic” magnitude on specific segments. The numerical model of Youngs and Coppersmith (1985) was used for the characteristic model, in which the number of events exceeding a given magnitude is the sum of the characteristic events and the non-characteristic events.

The maximum magnitude model can be regarded as an extreme version of the characteristic model. The model proposed by Wesnousky (1986) was adopted. In the maximum magnitude model, there is no exponential portion of the recurrence curve, i.e., events are modeled with a normal distribution about the characteristic magnitude.

The recurrence rates for the fault sources are defined by either the slip rate or the average return time for the maximum or characteristic event and the recurrence *b*-value. The slip rate is used to calculate the moment rate on the fault using the following equation defining the seismic moment:

$$M_o = \mu A D \quad (5)$$

where M_o is the seismic moment (in dyne-cm), μ is the shear modulus (dyne/cm^2), A is the area of the rupture plane (cm^2), and D is the slip on the plane (cm). Dividing both sides of the equation by time results in the moment rate as a function of slip rate:

$$\dot{M}_o = \mu A S \quad (6)$$

where $\dot{M}_o$ is the moment rate and S is the slip rate. M_o has been related to moment magnitude, **M**, by Hanks and Kanamori (1979):

$$\mathbf{M} = 2/3 \log M_o - 10.7 \quad (7)$$

Using this relationship and the relative frequency of different magnitude events from the recurrence model, the slip rate can be used to estimate the absolute frequency of different magnitude events.

The average return time for the characteristic or maximum magnitude event defines the high magnitude (low likelihood) end of the recurrence curve. When combined with the relative frequency of different magnitude events from the recurrence model, the recurrence curve is established.

2.4 Ground Motion Characterization

Empirical ground motion models for response spectral acceleration are used to characterize the ground motions in the seismic hazard analysis. The models used in this study are selected on the basis of the appropriateness of the site conditions and tectonic environment for which they were developed.

The variability in ground motion prediction is included in the PSHA by using the log-normal distribution about the median values as defined by the standard deviation associated with each model. Five standard deviations about the median value are included in the analysis.

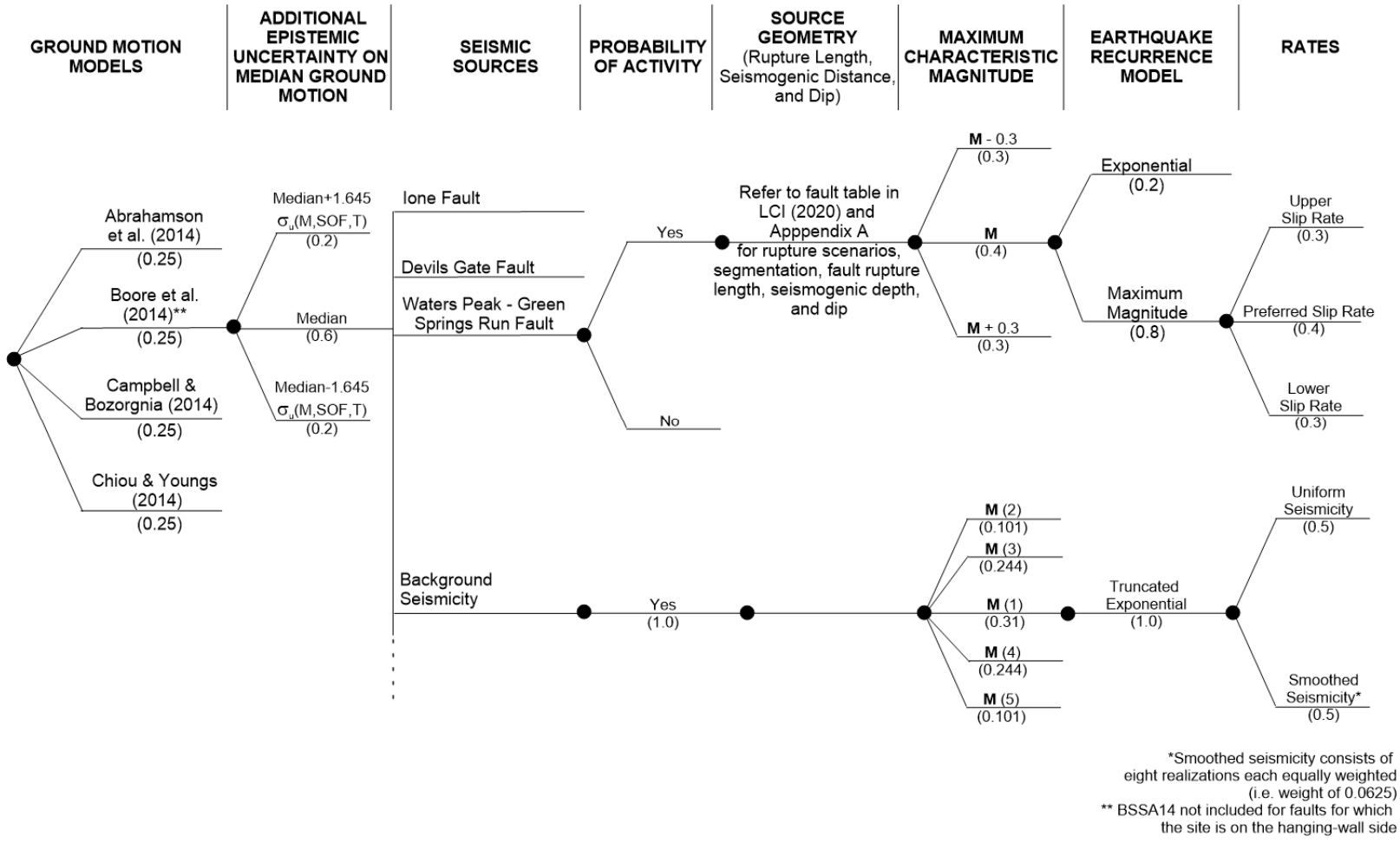

Figure 2-1. Example Logic Tree

3. Seismotectonic Setting and Historical Seismicity

3.1 Seismotectonic Setting

Pardee and Camanche Dams are located in the Sierra Foothills of central California east of the Sacramento Valley (Figure 1-1). The modern tectonic setting of central California is dominated largely by the transform plate boundary contact between the Pacific and North American plates south of the Mendocino triple junction. The Pacific plate is sliding in a north-northwest direction (N35°W to N38°W) at a rate of about 50 mm/yr with respect to the North American plate (Dixon et al., 2000). Right-lateral strike-slip displacement along the major branches of the San Andreas fault system accommodates most of this plate motion, with the remainder generating Holocene tectonism and seismicity at the western continental margin and to the east in the Sierra Nevada and Basin and Range Provinces (Minster and Jordan, 1987; Atwater, 1970). East of the Coast Ranges, the Great (Central) Valley and the adjacent Sierra Nevada form a relatively stable crustal block composed of Mesozoic crystalline basement that dips gently to the west (Hill et al., 1991). The western edge of the Sierra Nevada block, beneath the sediments of the Great Valley, is generally thought to be coincident with the western margin of the Great Valley. This region is referred to as the Coast Ranges-Sierran Block (CRSB) boundary zone (Wong and Ely, 1983; Wong et al., 1988), where compressional deformation occurs on reactivated east-verging, low-angle structures (Unruh and Moores, 1992; Unruh and Lettis, 1998). High slip-rate faults associated with the San Andreas fault system lie to the west of this boundary zone.

The Sierra Nevada is a 600-km-long by 150-km-wide composite batholith that was emplaced over a period of nearly 100 million years, from approximately 180 to 80 Ma (Bateman and Eaton, 1967). Uplift of the range to its present elevation occurred in late Cenozoic time around 10 to 3.5 Ma. In the vicinity of the central Sierra Nevada, the fault activity map of California compiled by Jennings (1994) and the USGS Quaternary fault and fold database (USGS, 2019) shows few Quaternary faults that fall within a 60-km-long zone that extends northwest from the Great Valley to Lake Tahoe in the east. However, more recent research suggests that “internal” faults may be distributed relatively evenly across the Sierra Nevada, and that cumulative late Cenozoic vertical separations and slip rates on these faults systematically increase eastward towards the Tahoe-Sierra Frontal fault system along the eastern escarpment of the Sierra (from thousandths of a mm/yr to hundredths of a mm/yr). Only a few of these faults show latest Pleistocene or younger movement. The late Cenozoic faults of the western Sierra Nevada are the closest to the dam sites and typically exhibit normal dip-slip and normal right-lateral-oblique motion. Many of these faults are reactivated portions of the Mesozoic Foothills fault system (PG&E, 1994), and have been interpreted to have low long-term slip rates (Schwartz et al., 1977; Woodward-Clyde Consultants, 1978; PG&E, 1994; Page and Sawyer, 2007; LCI, 2020).

The Walker Lane belt is a structural transition zone between the relatively stable Sierra Nevada microplate to the west and the extensional Basin and Range Province to the east. The northwest-trending, greater than 100-km-wide Walker Lane Belt is characterized by Quaternary, distributed, dextral-shear accommodated on northwest-striking dextral faults and north-striking normal faults, with possibly lower activity on northeast-striking sinistral faults. Geodetic studies indicate that the Sierra Nevada microplate is moving northwestward at a rate of about 11 mm/yr and rotating counter-clockwise relative to the stable North American plate (Hammond and Thatcher, 2007; Unruh and Humphrey, 2017), and possibly that 6-8 mm/yr of northwest-directed dextral shear is occurring across the northern Walker Lane Belt at 39.5º to 40º latitude, resulting in dextral transtensional deformation within the belt (Thatcher et al., 1999; Dixon et al. 2000; Svarc et al., 2002; Bormann et al., 2012). The northwest-directed shear and trans-extensional deformation of the Walker Lane Belt are in contrast to the more purely extensional deformation occurring in the Basin and Range Province to the east. Overall, the Quaternary fault patterns in the Walker Lane Belt and western Basin and Range Province reflect this gradual transition from northwest dextral shear to the west to east-west extension to the east and are consistent with geodetic surveys in the region.

3.2 Historical Seismicity

The Pardee and Camanche Dams are located in a region characterized by a relatively low-level of historical seismicity, though seismographic coverage of the region is far less than in Coastal California.

For Pardee Dam only 9 events have been recorded within 50 km of the dam. The largest of these is the 1986 duration magnitude (M_D) 3.2 event, which occurred 49 km west of the dam. The closest recorded event is the 1986 M_D 2.5 event, 9 km east of the dam. Within 100 km of the dam, 8 events M ≥ 5.0, and 3 events M ≥ 6.0 have been recorded, all of which have occurred to the west of the dam in the San Francisco Bay Region. The largest of these is the 1892 **M** 6.5 event, 96 km west-northwest of the dam (Figure 3-1).

For Camanche Dam only 14 events have been recorded within 50 km of the dam. The largest of these is the 2003 M_D 3.5 event, 47 km northwest of the dam. The closest recorded event is the 1989 M_D 2.7 event, 25 km southeast of the dam. Within 100 km of the dam, 11 events M ≥ 5.0, and 4 events M ≥ 6.0 have been recorded, all of which have occurred to the west of the dam in the San Francisco Bay Region. The largest of these is the 1892 **M** 6.5 event, 88 km west-northwest of the dam (Figure 3-1).

The 1892 **M** 6.5 event occurred on April 19 near Vacaville in Solano County. Ground fissures formed near Allendale, between Vacaville and Winters, and several buildings in the area collapsed or shifted off their foundation. At Vacaville, almost all brick structures were destroyed, many frame buildings were impaired, and chimneys were twisted or knocked to the ground. Similar damage was reported from Winters. Although damage in general was less serious in Dixon, many school buildings were almost ruined. Modified Mercalli intensity VIII or higher was observed over an area of 1,100 km^2. The earthquake was felt north to Redding, east to Virginia City, Nevada, and south to Salinas and Fresno (Stover and Coffman, 1993).

Just two days later a **M** 6.2 event occurred near Winters. This further damaged the structures weakened by the April 19 event. The damage was most severe in Winters with many buildings leveled. At Esparto, every brick chimney fell and wood-frame buildings were wrenched out of shape. Many chimneys were wrecked in Sacramento and Woodland. The area shaken at Modified Mercalli intensity VIII or larger was about 890 km^2, but the general felt area was about the same as that of the April 19 event (Stover and Coffman, 1993).

These two earthquakes occurred at the western margin of the Great Valley and the eastern margin of the Diablo Range (Figure 3-1) and are interpreted to have occurred on structures that formed in response to northeast-southwest compression resulting from divergence between the San Andreas fault and the orientation of the Pacific-North American plate motion (Wentworth and Zoback, 1990). In 1984, Wakabayashi and Smith (1984) described a series of west-dipping faults that separate the Coast Ranges from the Central Valley, the CRSB boundary zone. The CRSB faults are associated with a buried fold and thrust belt and, in most cases, do not rupture the surface. O'Connell et al. (2001) utilized 3D *P*-wave velocity structure, 2D seismic reflection data, elastic deformation modeling, and synthetic ground-motion modeling of the April 1892 Vacaville–Winters earthquake sequence to provide strong constraints on the locations and downdip geometries of the Gordon Valley and Trout Creek blind thrust fault segment. The 19 April 1892 earthquake probably occurred on the Gordon Valley blind thrust fault, while the 21 April 1892 earthquake probably occurred along the northern 10 km of the Gordon Valley blind thrust fault in the Gordon Valley–Trout Creek fault segmentation region near Winters (O'Connell et al., 2001).

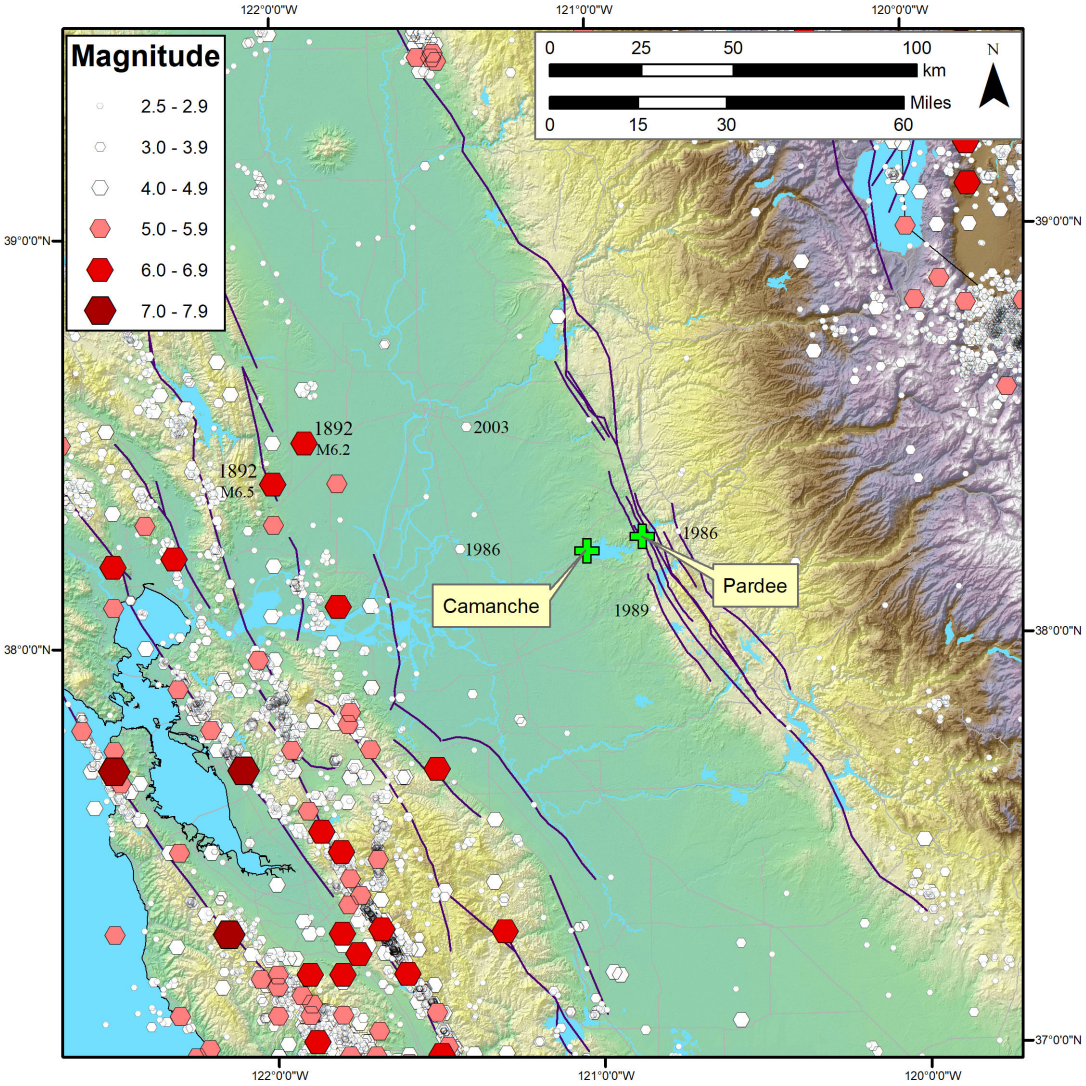

Source: Seismicity from Field et al. (2013) updated ComCat. Faults from AECOM seismic source model and LCI (2020)

Figure 3-1. Historical Seismicity, 1869 to 2023, in the Site Region

4. Inputs to Analysis

4.1 Seismic Sources

Seismic source characterization is concerned with three fundamental elements: (1) the identification, location, and geometry of significant sources of earthquakes; (2) the maximum characteristic size and distribution of the earthquakes associated with these sources; and (3) in the PSHA, the rate at which they occur. The source parameters for the significant faults in the site region (generally within about 150 km) are characterized for input into the hazard analyses (Figure 4-1). Areal source zones, used to represent background earthquakes, are also characterized and used in the PSHA.

4.1.1 Faults

The fault model used in this study is adopted from HID for Pardee Dam (LCI, 2020) for the nearby Foothills fault system, and the AECOM seismic source model for the more distant faults in the San Francisco Bay Area. The AECOM seismic source model was developed from two main sources: (1) a model developed as part of the California Department of Water Resources' Delta Risk Management Strategy Project (URS Corporation/Jack Benjamin & Associates, 2007) and (2) the Unified California Earthquake Rupture Forecast (UCERF3) source model (Field et al., 2013). Each seismic source is characterized using the latest available geologic, seismologic, and paleoseismic data.

Figure 4-1 shows the locations of the faults relative to the project site, with Figure 4-2 showing the local faults of the Foothills fault system. Appendix A summarizes the fault source parameters used in this analysis. Faults are included that are judged to be at least potentially active and that may contribute to the probabilistic hazard because of their maximum characteristic earthquakes and/or proximity to the project site (Appendix A). In this analysis, most faults are modeled as single, independent, planar sources extending the full extent of the seismogenic crust. Thus, fault dips are averages estimated through the seismogenic crust. Generally, in western California, the seismogenic crust ranges from 11 to 15 km thick based on well-located contemporary seismicity (e.g., Oppenheimer and MacGregor-Scott, 1992).

Recurrence rates for many of the faults within the region are either poorly understood or unknown due to a lack of reliable paleoseismic data. Thus, fault activity is expressed as an average annual slip rate (in mm/yr) for those faults where recurrence interval (years between events) data are not available. The uncertainty in slip rates and other input parameters are accommodated in the PSHA through the use of logic trees (Figure 2-1).

Uncertainties in determining recurrence models can significantly impact the hazard analysis. Truncated exponential, maximum-magnitude, and characteristic recurrence models were considered, with various weights depending on source geometry and type of rupture model. Historical seismicity and paleoseismic investigations along faults in the western U.S. (e.g., San Andreas fault) suggest that characteristic behavior is more likely for individual faults (Schwartz and Coppersmith, 1984). Therefore, except for faults associated with the Foothills fault system, the characteristic model is favored (weight of 0.70) while the maximum magnitude model is weighted 0.30 (Figure 2-1). For the characteristic model, the characteristic events are distributed uniformly over a $\pm$ 0.25 magnitude unit around the characteristic magnitude, and the remainder of the moment rate is distributed exponentially using equation (4) with a maximum magnitude 0.25 units lower than the characteristic magnitude (Youngs and Coppersmith, 1985). For the maximum magnitude model, events are modeled with a normal distribution about the characteristic magnitude, with a sigma of 0.25. The distribution is truncated at 0.5 units above the characteristic magnitude. For the Foothills fault system the maximum magnitude (weighted 0.8) and truncated exponential (weighted 0.2) recurrence models were used as described in the HID.

Tables A1 and A2 in Appendix A contain a full list of the rupture scenarios, characteristic magnitudes, slip rates and other important fault characteristics for all faults used in the PSHA model. A brief description of the more significant faults is provided below.

4.1.1.1 Foothills Fault System

The Foothills fault system (Figures 4-1 and 4-2) formed in response to eastward convergence and subduction during Mesozoic time (Clark, 1960). The fault zone is largely composed of Mesozoic structures that have not been active in Cenozoic time. However, some preferentially oriented structures

within this older framework have been reactivated in the late Cenozoic and some even in the Quaternary. Although originally developed as reverse faults associated with convergence, the late Cenozoic faults exhibit primarily normal dip-slip motion in response to tectonic extension (LaForge and Ake, 1999). Earthquake focal mechanisms also indicate extensional stresses along the Sierran Foothills (Lahr et al., 1976). Page and Sawyer (2001) estimate that about 1 to 2 mm/yr of dextral shear are also accommodated by faulting within the central Sierra Nevada and some of the more westerly-striking faults within the Foothills fault system are dextral-oblique.

The Foothills fault system is complex and its paleoseismic history is still not well known. This is due to a lack of late Cenozoic deposits over much of the southern part of the zone that prevents evaluation of fault continuity (Schwartz et al., 1996) and erosion rates that exceed fault-slip rates. It appears that only faults with multiple late Cenozoic surface-rupturing events are conspicuous, given the geologic conditions that exist in the central Sierra Nevada (Schwartz et al., 1996).

Page and Sawyer (2001; 2007) characterize late Cenozoic faults within the Sierra Nevada as being generally less than 20 km long with predominantly vertical slip and minor lateral slip. They characterize the faults as having very low slip rates that range from 0.001 to 0.01 mm/yr with repeated displacement events in the past 4 to 5 million years. They estimate recurrence intervals for repeated fault ruptures on the order of tens of thousands of years. They conclude that many of the late Cenozoic faults, but not all, are reactivated parts of the Mesozoic Foothills fault system. They emphasize, however, that most of the Mesozoic faults are not late Quaternary faults.

Recently, LCI (2020) performed a Foothills fault system study for Pardee Dam. This included three paleoseismic trenches of the Waters Peak fault near Pardee Dam.

Based on this study and field investigations of other nearby faults, LCI (2020) developed a HID for seven segments of the Foothills fault system (Table A1). This study has adopted the LCI (2020) characterization with three additional segments within 50 km of Pardee Dam (Figure 4-2; Table A1). The characterization of these additional segments is adopted from Anderson and Ake (2008).

Recognizing that existing mapping of potentially active faults is incomplete and the uncertainty of active and non-active individual faults within these sections, a "floating earthquake" model has been included in the source model, that allows an earthquake to occur along any portion of the Foothills fault system (Figure 4-1). The maximum earthquake for the floating earthquake within the Foothills fault system is modeled as a **M** 6.5 (Table A1), based on a surface rupture length of 20 km. Slip rate information is adopted from the Anderson and Ake (2008) study based on their “simplified” fault. The floating earthquake was weighted 0.2, with the segmented model weighted 0.8 (Table A1).

The segments most important to the seismic hazard at Pardee and Camanche Dams are summarized below from LCI (2020):

Waters Peak – Green Springs Run Fault

The Waters Peak fault represents one of the western-most faults comprising the Bear Mountain fault zone and is defined by a prominent northwest-trending lineament. The fault trace is located 0.2 km west of Pardee Dam and 14.5 km east of Camanche Dam. The Waters Peak fault is modeled as a 62 km fault from north of Pardee Reservoir to approximately 5 km south of Table Mountain, based on a connection with the Green Springs Run fault, a similarly active late Cenozoic structure along strike to the southeast without significant steps, bends, or structural complexities. The Waters Peak fault is well expressed in the Mokelumne River gorge and Pardee Dam spillway where it dips steeply to the east at 64° to 70°. This places Pardee Dam in the hanging wall, while Camanche Dam is in the footwall. The style of faulting across the Waters Peak fault in the current tectonic regime is east-down, strike-slip-normal oblique based on structural and stratigraphic evidence in trenches (LCI, 2020).

Trenches across the Waters Peak fault at multiple locations between Pardee Dam and New Hogan Reservoir document offset of Miocene Mehrten Formation and offset of younger alluvium/colluvium interpreted to be middle to late Quaternary age (LCI, 2020). However, it should be noted LCI’s analysis of the trench exposures, together with a detailed review of earlier United States Army Corp of Engineers results, indicate the Waters Peak fault is *likely* inactive per DSOD criteria for active faults in California (LCI, 2020), that is no evidence of rupture in the lasts 35,000 years. However, there is clear evidence of

activity in the Quaternary, so that the fault could be labeled as conditionally active (DSOD, 2018) and therefore the fault was included in the seismic hazard analysis with a probability of activity of 1.0.

The characteristic magnitudes for the Waters Peak – Green Springs Run fault source are **M** 7.0, **M** 6.4, and **M** 6.0, based on characteristic rupture lengths of about 40 km, 20 km, and 12 km, respectively, the estimated rupture areas, and the empirical magnitude-area relation of Hanks and Bakun (2014).

The trench data collected by LCI (2020) suggest a record of zero earthquakes in the past approximately 60,000 years and likely one (possibly two) event in the past approximately 130,000 years (resulting in about 0.5 m vertical displacement). In order to explore what constraint these data may have on fault slip rate, LCI considered a range of *vertical* fault slip rates, implied accumulated fault slip over the 130,000 year observational period from the trenches, and a broad range of estimated single-event earthquake slips to see what combinations of slip rate and per-event slip were inconsistent with the trench data. This approach suggests that vertical slip rates less than 0.02 mm/yr are consistent with the trench data, and vertical rates 0.03 or higher are highly inconsistent with the trench data. Using the paleoseismic constraints but also considering the long-term slip rate data, LCI derive a preferred net slip rate of 0.01 mm/yr with an uncertainty range of 0.004 to 0.045 mm/yr. These slip rates are consistent with vertical displacements of 0.5 to 2 m in 130,000 years.

Ione Fault

The Ione fault is located approximately 1 km west of Pardee Dam and 13.9 km east of Camanche Dam. it is recognized by its strong geomorphic expression as a southwest-facing scarp mainly north of the Mokelumne River. The 17-km-long fault source extends from north of Dry Creek near Ione to a point directly north of the Mokelumne River. The southwest-side down fault places Pardee Dam in the footwall, while Camanche Dam is in the hanging wall.

Estimates of vertical separation of the Ione Formation across the fault vary from about 150 to 250 m, to 40 to 120 m (LCI, 2020). USACE (1995) trenched the Ione fault northwest of the Lake Amador spillway channel and evidence of late Quaternary (Holocene) activity of the Ione fault could not be confirmed. Alternative interpretation of the trench suggests faulting post-dated Holocene debris flow deposits and classify the Ione fault as late Quaternary active. The probability of activity of the source is 0.5 based on clear evidence for offset Cenozoic strata, and possible but unconfirmed late Quaternary activity (possibly faulted Holocene debris flow deposits).

The characteristic magnitudes are **M** 6.5, **M** 6.2, and **M** 6.0 based on characteristic rupture lengths of about 20 km, 15 km, and 12 km, respectively, the estimated rupture areas, and the empirical magnitude-area relation of Hanks and Bakun (2014).

The slip rate is estimated using 40 to 120 m (preferred value 75 m) vertical separation of the Eocene Ione Formation, with estimates of the timing of onset of deformation that represent the start of the current tectonic regime between approximately 3 and 7 Ma, with a preferred value of 5 Ma. The averaged net offsets and offset ages yield a preferred slip rate of 0.03 mm/yr, with an uncertainty range of 0.002 to 0.1 mm/yr.

4.1.1.2 Coastal California Faults

In addition to faults along the western margins of the Sierra Nevada, significant faults to the west of Pardee and Camanche Dams along the active plate boundary are incorporated into the analysis. Most of these sources are faults within the San Andreas fault system, including the San Andreas, Hayward-Rodgers Creek, Calaveras, and Green Valley-Berryessa-Hunting Creek faults (Figure 4-1, Table A2).

San Andreas Fault System

The dominant active fault in California is the San Andreas fault, which lies west of the sites (Figure 4-1). The San Andreas fault extends from the Gulf of California, Mexico, to Point Delgada on the Mendocino Coast in northern California, a total distance of 1,200 km. The San Andreas fault system accommodates the majority of the motion between the Pacific and North American plates (Wallace, 1990). This fault is the largest active fault in California. Movement on the San Andreas fault is right-lateral strike-slip, with a total offset of some 560 km (Irwin, 1990). Over most of its southern extent, the San Andreas fault is a relatively simple, linear fault trace. In central California, the San Andreas fault is clearly delineated, striking northwest, parallel to the vector of plate motion between the Pacific and North American plates. South of

the San Francisco Bay area, however, the fault splits into a number of branch faults or splays, including the Calaveras and Hayward faults.

The San Andreas is responsible for two of the largest known earthquakes in California. The 1857 **M** 7.9 Fort Tejon and 1906 **M** 7.9 San Francisco earthquakes. The 1857 Fort Tejon earthquake resulted from rupture of the southern part of the fault from Parkfield south to near Wrightwood, a distance of approximately 360 km. Displacement averaged 4.5 m with as much as 9 m reported on the Carrizo Plain. The 1906 San Francisco earthquake resulted from rupture of the northern part of the fault from San Juan Bautista north to Point Delgada, a distance of approximately 475 km. The average displacement on the fault was 5.1 m in the area north of the Golden Gate and 2.5 m in the Santa Cruz Mountains (WGCEP, 2008).

Based on differences in geomorphic expression, fault geometry, paleoseismic chronology, slip rate, seismicity, aseismic creep, and historical fault ruptures, the San Andreas fault is divided into a number of fault segments. Each of these segments may be capable of rupturing independently or in conjunction with adjacent segments. The northern San Andreas includes the Santa Cruz Mountains, Peninsula, North Coast and Offshore segments. Based on the lengths of the fault segments, they are capable of producing estimated maximum characteristic earthquakes of **M** 7.1, 7.3, 7.5 and 7.4, respectively. The 1906 earthquake was the result of rupture of the Offshore (northernmost segment north of Point Arena), North Coast, Peninsula, and Santa Cruz Mountains segments. Two- or three-segment ruptures also may be possible (WGCEP, 2008). The maximum earthquakes associated with these potential multi-segment ruptures are estimated to range from **M** 7.1 to 8.0 (Table A1).

For the hazard analysis the rupture segmentation of WGCEP (2008) was utilized (Table A1), however the segment geometry, slip rates, and maximum characteristic magnitudes were updated from Field et al. (2013).

Calaveras Fault

This fault is a main component of the San Andreas system, branching off the main San Andreas fault south of Hollister, and extending northwards for approximately 130 km (Figure 4-1). The predominant sense of motion on the Calaveras fault is right-lateral strike-slip. In the southern San Francisco Bay region, the Calaveras fault traverses the Hollister Plain and the Diablo Range east of the Santa Clara Valley and is a major structural boundary between the Diablo Range and the San Francisco Bay structural depression (Page, 1982). The Calaveras fault exhibits prominent geomorphic expression along its entire active length and has generated small and moderate earthquakes during historical time. Abundant microseismicity and several historical moderate-magnitude earthquakes characterize the central Calaveras fault (Bakun, 1980; Bakun et al., 1984; Bakun and Lindh, 1985; Cockerham and Eaton, 1987; Oppenheimer et al., 1990; Schaff et al., 2002) (Figure 3-1).

Between 1949 and 2007, **M** > 5 earthquakes ruptured the central Calaveras fault in a northward progression as post-seismic relaxation following one event triggered the next event (Du and Aydin, 1992). The earthquake cycle proceeded as follows: 1949 Gilroy earthquake (**M** 5.2), 1979 Coyote Lake earthquake (**M** 5.7), 1984 Morgan Hill earthquake (**M** 6.2), 1988 Alum Rock earthquake (**M** 5.1) (Oppenheimer et al., 1990), and the 2007 Alum Rock **M** 5.6 earthquake. The Coyote Lake and Morgan Hill rupture areas appear to be a repeat of previous events in 1897 and 1911, respectively (Oppenheimer et al., 1990). Oppenheimer et al. (1990) analyzed spatial patterns of microseismicity along the central Calaveras fault and inferred that the central Calaveras fault releases strain predominantly through aseismic creep and small to moderate (≤ **M** 6.2) magnitude earthquakes.

The northern Calaveras fault exhibits far less historical seismicity, with only one moderate magnitude event along the fault north of Calaveras Reservoir, the 1861 **M** 5.8 San Ramon Valley earthquake (Oppenheimer and Lindh, 1992). This earthquake produced surface cracking in San Ramon for a length of either 4 km (Jennings, 1994) or 10 to 13 km (Rogers and Halliday, 1992), although this cracking has been attributed to landsliding (Hart, 1981) and possibly strong ground shaking (WGCEP, 2008). During the past 35 years, there have been five swarms of earthquakes at or near the northern part of the northern Calaveras fault (1970 Danville, 1976 Danville, 1990 Alamo, 2002 San Ramon and 2003 Las Trampas swarms), although all of these appear to be on previously unrecognized faults that intersect and strike nearly orthogonal to the northern Calaveras fault.

Based on structural relations with other major faults, contemporary seismicity, rate of present-day creep and geodetic deformation, and geomorphic expression, the Calaveras fault is interpreted to consist of four segments (Kelson 2001; WGCEP, 2008):

- Northern Calaveras (NCF), mapped from Alamo southwards to the Calaveras Reservoir;
- Central Calaveras (CCF), mapped from the Calaveras Reservoir southwards to San Felipe Lake;
- Southern Calaveras (SCF), mapped from San Felipe Lake to south of Hollister near the junction of the San Benito River and Tres Pinos Creek; and
- Paicines Section mapped from near the junction of the San Benito River and Tres Pinos Creek south to near Stone Canyon.

WGCEP (2008) analyzed all available local and regional information on the Calaveras fault and considered multiple fault-rupture models and rupture. For the hazard analysis the rupture segmentation of WGCEP (2008) was utilized (Table A1), however the segment geometry, slip rates, and maximum characteristic magnitudes were updated from Field et al. (2013).

Hayward-Rodgers Creek Fault System

The Hayward fault extends for 100 km from the area of Mount Misery, east of San Jose, to Point Pinole on San Pablo Bay. The northern continuation of this fault system is the Rodgers Creek fault (Figure 4-1). The two faults are separated by a 5-km-wide right step beneath San Pablo Bay. Systematic right-lateral geomorphic offsets and creep offset of cultural features have been well documented along the entire length of the fault (Lienkaemper, 1992). The last major earthquake on the Hayward fault, in October 1868, occurred along the southern segment of the fault. This **M** 6.8 event caused toppling of buildings in Hayward and other localities within about 5 km of the fault. The surface rupture associated with this earthquake is thought to have extended for approximately 30 km, from Warm Springs to San Leandro, with a maximum reported displacement of 1 m. The Hayward fault is considered the most likely source of the next major earthquake in the San Francisco Bay area (WGCEP, 2008). As well as undergoing displacement during earthquake ruptures, the Hayward fault also moves by aseismic creep. Measurements along the fault over the last two decades show that the creep rate is 5 to 9 mm/yr (Lienkaemper and Galehouse, 1997).

Recent research of historical documents has led to the conclusion that an earthquake in 1836, previously thought to have occurred on the northern Hayward fault, occurred elsewhere (Toppozada and Borchardt, 1998), thereby increasing the time since the last earthquake on this segment of the fault. Recent paleoseismic trenching along the northern Hayward fault indicates that the last surface rupturing earthquake along this part of the fault was sometime between 1626 and 1724 (Lienkaemper et al., 1999). This study also indicated at least four surface-rupturing earthquakes in the last 2,250 years. The WGCEP (2008) assigns maximum earthquakes of **M** 6.9, and recurrence intervals of 318 and 211 years, for the northern and southern segments of the Hayward fault, respectively. Rupture of the combined northern and southern segements would generate an earthquake of **M** 7.2. Our model also incorporates a scenario where the Hayward fault ruptures along with the Rodgers Creek and Healdsburg fault. Rupture of the entire length of all three faults would generate a maximum earthquake of **M** 7.5. Rupture of the Rodgers Creek fault, Healdsburg and northern segment of the Hayward fault would generate a maximum event of **M** 7.4.

Green Valley-Berryessa-Hunting Creek Fault System

The Green Valley-Berryessa-Hunting Creek fault system, a northwest-striking, right-lateral, strike-slip fault, includes multiple faults, which previous hazard models (e.g. 2008) treated as independent sources, but which new mapping and analysis by Lienkaemper (2010) suggests can rupture in combination (Figure 4-1; Table A2). The earlier models included: the Hunting Creek-Berryessa fault; and the Concord-Green Valley fault.

The source characterization of these faults for this study is based on the Lienkaemper mapping and the characterization in the UCERF 3 statewide hazard model, along with earlier data and interpretations. In this model, the Concord-Green Valley fault is no longer treated as segmented into the Concord, southern Green Valley, and northern Green Valley segments of the WGCEP (2008), but is considered a single

unsegmented fault, the Green Valley fault as there is no evidence of segmentation at the boundaries. The Berryessa fault is part of the Green Valley fault system. The Hunting Creek fault serves as a "fuse" between the Bartlett Springs fault to the north and Green Valley fault. Rupture lengths are obtained from Lienkaemper mapping (Lienkaemper, 2010).

4.1.2 Background Seismicity

To account for the hazard from background (floating or random) earthquakes that are not associated with known or mapped faults, regional seismic source zones are used in the PSHA. An example background earthquake is the 1986 **M** 5.7 Mt. Lewis earthquake, which occurred east of San Jose and resulted in no discernable surface rupture. In this analysis, the hazard from background earthquakes is addressed through the use of regional source zones (Figure 4-3). The regional source zones are defined based on similar seismotectonic characteristics such as maximum magnitude, style of faulting, seismogenic thickness and historic and instrumental seismicity rate.

The seismic source zones and rates were adopted from the HID (LCI, 2020). The zones included are the Walker Lane (WL), Sierra Nevada-Great Valley (SNGV), Coast Ranges-Great Valley Boundary (CRGVB), and the Coast Ranges (CR). The use of seismic source zones assumes that background earthquakes are uniformly (randomly) distributed throughout the seismogenic crust. However, some seismicity may be stationary through time (at least over the next few decades of interest) and can be smoothed, thus the hazard from seismicity that clusters in a specific seismic zone is retained spatially. This scheme addresses both the spatial stationarity of seismicity and its randomness. Recurrence parameters (*b*-values and rates) for both the uniform and gridded seismicity were calculated using the historical seismicity record and the program ABSMOOTH (EPRI/DOE/NRC, 2012). The gridded seismicity (0.2-degree cells) includes eight realizations to provide a good representation of the underlying distributions. The uniform model is assigned a weight of 0.5 and the eight gridded seismicity models are assigned a total weight of 0.5, or 0.0625 for each of the eight models individually (LCI, 2020).

The recurrence curves for the SNGV as calculated in the hazard code are shown on Figure 4-4. The dam sites lie within the SNGV (Figure 4-3).

The HID states that fault related seismicity was not removed from the catalog when developing the recurrence calculations. For most of the zones, there are few earthquakes associated with faults included in the seismic source model, with the exception of the CR. As such there may be double counting of the ground motions from the CR sources, so the recurrence for the CR was recalculated in this study.

To calculate the recurrence for the CR, an earthquake catalog was compiled from Field et al. (2013) updated from the Advanced National Seismic System comprehensive catalog (ComCat). Events within 10-km-wide corridors of active faults, such as the San Andreas fault, were removed from the catalog, following the process in Youngs et al. (1992). Dependent events, such as aftershocks, foreshocks, and smaller events within an earthquake swarm, were identified and removed from the catalogs using the technique developed by Youngs et al. (2000). Completeness intervals were adopted from the HID (LCI, 2020). The recurrence relationships for the CR were estimated using the maximum likelihood procedure developed by Weichert (1980). The earthquake recurrence of the background seismic zones is described by the truncated exponential form of the Gutenberg-Richter relationship.

Corrections for magnitude error and magnitude rounding are incorporated into the recurrence estimates for the regional catalog following the methodology of Felzer (2008). Rounding errors were determined by observing the magnitudes reported in the catalogs over time and estimated magnitude errors based on Felzer (2008). For those earthquakes whose errors have been reported in the literature, these errors are included. Otherwise a standard error of 0.33 was assigned to pre-1962 earthquakes, 0.22 for 1962-1982 and 0.11 for earthquakes occurring after 1982. These errors are estimated based on whether the earthquake magnitudes were based on a maximum felt MM intensity or whether they were instrumentally determined. First the recurrence was calculated for the catalog. Then the recurrence was re-calculated 500 times, first fixing the *b*-value obtained initially, and applying the two magnitude corrections discussed above each time (first the rounding error, then the magnitude error for each magnitude in the catalog) to obtain an average corrected *a*-value. The resulting earthquake recurrence curve is shown on Figure 4-5 for the CR. The recurrence parameters and return intervals for the CR seismic source zone are given in Tables 4-1 and 4-2.

Because of the limited duration and incompleteness of the historical catalog and the small number of events and their narrow magnitude range used in the recurrence calculations, uncertainties in the recurrence parameters for the background seismicity are large. To incorporate the uncertainties into the PSHA, three *b*-values for each regional seismic source zone were used, the best estimate, and plus and minus 0.1 values, weighted 0.6, 0.2, and 0.2, respectively. This uncertainty also accounts for the possibility that the historical record may not be a robust representation of the next 50 to 100 years. An inspection of the resulting recurrence intervals for **M** 5 and 6 events was performed to check the reasonableness of the three *b*-values. The *a*-values were held fixed because the recurrence curve is better constrained at the smaller magnitudes.

Similar to the other seismic zones the seismicity in the CR was smoothed, though with a Gaussian filter. In the Gaussian smoothing approach (Frankel, 1995), the historical seismicity is smoothed on a grid at 0.1 degree intervals using a spatial window of 15 km to incorporate a degree of stationarity. The uniform model is assigned a weight of 0.5 and the gridded seismicity model is assigned a weight of 0.5. Sensitivity studies show the mean rates when smoothing using the Gaussian filter are similar to the ABSMOOTH process.

Table 4-1. Recurrence Parameters for the Regional Seismic Source Zones

Source Zone	*b*-value	$N_{M\geq5}$	Zone Area km^2	Maximum Magnitude (M_{max})	No. of Events
Coast Ranges (CR)	0.937	0.06295	42,150	7.0	329

Table 4-2. Estimated Average Recurrence Intervals for M ≥ 5 and M ≥ 6 in the Regional Seismic Source Zones

Source Zone	Recurrence Intervals M ≥ 5 (years)	Recurrence Intervals M ≥ 6 (years)
Coast Ranges (CR)	15.9	155.4

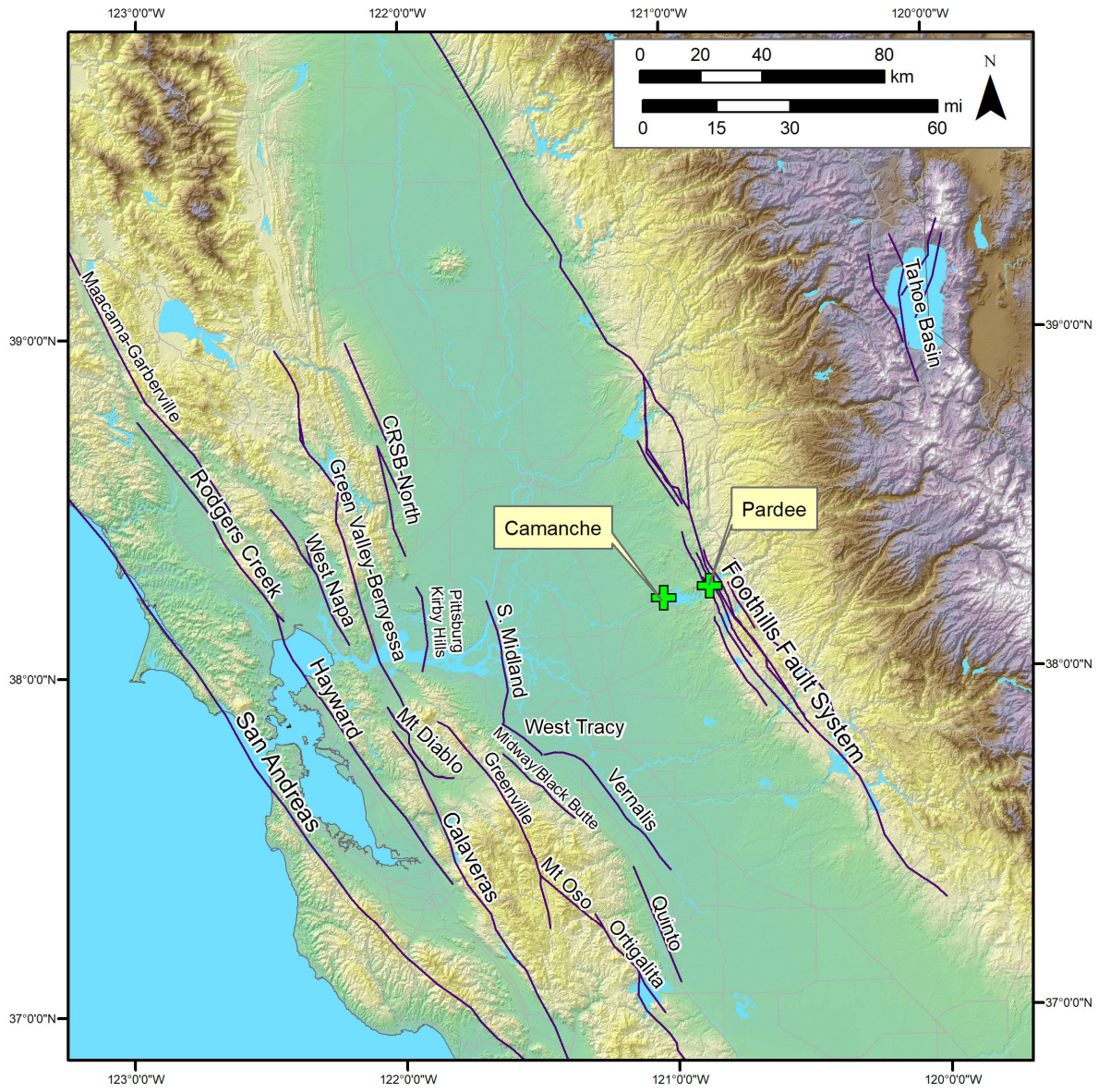

Source: Faults from AECOM seismic source model and LCI (2020)

Figure 4-1. Regional Quaternary Faults included in the Hazard Analysis

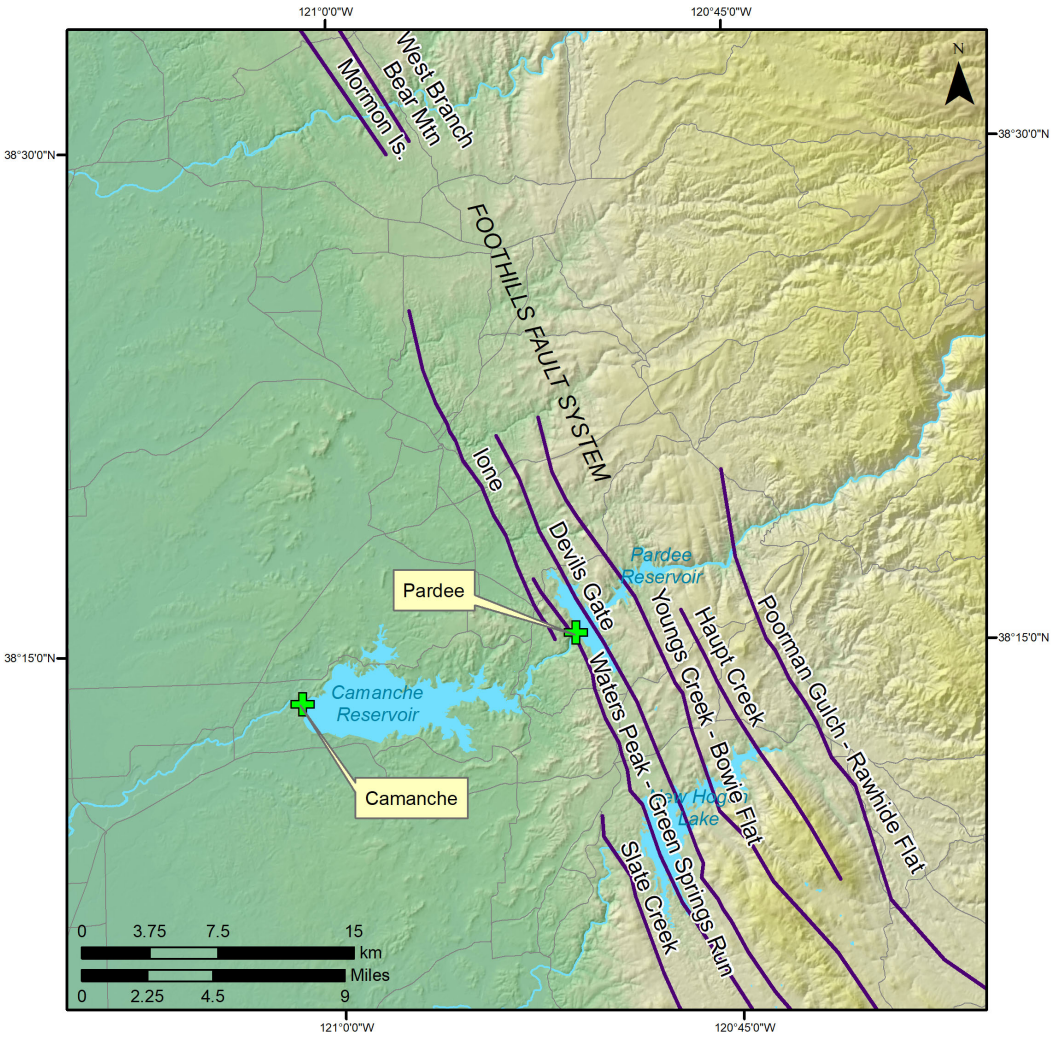

Source: Faults from AECOM seismic source model and LCI (2020)

Figure 4-2. The Foothills Fault System near Pardee and Camanche Dams

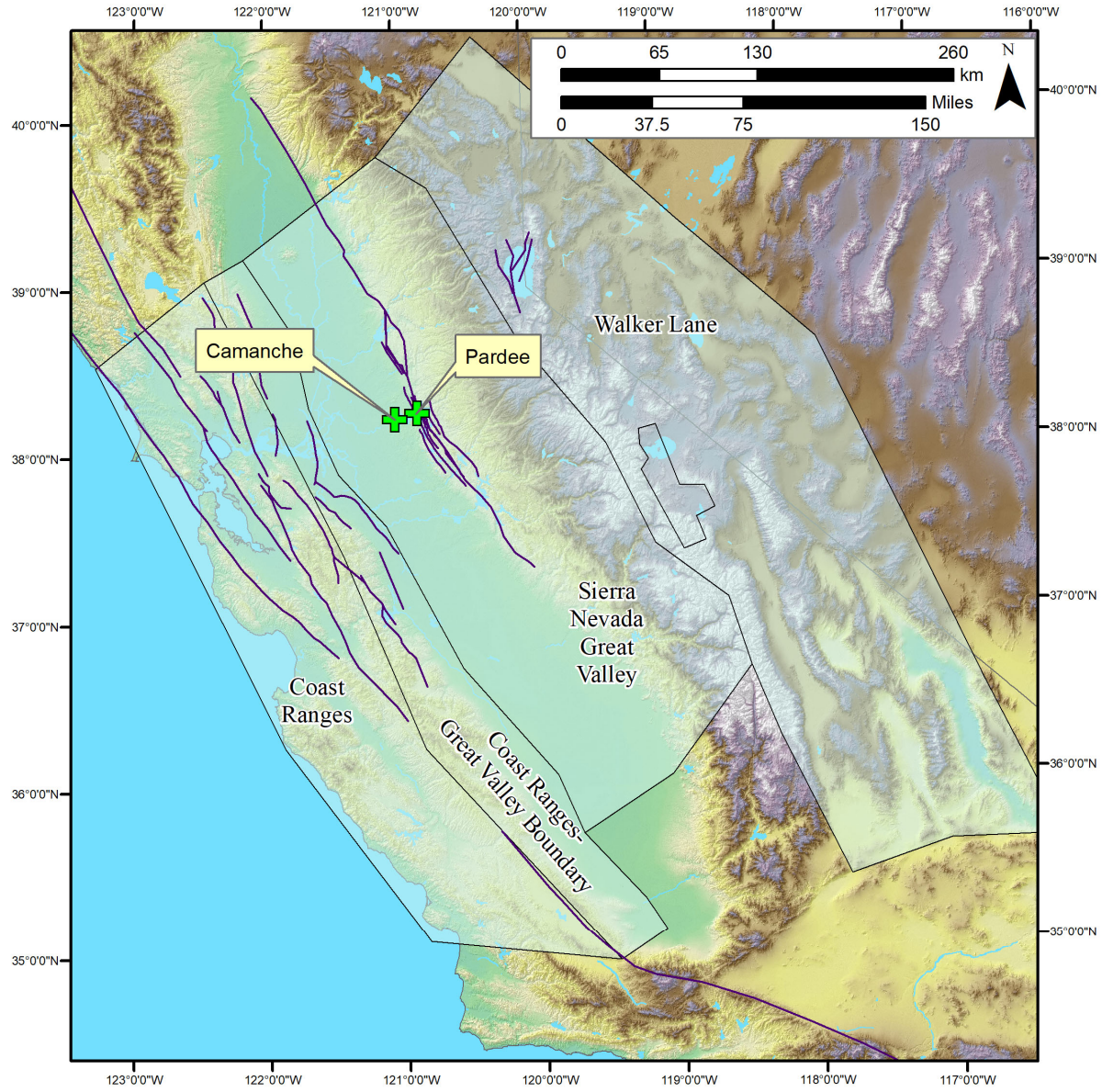

Figure 4-3. Regional Seismic Source Zones

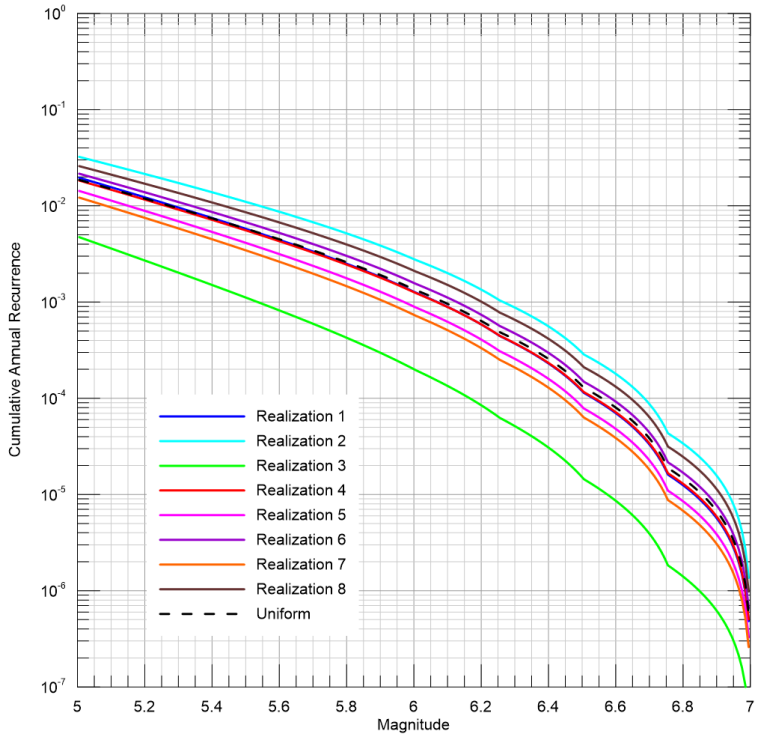

Figure 4-4. Magnitude Recurrence Curves for SNGV Seismic Source Zone

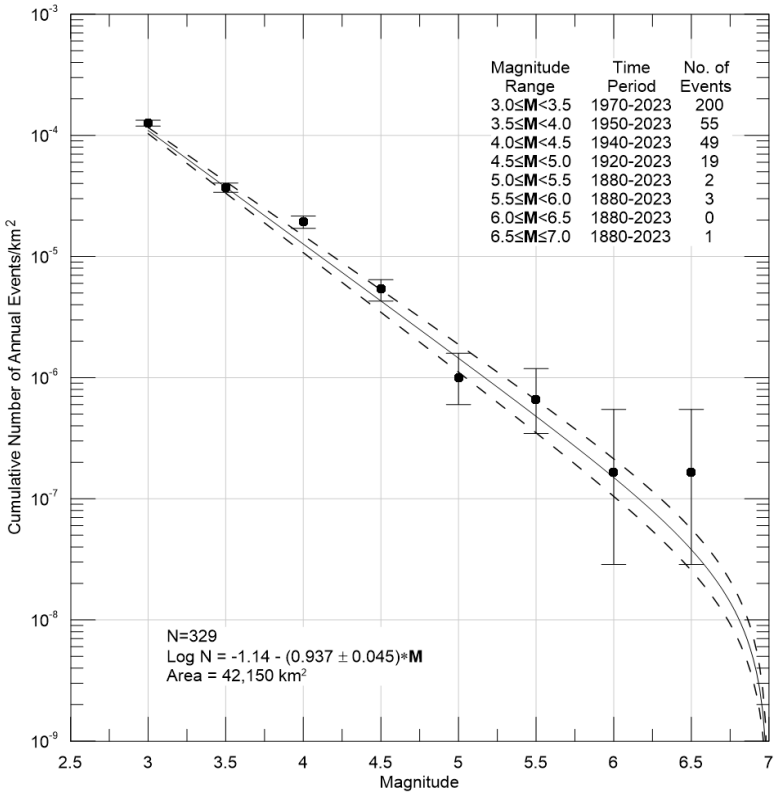

Figure 4-5. Earthquake Recurrence for the CR Seismic Source Zone

4.2 Geologic Site Conditions

4.2.1 Pardee Dam

Pardee Reservoir is within a northwest-trending belt of metamorphic rocks known as the foothills metamorphic belt. This metamorphic belt consists of several distinct, northwest-trending fault-bounded bands of Mesozoic and Paleozoic metamorphic rocks that extend for over 390 km along the western foothills of the north-central Sierra Nevada. In the vicinity of Pardee Dam, these rocks consist of the Jurassic-age Gopher Ridge Volcanics and Salt Springs Slate. The Salt Springs Slate stratigraphically overlies and interfingers with the Gopher Ridge Volcanics. On a regional scale, the volcanics typically form resistant ridges with the weaker, interbedded slates forming narrow valleys throughout the foothills. Locally (at the outcrop scale), thin (≤ 15 m thick) beds of slate occur within the metavolcanic rocks (Jacobs Associates, 2013)

The Gopher Ridge metavolcanics is the primary rock unit at the Pardee Dam and spillway and is composed mostly of pyroclastic and flow rocks. This formation is exposed nearly continuously along the northern and southern banks of the Mokelumne River canyon from Pardee Dam downstream to near the confluence with Mexican Gulch, a distance of about 185 m. The rock is referred to as "greenstone" in older reports addressing the dam foundation. The physical characteristics of the rock (i.e., competence) vary at the surface with degree of weathering. The rock is described as predominantly massive, strong and hard, and provides a competent foundation for the dam. The rock is jointed at fairly wide spacing (typically several meters). The foundation rock has essentially no primary permeability, and water flow occurs only through joints and fractures (EBMUD/GEI, 2013).

HCG (1997) performed multiple seismic refraction surveys at Pardee Dam and Spillway. The compressional wave velocities (Vp) indicate three primary velocity horizons. The upper zone corresponds to residual soils and intensely weathered bedrock to a depth of 3 m. The Vp ranged from 323 to 975 m/sec. The second horizon is about 6 to 21 m thick with Vp ranging from 1,600 to 2204 m/sec corresponding to moderately weathered and intensely to moderately fractured bedrock. The third zone was reported to be slightly weathered to fresh, moderately fractured bedrock with Vp ranging from 3,048 to 5,060 m/sec. Using a Poisson's Ratio of 0.3, typical for competent rock, a time average shear-wave velocity (V_S) in the upper 30 m (V_{S30}) was calculated to be 1,377 m/sec for the average profile, excluding the upper zone. The V_{S30} values range from 1,185 m/sec to 1,660 m/sec.

More recently, downhole P- and S-wave measurements from three borings at the Pardee Dam site, all within the Gopher Ridge Volcanics, indicate the shear-wave velocity ranges from about 372 m/sec to 2,900 m/sec in reasonable agreement with the seismic refraction results. The average Vs was about 1,307 m/sec over a total depth of about 39 m (Jacobs Associates, 2013).

Based on the above data, a V_{S30} of 1,300 m/sec was used in the seismic hazard analysis. To address epistemic uncertainty and to account for spatial variability of the V_S below the dam site and spillway, an uncertainty of ± 100 m/sec in the V_{S30} was included in the hazard analysis. The use of this V_{s30} assumes the dam is founded on moderately to slightly weathered to fresh, moderately fractured bedrock, which is consistent with the visual reports of rock outcropping at the dam site. If it is determined that weathered bedrock or residual soils are present in the dam foundation, the use of V_{s30} may not be appropriate to address site effects and a site-response analysis should be considered.

4.2.2 Camanche Dam

Camanche Dam was excavated directly into the Miocene-Pliocene Mehrten and the Oligocene-Miocene Valley Springs Formations on the western end of Camanche Reservoir. The Mehrten formation varies in rock type from mudflow or agglomerate, to conglomerate, sandstone, siltstone, and claystone. The most widespread sediments in the Mehrten formation are the sandstones which comprise over 50-percent of the material. They also occur as lenticular bodies and may be seen grading into siltstones at one extreme and into conglomerates at the other (Bechtel, 1961). The Valley Springs Formation consists of interbedded fluvial deposits (siltstone, sandstone, and conglomerate) and rhyolitic tuffs. Beds within the Valley Springs Formation are relatively continuous laterally. For about 366 m across the flood plain, the upstream and downstream shells of the Main Dam are founded on dredge tailings, specifically reworked river sands and gravels. (Rizzo, 2018).

Downhole seismic velocity measurements were collected from eighteen wells at the Main Dam, Dike 2 and Dike 5 (Terra/GeoPentech, 2010). Sixteen of these wells collected data in the Mehrten and Valley Springs Formation, which in many cases were overlain with older alluvium or dredge tailings. For most wells single V_S values were reported for each Formation. The downhole measurements sampled the two Formations over thicknesses ranging from about 1 m to 27 m, with an average of 9.5 m. For the purpose of calculating a V_{S30}, it was assumed the reported V_S extend to 30 m. The average V_{S30} of the Mehrten and Valley Springs Formation is about 760 m/sec, which was used in the hazard analyses. The minimum Vs value is 418 m/sec and the maximum of 1,162 m/sec. At the dam location, the range of Vs values is 654 to 1,070 m/sec. To account for spatial variability and capture the range of V_S values below the dam site, an uncertainty of ± 100 m/sec in the V_{S30} was included in the hazard analysis. This also covers approximately ± one standard deviation calculated from the 16 Vs values. This assumes the dam foundation consists of the Mehrten and Valley Springs Formations. If it is determined in future studies that older alluvium or weathered and/or intensely fractured rock is present in the foundation, a site-response analysis may need to be performed depending on the site-specific Vs profile.

4.3 Ground Motion Models

To estimate the ground motions for crustal earthquakes in the PSHA, ground motion models appropriate for tectonically active crustal regions were used.

The models appropriate for shallow crustal earthquakes in active tectonic regions, developed as part of the Next Generation of Attenuation (NGA)-West2 Project sponsored by PEER Center Lifelines Program, were published in 2014. The NGA-West1 Project began in 2003, and in 2008 the first set of models became available. The NGA West-1 models had a substantially better scientific basis than past relationships, which generally dated around 1997 (e.g., Abrahamson and Silva, 1997), because they were developed through the efforts of five selected ground motion developer teams working in a highly interactive process with other researchers who: (a) developed an expanded and improved database of strong ground motion recordings and supporting information on the causative earthquakes, the source-to-site travel path characteristics, and the site and structure conditions at ground motion recording stations; (b) conducted research to provide improved understanding of the effects of various parameters and effects on ground motions that are used to constrain models; and (c) developed improved statistical methods to develop ground motion relationships including uncertainty quantification. The NGA-West1 models benefited greatly from a large amount of new strong motion data from large earthquakes (**M** > 7) at close distances (< 25 km). Data include records from the 1999 **M** 7.6 Chi Chi, Taiwan, 1999 **M** 7.4 Kocaeli, Turkey, and 2002 **M** 7.9 Denali, Alaska earthquakes. The NGA-West2 models were developed based on an expanded strong motion database compared to the initial NGA database. A number of more recent well recorded earthquakes were added to the NGA-West2 database including the Wenchuan, China, numerous moderate magnitude California events down to **M** 3.0, and several Japanese, New Zealand, and Italian earthquakes.

The NGA-West2 models by Abrahamson et al. (2014, [ASK14]), Boore et al. (2014, [BSSA14]), Campbell and Bozorgnia (2014, [CB14]) and Chiou and Youngs (2014, [CB14]) were used in the PSHA and DSHA. The Idriss (2014) model was not included as it lacks important features not included in the other models, such as the distinction between normal and strike-slip faulting, and a hanging wall term. The most recent USGS National Seismic Hazard maps exclude the Idriss (2014) model (Petersen et al., 2020).

The NGA-West2 models are not well constrained for normal faulting, such as the Foothills fault system, due to a general sparsity of strong motion data for normal-faulting earthquakes, particularly for **M** ≥ 6, used in the development of the models. Based on interaction with FERC for dams in extensional tectonic regions, normal faults were modeled as a strike-slip fault and a normal fault, each equally weighted.

FERC (2018) states only the NGA-West2 ground motion models which explicitly account for the effects of the hanging wall, the ASK14, CB14 and CY14 models, should be included for the faults on which the site is on the hanging wall.

Based on the geologic site conditions and geophysical data at Pardee Dam (Section 4.2.1), the V_{S30} was estimated to be 1,300 ± 100 m/sec. However as described by Al Atik et al. (2022) empirical ground-motion models such as the NGA-West2 ground motion models are limited in the number of recordings on hard-rock stations used to develop the models. Therefore, the site response scaling in the ground motions

models cannot be reliably extrapolated to hard-rock conditions. The PSHA was calculated for a V_{S30} of 760 m/sec and the linear site adjustment factors of Al Atik et al. (2022) were used to adjust the median ground motions to a hard-rock site condition of V_{S30} of 1,300 ± 100 m/sec.

Input parameters for the NGA-West2 models include $Z_{1.0}$, the depth of a V_S of 1.0 km/sec and $Z_{2.5}$, the depth to a V_S of 2.5 km/sec. Both parameters were used by some of the developers as proxies for basin effects. $Z_{1.0}$ is used by CY14 and ASK14 and $Z_{2.5}$ is used in CB14. If site-specific data are not available, the authors have provided models to determine $Z_{1.0}$ and $Z_{2.5}$. Based on the V_{S30} of 1,300 m/sec at Pardee Dam a $Z_{1.0}$ of 0.001 km and a $Z_{2.5}$ of 0.328 km were used in the hazard analysis. At Camanche Dam a $Z_{1.0}$ of 0.045 km and a $Z_{2.5}$ of 0.607 km were used in the hazard analysis based on a V_{S30} of 760 m/sec. Other parameters such as depth to the top of rupture (zero for all faults that intersect the surface unless specified otherwise), dip angle, rupture width, and aspect ratio were specified for each fault or calculated within the PSHA code.

As noted by Al Atik and Youngs (2014) the development of the NGA-West2 models was a collaborative effort with many interactions and exchanges of ideas among the developers, and the developers indicated that an additional epistemic uncertainty needs to be incorporated into the median ground motions in order to more fully represent an appropriate level of epistemic uncertainty. Hence, for each of the four models, an additional epistemic uncertainty on the median ground motion was included. The three-point distribution and model of Al Atik and Youngs (2014) was applied (Figure 2-1). The model is a function of magnitude, style of faulting, and spectral period.

5. Seismic Hazard Results

5.1 Pardee Dam PSHA Results

The PSHA at Pardee was calculated for a site condition with a V_{S30} of 760 m/sec (Section 4.2.1), then as discussed in Section 4.3, the uniform hazard response spectra (UHRS) are converted to hazard rock site conditions of V_{S30} of 1,300 ± 100 m/sec using the linear site adjustment factors of Al Atik et al. (2022). The V_{S30} range is to account for the epistemic uncertainty in the adopted value in addition to the spatial variability in V_{S30} at the dam site.

The results of the PSHA are presented in terms of ground motion as a function of annual exceedance frequency. This frequency is the reciprocal of the average return period. Figures 5-1 and 5-2 show the mean, median (50th percentile), 5th, 15th, 85th, and 95th percentile hazard curves for the PGA and 1.0 sec spectral accelerations (SA). The fractiles indicate the range of uncertainties about the mean hazard. At a return period of 10,000 years, there is a factor of 2.7 difference between the 5th and 95th percentile hazard at PGA (Figure 5-1) and a factor of 2.0 at 1.0 sec SA (Figure 5-2). The PGA and 1.0 sec SA for select return periods and fractiles are listed in Table 5-1.

The contributions of the various seismic sources to mean PGA and 1.0 sec SA hazard are shown on Figures 5-3 and 5-5. The fractional contribution of seismic sources as a percent of the total mean hazard is presented on Figures 5-4 and 5-6. At PGA and return period less than about 1,000-years, the more distant, highly active faults, such as the San Andreas, Calaveras and Hayward, contribute the most to the total mean hazard. The SNGV background zone is also a significant source over most return periods. For return periods greater than about 1,000-years, the faults of the Foothills fault system contribute the most to the total mean hazard. Figure 5-4 shows the fractional contributions of significant sources as well as the combined hazard for the Foothills fault system faults, for all other faults, and for all background sources. The Foothills fault system contributes almost 90-percent of the total mean hazard at a return period of 10,000-years (Figure 5-4). The unusual shape of the mean hazard curve (Figure 5-3), is a result of the low-slip rates for the faults of the Foothills fault system, which contribute very little at short return periods, but contribute significantly at longer return periods due to their proximity to Pardee Dam. Whereas the more distant, highly active faults contribute significantly at short return periods, but due to the relatively large distance to the dam site, their contribution diminishes at longer return periods (Figure 5-3). At 1.0 sec SA, the hazard contributions are similar (Figures 5-5 and 5-6), however the more distance faults, especially the San Andreas contribute more to the total mean hazard, and the SNGV background contributes much less, in part due to the relatively low seismicity in the region (Figure 3-1).

Figures 5-7 to 5-12 illustrate the proportional contributions after deaggregating the mean PGA and 1.0 sec SA hazard by magnitude, distance and epsilon bins for 950-, 2,475- and 10,000-year return periods. Epsilon is the difference between the logarithm of the ground motion amplitude and the mean logarithm of ground motion (for that M and R) measured in units of the standard deviation (σ) of the logarithm of the median ground motion. Therefore, an epsilon greater than zero represents an above-average ground motion. Also included in Figures 5-7 to 5-12 is a plot with the magnitude deaggregation for all distances combined. The hazard at PGA and return periods of 950-years and greater is dominated by events at distances of 0-20 km with magnitudes ranging from **M** 5.0 to 7.0, representing the Foothill fault system. At 1.0 sec SA the hazard is bimodal, with contributions from the Foothill fault system at distances less than 20 km and magnitudes ranging from **M** 5.0 to 7.0, but also from the San Andreas fault at a distance of 160 km and magnitudes ranging from **M** 7.5 to 8.6. Based on the magnitude and distance bins (e.g., Figures 5-7 to 5-12), the controlling earthquakes as defined by the modal magnitude **M***, distance D*, and epsilon ε* can be calculated. Table 5-2 lists the **M***, D*, and ε* for PGA and 1.0 sec SA at the return periods of interest. Table 5-3 lists the **M*** and D* when the epsilons are combined for each magnitude-distance bin. Table 5-4 lists the mean $\overline{M}$, $\overline{D}$, $\bar{\varepsilon}$ values. Also provided are the mean $\overline{M}$ and $\overline{D}$ for the significant contributing sources (Table 5-5).

The sensitivities of the PGA and 1.0 sec SA hazard to selection of ground-motion models are shown on Figures 5-13 and 5-14. Each hazard curve shown is calculated using only that model. The other ground motion models are general similar, though the ASK14 model gives slightly higher ground motions at PGA, while the CB14 and CY14 models give the highest ground motions at 1.0 sec SA.

Sensitivity of the unform and gridded background seismicity for the seismic sources zones at PGA is shown on Figure 5-15. Given the relatively low seismicity in the region, the uniform seismicity for the SNGV contributes the most to the total mean hazard over most return periods of interest. For the SNGV, WL and CRGVB seismic zones the uniform seismicity contributes more to the total mean hazard, than the smoothed seismicity, again, due to the relatively low seismicity in the region. For the CR seismic zone, the uniform and smoothed seismicity contribute similarly to the total mean hazard, as a result of the relatively high rate of seismicity.

The UHRS for a range of return periods from 144- to 10,000-years are shown on Figure 5-16. The UHRS have been converted to hard rock using the linear site adjustment factors of Al Atik et al. (2022). These UHRS reflect the geometric mean of expected horizontal ground motions as predicted by the ground-motion models. Figure 5-17 shows the range in epistemic uncertainty in the 2,475-year return period UHRS. The return period of PGA at the 95th percentile level computed from the mean hazard curve is 5,200-years and at 1.0 sec SA value the return period is 4,600-years. The 5th and 95th percentile UHRS differ by an average factor of 2.6. These ranges represent the uncertainty modeled in the PSHA based on our current knowledge of all inputs. Additional information on seismic sources or future refinement of ground-motion models would likely decrease the range of uncertainty, but the mean may shift within this range.

The sensitivity of the UHRS to the selection of V_{S30} is shown on Figure 5-18. A V_{S30} of 1,400 m/sec gives the largest ground motions for periods less than 0.3 sec, with a V_{S30} of 1,200 m/sec giving the largest ground motions for longer periods. The difference in the UHRS is around 10-percent at periods of 0.03 to 0.15 sec, but less than 5-percent at longer periods and at PGA. The recommended UHRS is the envelope of the V_{S30} and these values. All hard rock UHRS values are provided in Tables 5-6 to 5-9.

Because Pardee Dam is at near-fault distances from the Foothills fault system, the effect of forward rupture directivity was explored. Fault directivity is discussed in more detail in Section 5.2. The PSHA was run with fault directivity for the Foothills fault system using the model of Bayless and Somerville, developed as part of the NGA-West2 Directivity Working Group (Spudich et al. 2013), which is an update to the widely used model of Somerville et al. (1997). In the PSHA, directivity had minimal effect at Pardee dam, less than 1 percent at a period of 10 sec, and is therefore not included in the in the tables or figures below. This is due in large part to the randomization of the hypocenter in the PSHA code and that dip-slip faults generally have lower directivity effects than strike-slip faults.

Table 5-1. Pardee Dam Summary of Horizontal Probabilistic Ground Motions (V_{S30} = 760 m/sec)

Return Period (years)	PGA (g) Mean [5th, 95th percentile]	1.0 Sec SA (g) Mean [5th, 95th percentile]
144	0.0543 [0.0432, 0.0660]	0.0456 [0.0361, 0.0549]
475	0.0866 [0.0661, 0.113]	0.0706 [0.0568, 0.0847]
950	0.117 [0.0845, 0.164]	0.0900 [0.0718, 0.110]
2,475	0.193 [0.120, 0.305]	0.128 [0.0982, 0.162]
5,000	0.296 [0.160, 0.450]	0.168 [0.124, 0.231]
10,000	0.433 [0.227, 0.616]	0.227 [0.156, 0.330]

Table 5-2. Pardee Dam Modal Magnitude, Distance and Epsilon

Period (sec)	Return Period:	144-year	475-year	950-year	2,475-year	5,000-year	10,000-year
PGA	M*	6.7	7.9	6.1	5.9	6.1	6.1
	D* (km)	95.0	162.5	5.0	5.0	5.0	5.0
	ε*	1.5	1.5	-1.5	-0.5	-0.5	0.5
1.0 sec SA	M*	7.1	7.7	7.9	6.1	5.9	6.1
	D* (km)	162.5	162.5	162.5	5.0	5.0	5.0
	ε*	1.5	1.5	1.5	-0.5	0.5	0.5

Table 5-3. Pardee Dam Modal Magnitude and Distance (combined epsilon)

Period (sec)	Return Period:	144-year	475-year	950-year	2,475-year	5,000-year	10,000-year
PGA	M*	6.7	5.9	5.9	6.1	6.1	6.1
	D* (km)	95.0	5.0	5.0	5.0	5.0	5.0
1.0 sec SA	M*	7.9	7.9	7.9	6.1	6.1	6.1
	D* (km)	162.5	162.5	162.5	5.0	5.0	5.0

Table 5-4. Pardee Dam Mean Magnitude, Distance and Epsilon

Period (Sec)	Return Period:	144-year	475-year	950-year	2,475-year	5,000-year	10,000-year
PGA	$\bar{M}$	6.6	6.4	6.3	6.1	6.0	6.1
	$\bar{D}$ (km)	94.8	68.5	47.0	20.3	10.3	6.9
	$\bar{\varepsilon}$	0.9	0.7	0.4	0.2	0.3	0.6
1.0 sec SA	$\bar{M}$	6.9	6.9	6.9	6.7	6.6	6.4
	$\bar{D}$ (km)	120.7	108.0	94.6	68.1	46.8	26.8
	$\bar{\varepsilon}$	1.3	1.5	1.4	1.2	1.0	0.9

Table 5-5. Pardee Dam Mean Magnitude and Distance for Significant Seismic Sources

Period (sec)	Source	Return Period:	144-year	475-year	950-year	2,475-year	5,000-year	10,000-year
PGA	Waters Peak-Green Springs Run	M*	5.9	5.9	6.0	6.0	6.0	6.1
		D* (km)	18.8	16.3	14.2	11.8	8.1	6.2
	Devils Gate	M*	5.8	5.8	5.8	5.8	5.9	5.9
		D* (km)	7.2	6.7	6.3	5.6	4.3	3.5
	Ione	M*	5.8	5.9	5.9	5.9	6.0	6.1
		D* (km)	8.1	7.8	7.5	7.1	6.1	5.4
	SNGV	M*	5.6	5.6	5.6	5.6	5.7	5.7
		D* (km)	60.3	48.6	41.9	35.5	26.8	22.2
	San Andreas (Unseg)	M*	7.9	8.0	8.0	8.1	8.2	8.2
		D* (km)	157.0	156.1	155.8	155.5	155.3	155.2
1.0 sec SA	Waters Peak-Green Springs Run	M*	6.0	6.1	6.1	6.1	6.2	6.2
		D* (km)	16.7	12.1	12.1	10.2	8.4	6.8
	Devils Gate	M*	5.8	5.9	5.9	5.9	5.9	6.0
		D* (km)	6.4	5.2	5.2	4.6	4.0	3.4
	Ione	M*	5.9	6.0	6.0	6.1	6.1	6.2
		D* (km)	7.3	6.4	6.4	6.0	5.6	5.1
	SNGV	M*	5.9	6.0	6.0	6.1	6.1	6.1
		D* (km)	69.3	45.8	45.6	37.8	30.7	24.7
	San Andreas (Unseg)	M*	7.7	7.9	7.9	8.0	8.0	8.1
		D* (km)	161.3	157.3	157.3	156.6	156.1	155.7

Table 5-6. Pardee Dam 5%-Damped Mean Horizontal UHRS (V_{S30} = 1,200 m/sec)

Return Period:	144-year	475-year	950-year	2,475-year	5,000-year	10,000-year
Period (sec)	**SA (g)**	**SA (g)**	**SA (g)**	**SA (g)**	**SA (g)**	**SA (g)**
0.010 (PGA)	0.0498	0.0794	0.107	0.177	0.271	0.397
0.030	0.0583	0.0939	0.128	0.215	0.334	0.491
0.050	0.0788	0.130	0.178	0.305	0.475	0.697
0.100	0.112	0.186	0.257	0.448	0.700	1.04
0.150	0.122	0.199	0.271	0.469	0.740	1.10
0.200	0.113	0.181	0.243	0.411	0.642	0.960
0.300	0.0968	0.151	0.197	0.308	0.460	0.684
0.400	0.0792	0.122	0.157	0.235	0.337	0.492
0.500	0.0669	0.103	0.132	0.192	0.267	0.382
0.600	0.0570	0.0876	0.112	0.161	0.219	0.310
0.750	0.0475	0.0733	0.0936	0.133	0.178	0.245
1.000	0.0343	0.0531	0.0676	0.0959	0.126	0.171
1.500	0.0222	0.0343	0.0437	0.0610	0.0785	0.102
2.000	0.0156	0.0245	0.0313	0.0436	0.0557	0.0712
3.000	0.00944	0.0153	0.0196	0.0273	0.0346	0.0437
4.000	0.00678	0.0108	0.0141	0.0197	0.0250	0.0313
5.000	0.00543	0.00855	0.0111	0.0159	0.0203	0.0254
7.500	0.00405	0.00642	0.00839	0.0121	0.0159	0.0201
10.000	0.00328	0.00517	0.00674	0.00972	0.0127	0.0165

Table 5-7. Pardee Dam 5%-Damped Mean Horizontal UHRS (V_{S30} = 1,300 m/sec)

Return Period:	144-year	475-year	950-year	2,475-year	5,000-year	10,000-year
Period (sec)	**SA (g)**	**SA (g)**	**SA (g)**	**SA (g)**	**SA (g)**	**SA (g)**
0.010 (PGA)	0.0505	0.0805	0.109	0.179	0.275	0.402
0.030	0.0605	0.0975	0.133	0.224	0.346	0.509
0.050	0.0833	0.137	0.188	0.322	0.502	0.737
0.100	0.118	0.196	0.271	0.473	0.737	1.09
0.150	0.127	0.207	0.283	0.490	0.772	1.15
0.200	0.116	0.185	0.248	0.419	0.655	0.980
0.300	0.0974	0.151	0.198	0.310	0.463	0.688
0.400	0.0786	0.121	0.156	0.233	0.334	0.488
0.500	0.0659	0.102	0.130	0.189	0.263	0.377
0.600	0.0561	0.0861	0.110	0.158	0.216	0.305
0.750	0.0467	0.0719	0.0919	0.131	0.175	0.241
1.000	0.0337	0.0521	0.0664	0.0941	0.124	0.168
1.500	0.0218	0.0337	0.0429	0.0599	0.0771	0.100
2.000	0.0154	0.0241	0.0308	0.0429	0.0547	0.070
3.000	0.00929	0.0150	0.0193	0.0268	0.0340	0.043
4.000	0.00668	0.0106	0.0139	0.0194	0.0246	0.0308
5.000	0.00536	0.00844	0.011	0.0157	0.0200	0.0251
7.500	0.00400	0.00634	0.00829	0.0120	0.0157	0.0199
10.000	0.00324	0.00511	0.00666	0.00961	0.0126	0.0163

Table 5-8. Pardee Dam 5%-Damped Mean Horizontal UHRS (V_{S30} = 1,400 m/sec)

Return Period:	144-year	475-year	950-year	2,475-year	5,000-year	10,000-year
Period (sec)	**SA (g)**	**SA (g)**	**SA (g)**	**SA (g)**	**SA (g)**	**SA (g)**
0.010 (PGA)	0.0512	0.0817	0.110	0.182	0.279	0.409
0.030	0.0628	0.101	0.138	0.232	0.360	0.529
0.050	0.0875	0.144	0.198	0.339	0.527	0.774
0.100	0.123	0.205	0.283	0.494	0.770	1.14
0.150	0.131	0.214	0.293	0.507	0.798	1.19
0.200	0.117	0.188	0.252	0.425	0.664	0.994
0.300	0.0977	0.152	0.198	0.311	0.464	0.690
0.400	0.0779	0.120	0.155	0.231	0.331	0.484
0.500	0.0651	0.100	0.128	0.187	0.260	0.372
0.600	0.0552	0.0848	0.108	0.155	0.212	0.300
0.750	0.0459	0.0708	0.0904	0.129	0.172	0.237
1.000	0.0331	0.0513	0.0653	0.0926	0.122	0.165
1.500	0.0214	0.0332	0.0423	0.0590	0.0758	0.0989
2.000	0.0152	0.0238	0.0303	0.0422	0.0539	0.0690
3.000	0.00916	0.0148	0.0190	0.0265	0.0336	0.0424
4.000	0.00659	0.0105	0.0137	0.0192	0.0243	0.0304
5.000	0.00529	0.00833	0.0108	0.0155	0.0198	0.0248
7.500	0.00396	0.00628	0.0082	0.0119	0.0156	0.0197
10.000	0.00321	0.00507	0.0066	0.00952	0.0125	0.0162

Table 5-9. Pardee Dam 5%-Damped Mean Horizontal UHRS (Enveloped Hard Rock)

Return Period:	144-year	475-year	950-year	2,475-year	5,000-year	10,000-year
Period (sec)	**SA (g)**	**SA (g)**	**SA (g)**	**SA (g)**	**SA (g)**	**SA (g)**
0.010 (PGA)	0.0512	0.0817	0.110	0.182	0.279	0.409
0.030	0.0628	0.101	0.138	0.232	0.360	0.529
0.050	0.0875	0.144	0.198	0.339	0.527	0.774
0.100	0.123	0.205	0.283	0.494	0.770	1.14
0.150	0.131	0.214	0.293	0.507	0.798	1.19
0.200	0.117	0.188	0.252	0.425	0.664	0.994
0.300	0.0977	0.152	0.198	0.311	0.464	0.690
0.400	0.0792	0.122	0.157	0.235	0.337	0.492
0.500	0.0669	0.103	0.132	0.192	0.267	0.382
0.600	0.0570	0.0876	0.112	0.161	0.219	0.310
0.750	0.0475	0.0733	0.0936	0.133	0.178	0.245
1.000	0.0343	0.0531	0.0676	0.0959	0.126	0.171
1.500	0.0222	0.0343	0.0437	0.0610	0.0785	0.102
2.000	0.0156	0.0245	0.0313	0.0436	0.0557	0.0712
3.000	0.00944	0.0153	0.0196	0.0273	0.0346	0.0437
4.000	0.00678	0.0108	0.0141	0.0197	0.0250	0.0313
5.000	0.00543	0.00855	0.0111	0.0159	0.0203	0.0254
7.500	0.00405	0.00642	0.00839	0.0121	0.0159	0.0201
10.000	0.00328	0.00517	0.00674	0.00972	0.0127	0.0165

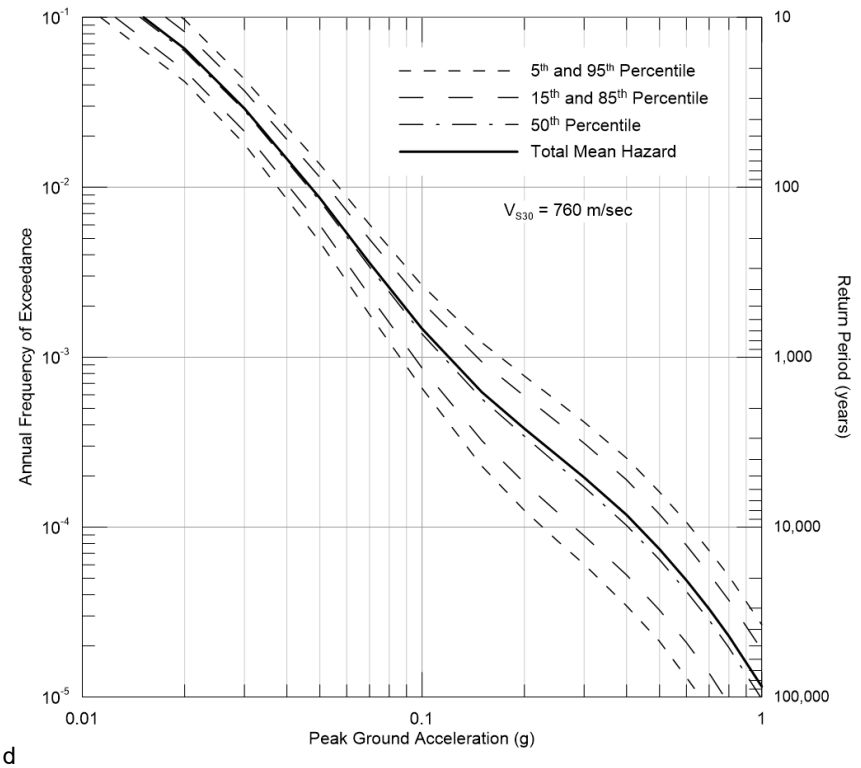

d

Figure 5-1. Pardee Dam Seismic Hazard Curves for Peak Ground Acceleration

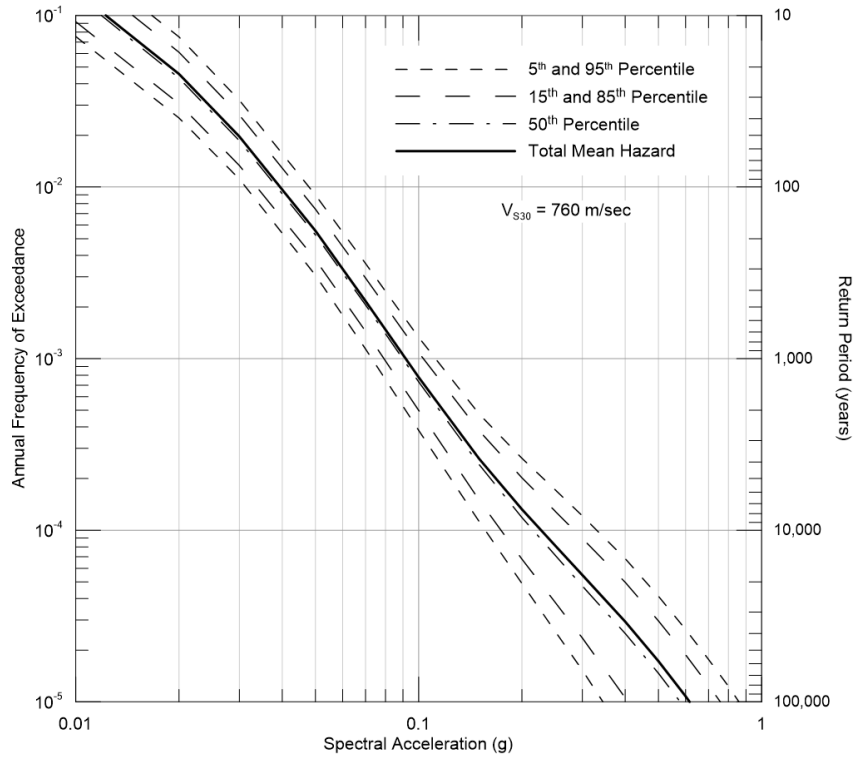

Figure 5-2. Pardee Dam Seismic Hazard Curves for 1.0 Sec Spectral Acceleration

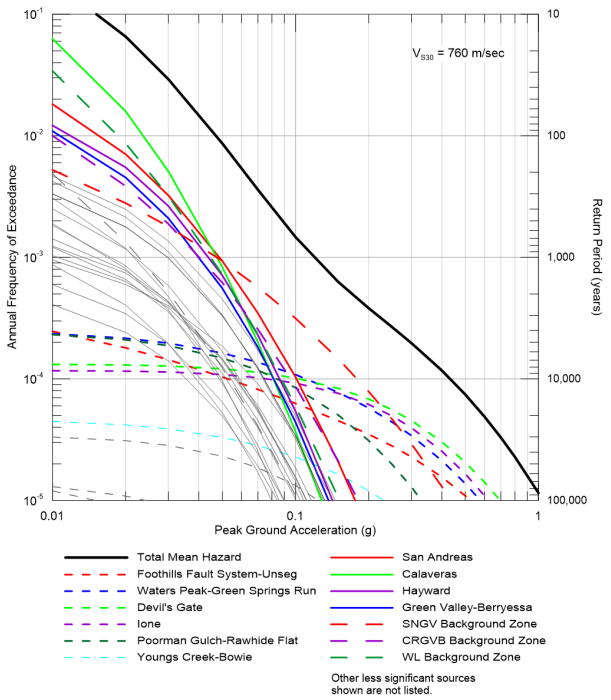

Figure 5-3. Pardee Dam Seismic Source Contributions to Mean Horizontal Peak Ground Acceleration Hazard

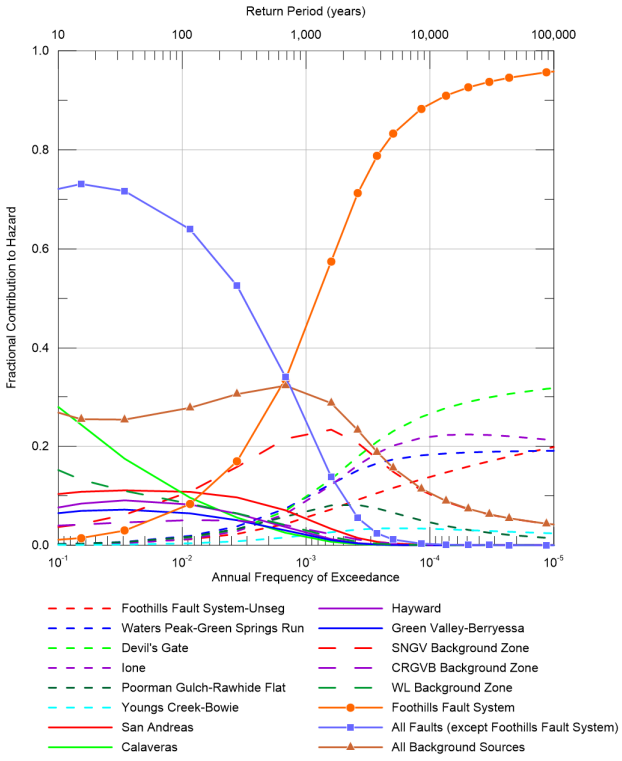

Figure 5-4. Pardee Dam Seismic Source Fractional Contributions to Mean Horizontal Peak Ground Acceleration Hazard

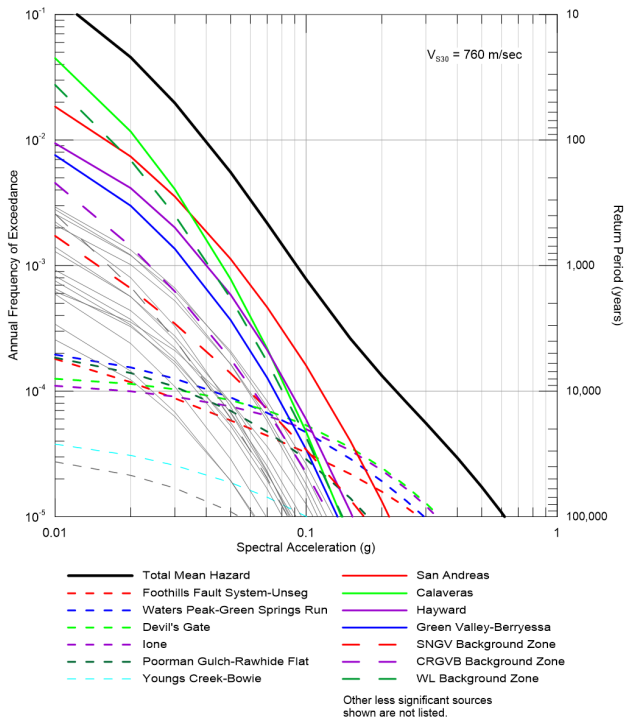

Figure 5-5. Pardee Dam Seismic Source Contributions to Mean Horizontal 1.0 Sec Spectral Acceleration Hazard

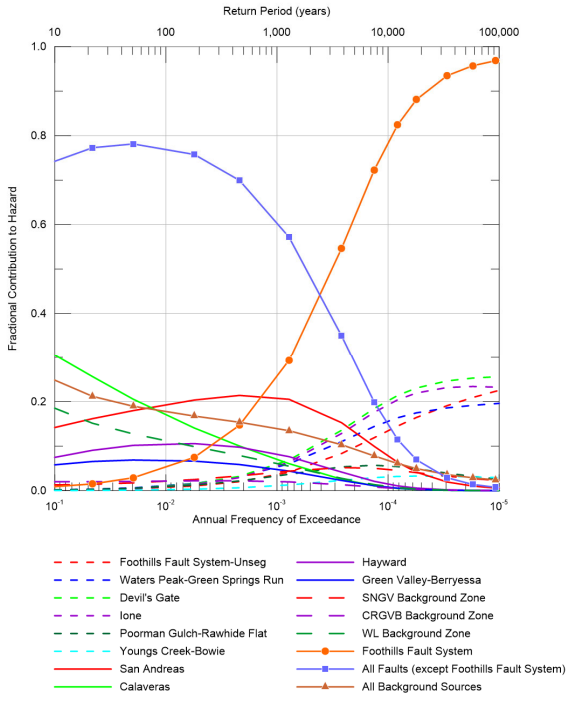

Figure 5-6. Pardee Dam Seismic Source Fractional Contributions to Mean Horizontal 1.0 Sec Spectral Acceleration Hazard

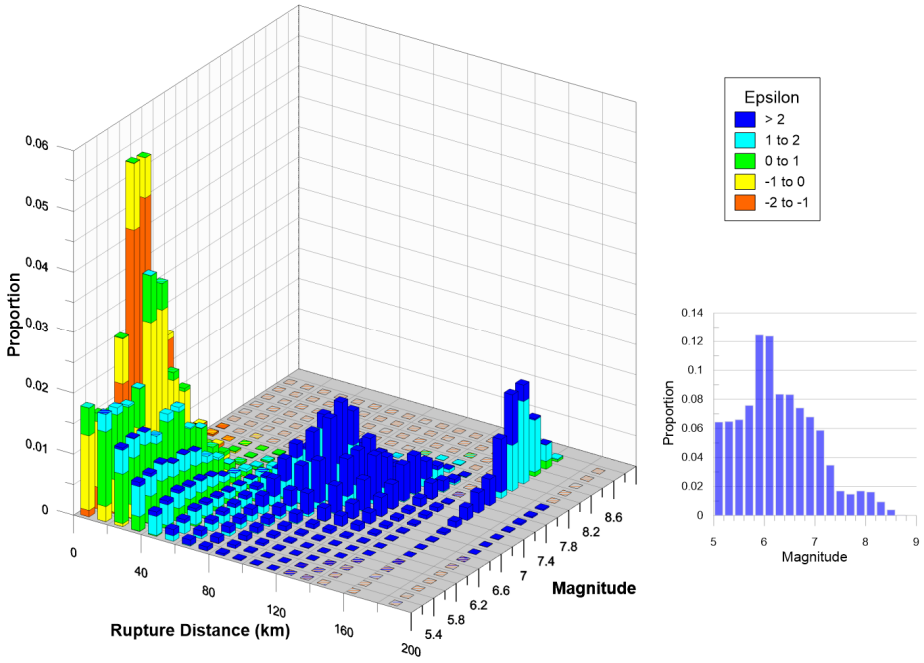

Figure 5-7. Pardee Dam Magnitude and Distance Contributions to the Mean Horizontal Peak Ground Acceleration Hazard at 950-Year Return Period

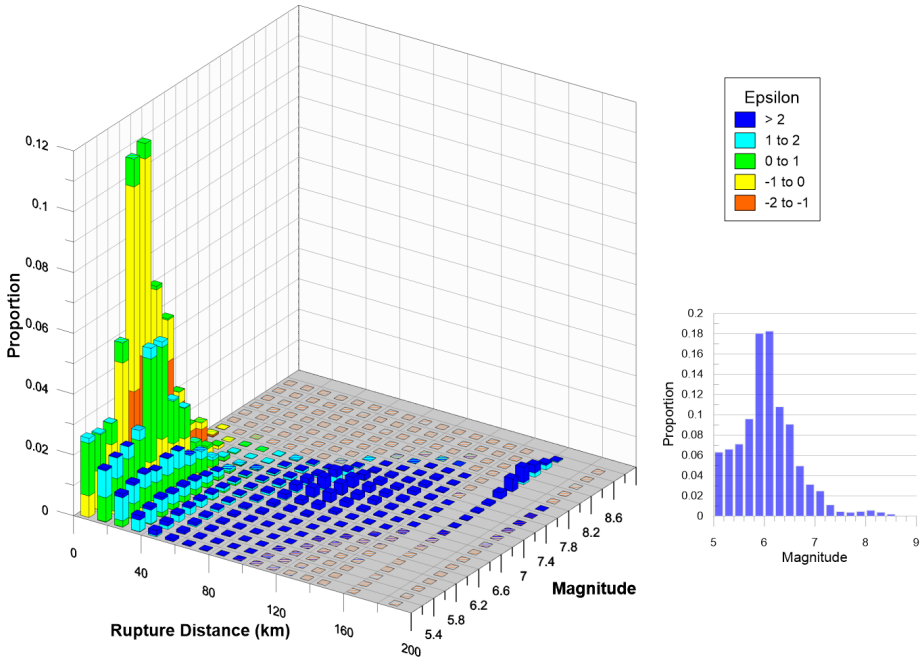

Figure 5-8. Pardee Dam Magnitude and Distance Contributions to the Mean Horizontal Peak Ground Acceleration Hazard at 2,475-Year Return Period

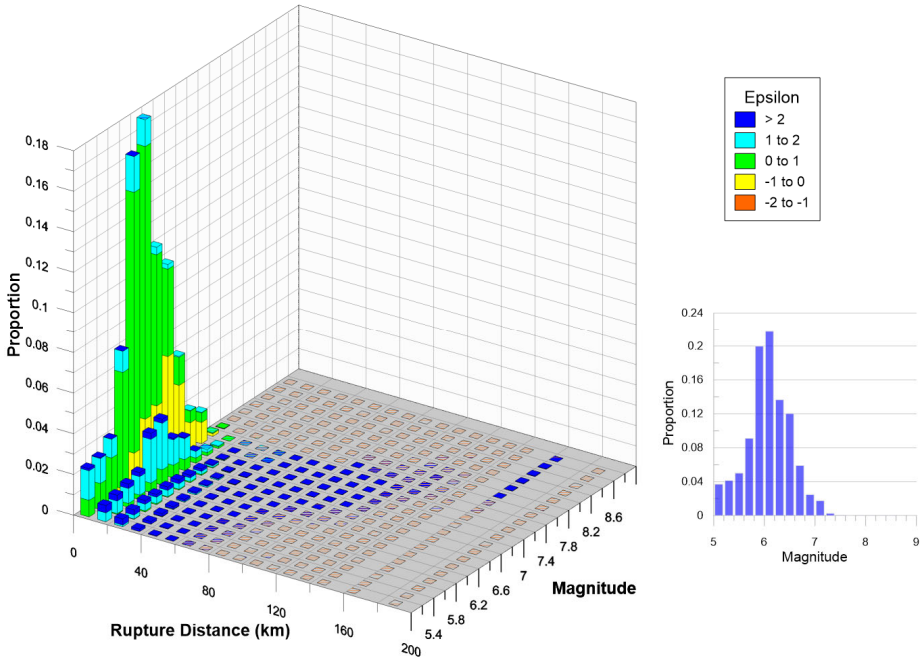

Figure 5-9. Pardee Dam Magnitude and Distance Contributions to the Mean Horizontal Peak Ground Acceleration Hazard at 10,000-Year Return Period

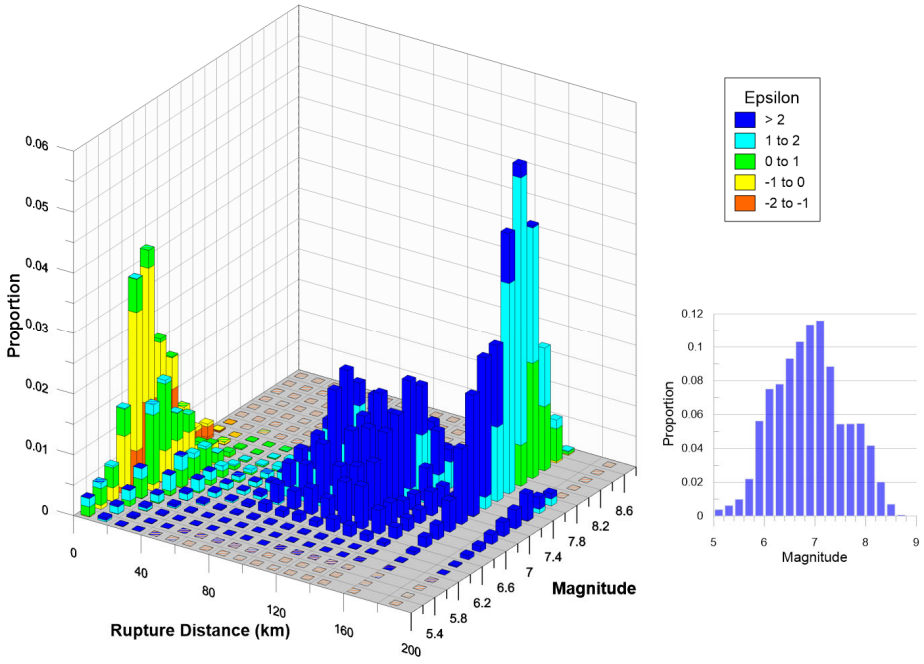

Figure 5-10. Pardee Dam Magnitude and Distance Contributions to the Mean Horizontal 1.0 Sec Spectral Acceleration Hazard at 950-Year Return Period

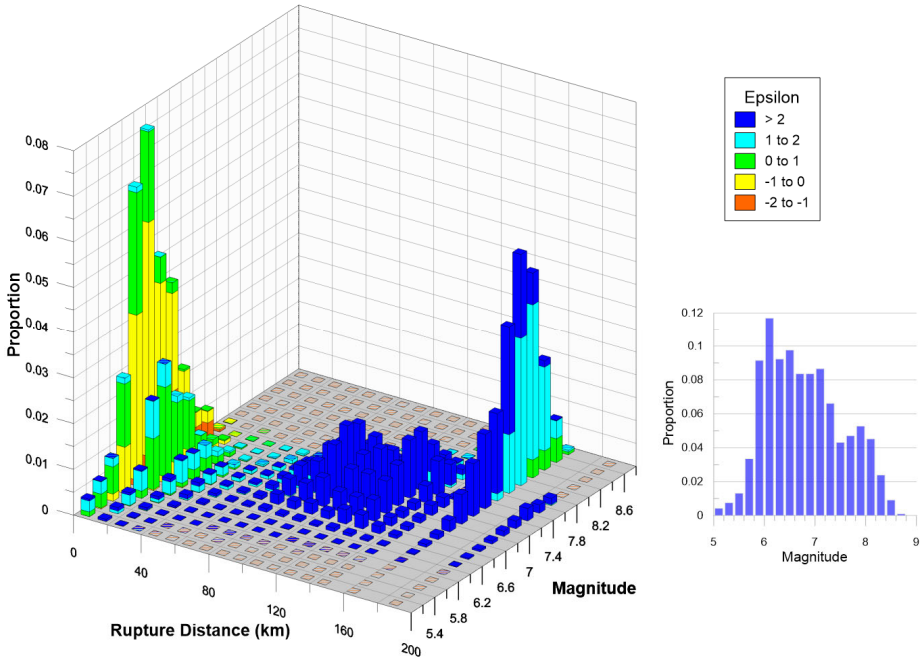

Figure 5-11. Pardee Dam Magnitude and Distance Contributions to the Mean Horizontal 1.0 Sec Spectral Acceleration Hazard at 2,475-Year Return Period

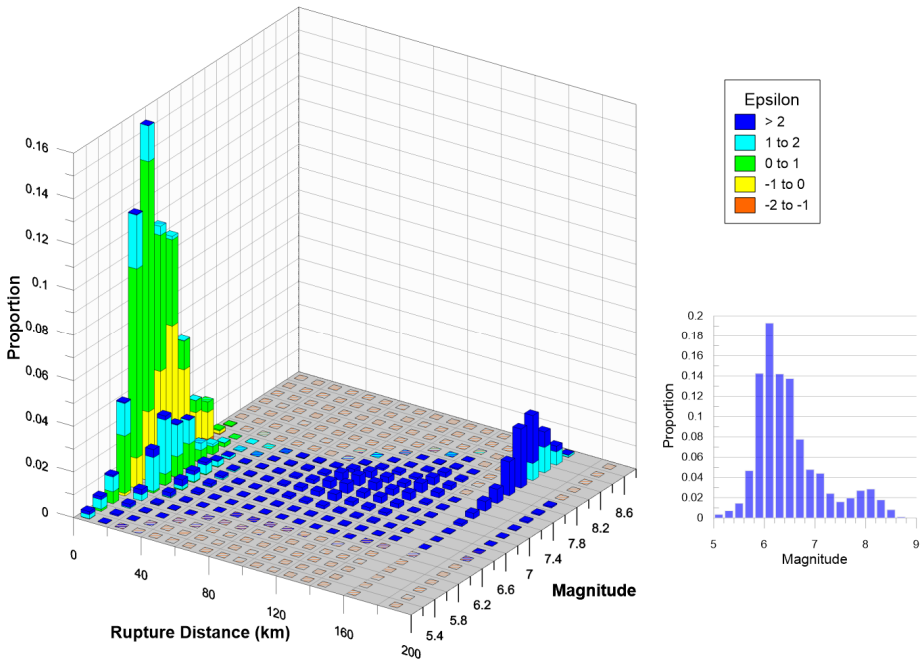

Figure 5-12. Pardee Dam Magnitude and Distance Contributions to the Mean Horizontal 1.0 Sec Spectral Acceleration Hazard at 10,000-Year Return Period

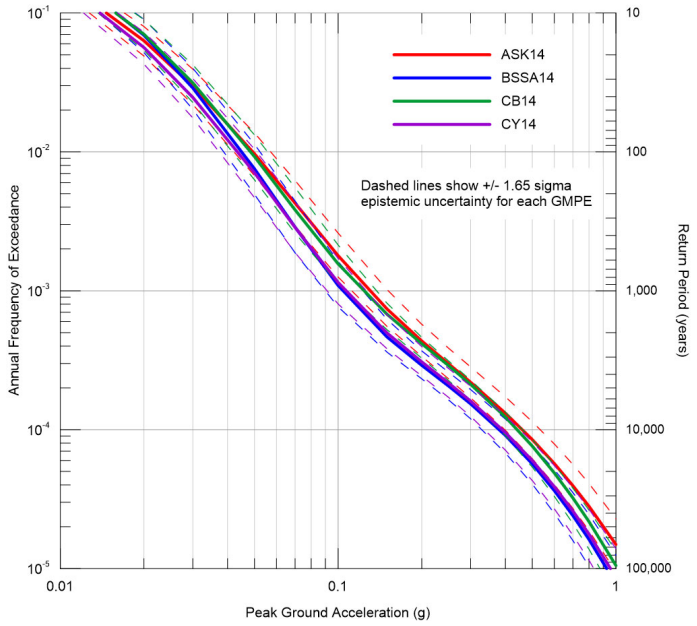

Figure 5-13. Pardee Dam Sensitivity of the Peak Ground Acceleration Hazard to the Selection of Ground Motion Models

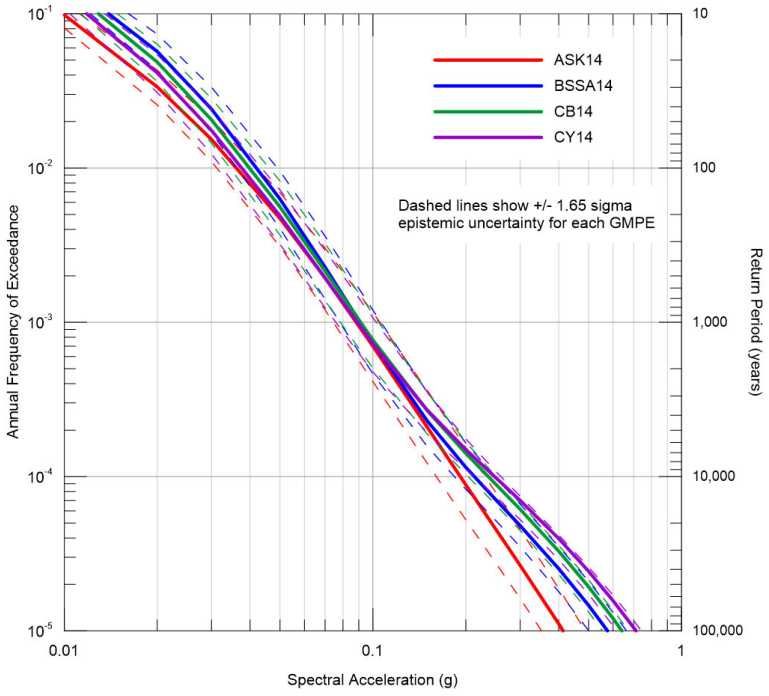

Figure 5-14. Pardee Dam Sensitivity of the 1.0 Sec Spectral Acceleration Hazard to the Selection of Ground Motion Models

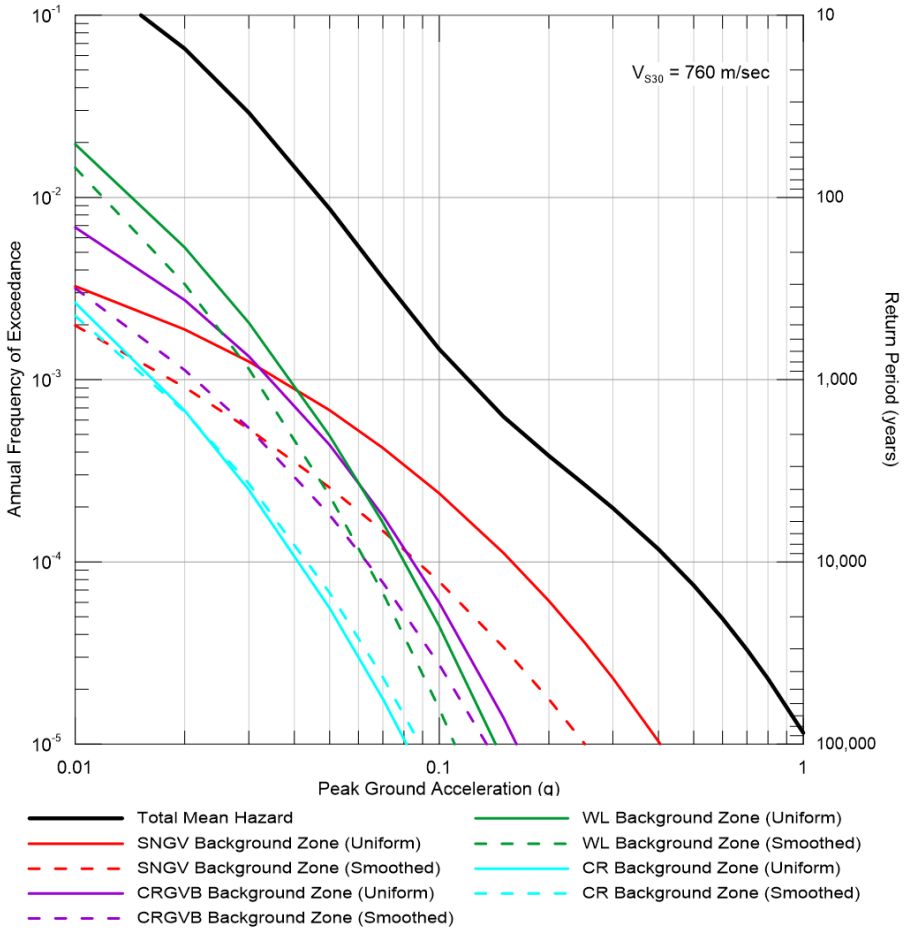

Figure 5-15. Pardee Dam Sensitivity of Horizontal Peak Ground Acceleration Hazard to Background Seismicity

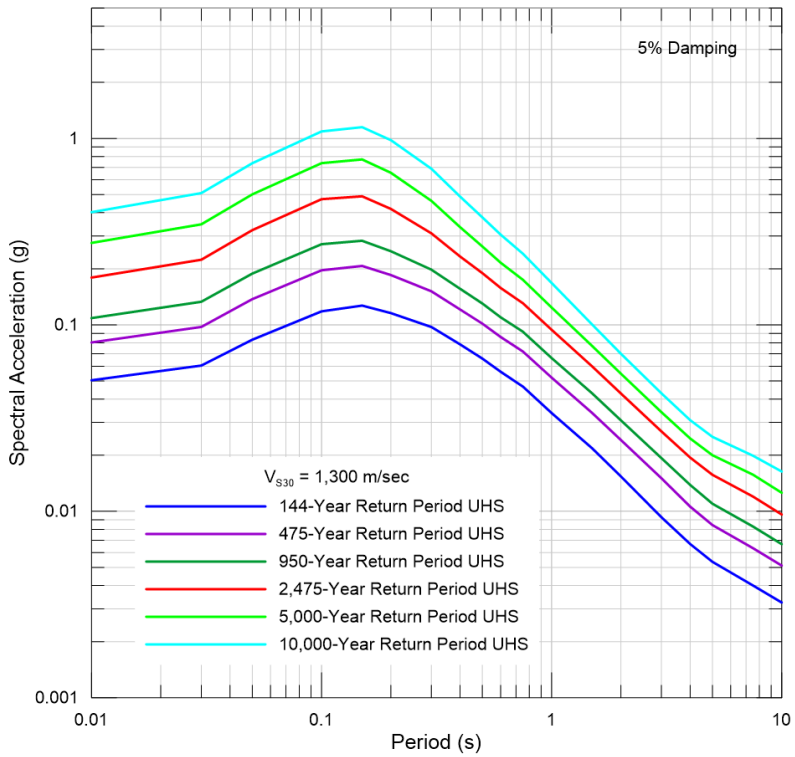

Figure 5-16. Pardee Dam 5%-Damped Uniform Hazard Response Spectra

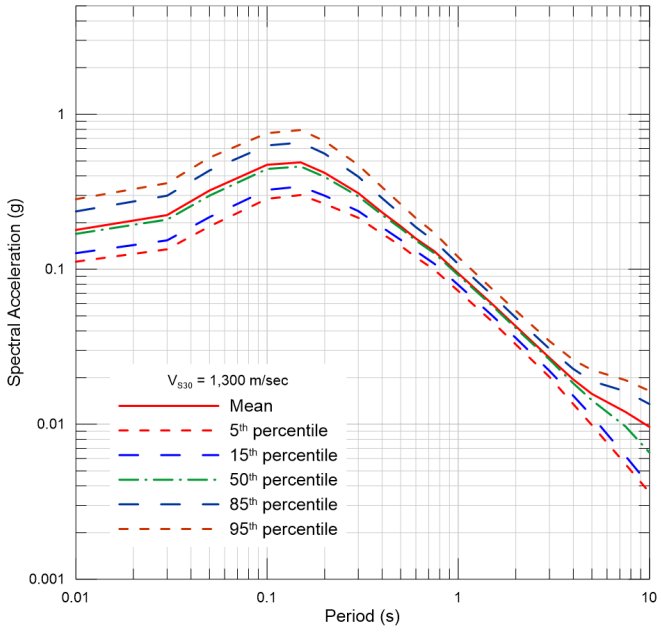

Figure 5-17. Pardee Dam 5%-Damped Mean and Fractile UHRS at a Return Period of 2,475-Years

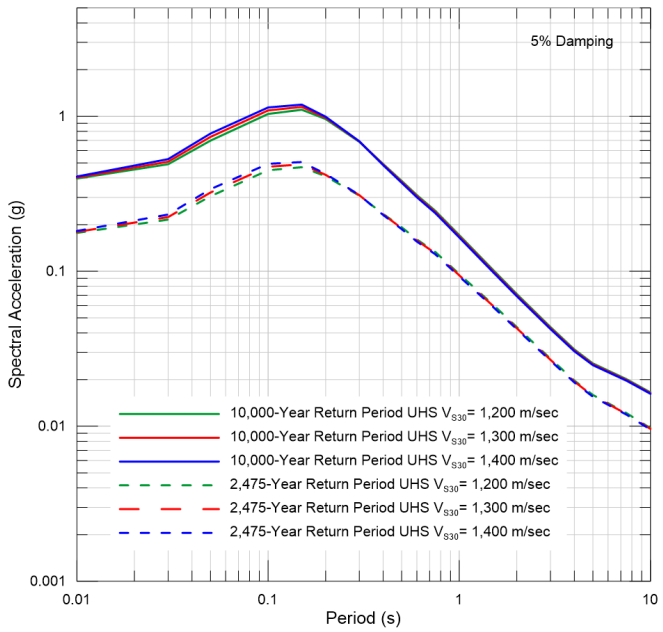

Figure 5-18. Pardee Dam Sensitivity of the 2,475- and 10,000-Year Return Period UHRS to the Selection of V_{S30}

5.1.1 Comparison with USGS National Seismic Hazard Maps

In 1996, the USGS released a “landmark” set of National Hazard Maps for earthquake ground shaking, which was a significant improvement from previous maps they had developed (Frankel et al., 1996). These maps were the result of the most comprehensive analyses of seismic sources and ground motion prediction ever undertaken on a national scale. These maps were subsequently updated by Petersen et al. (2020). The maps are the basis for the National Earthquake Hazard Reduction Program (NEHRP) risk -targeted maximum considered earthquake (MCE_R) maps, which are used in the International Building Code. The most recent maps are for a range of V_{S30} values. For a 2475-year return period and site class B/C (V_{S30} 760 m/sec), the latest 2018 National Seismic Hazard Maps indicate a PGA of 0.18 g and a 1.0 sec SA of 0.16 g for the Pardee dam site.

For a 2475-year return period, the site-specific PGA is 0.19 g with the 5th and 95th percentile values of 0.12 g and 0.30 g, respectively, for a V_{S30} of 760 m/sec. The site-specific 1.0 sec SA is 0.13 g with the 5th and 95th percentile values of 0.10 and 0.17 g, respectively. The differences are most likely due to the background seismicity. For the USGS maps in California, the background seismicity is based on a statewide seismic rate. That is, the overall rates of earthquakes allocated to the gridded source zones do not directly depend on the observed historical occurrence and rates of earthquakes in the site region, but rather are based on a state-wide rate of earthquakes and a state-wide solution of earthquake rates modeled to occur on fault sources. Whereas in this site-specific study the background seismicity rates are based on more regional seismotectonic zones.

5.2 Pardee Dam DSHA Results

Deterministic analyses were performed for the Waters Peak-Green Springs Run fault. This is the closest fault to Pardee Dam and the dam lies on the hanging wall. The Devils Gate and Ione faults are slightly farther away and with similar magnitudes would have lower ground motions, therefore were not included in the DSHA. The San Andreas and Calaveras faults are capable of large magnitude earthquakes, so they were also considered due to their potential to impact the long period ground motions.

Pardee Dam is operated by EBMUD under the jurisdiction of the California DSOD and FERC. DSOD has adopted a “consequence-hazard” matrix (Figure 5-19) that establishes guidelines for selecting the percentile level of ground motions to be used in the seismic safety evaluation of dams (DSOD, 2018).

Following this approach, 50th to 84th percentile ground motions are required for Extremely High hazard class dams such as Pardee Dam and given the low slip rate (less than 0.1 mm/yr) for the Waters Peak-Green Springs Run fault. The 84th percentile would be required for the San Andreas fault, given its very high slip rate (greater than 9 mm/yr).

FERC guidelines (FERC, 2018) allow the percentile level of ground motions to be determined from the average slip rate of the fault. For faults with slip rates greater or equal than 0.9 mm/yr the 84th percentile is to be used, for faults with slip rates less than or equal to 0.3 mm/yr the median (50th percentile) can be used. For faults with slip rates between 0.3 to 0.9 mm/yr FERC (2018) provides the following equation to determine the percentile to be used:

$$\varepsilon = \frac{Log_{10}(\frac{slip\ rate}{0.3})}{Log_{10}(3)}$$

Following FERC guidelines the 50th percentile could be used for the Waters Peak-Green Springs Run fault, while the 84th percentile would be required for the San Andreas fault.

Based on the very low slip rate for the Water Peak-Green Springs Run fault, and the criteria for both DSOD and FERC the median 5%-damped horizontal acceleration spectrum was computed. The mean characteristic magnitude of **M** 6.5 was selected based on the unsegmented rupture of the Foothills fault system with the fault geometry based on the Waters Peak-Green Springs Run fault, with a rupture (closest) distance of 0.17 km. A **M** 8.0 at a rupture distance of 155 km was used for the 84th percentile San Andreas fault, and a **M** 7.25 at a rupture distance of 112 km was used for the 84th percentile Calaveras fault in the DSHA calculations. All input parameters for the DSHA are given in Table 5-10. The same ground-motion models as used in the PSHA were used in the DSHA (see Section 4.3). Like in the PSHA the hazard was calculated for a V_{S30} of 760 m/sec and adjusted to 1,300 ± 100 m/sec using the linear site adjustment factors of Al Atik et al. (2022).

Figure 5-20 shows the DSHA spectra. The 84th percentile for the San Andreas does exceed the median for the Waters Peak-Green Springs Run fault at periods greater than 9.0 sec. Figure 5-21 shows the median horizontal acceleration response spectra from each ground-motion model and the lognormal mean of the ground-motion models for the Waters Peak-Green Springs Run fault. CB14 gives the highest ground motions for periods less than 0.1 and CY14 for longer periods.

Sensitivity to the selection of V_{S30} is shown on Figure 5-22. A V_{S30} of 1,400 m/sec gives the largest ground motions for periods less than 0.15 sec, with a V_{S30} of 1,200 m/sec giving the largest ground motions for longer periods. The difference in the spectra is around 10-percent at periods of 0.02 to 0.075 sec, but less than 5-percent at longer periods and at PGA. The recommended spectrum is the envelop of the V_{S30} and these values are provided in Table 5-11.

The median for the Waters Peak-Green Springs Run fault and the 84th percentile spectrum for the San Andreas fault are compared to the UHRS on Figure 5-23. The Waters Peak-Green Springs Run fault median spectrum is near the 10,000-year return period UHRS for periods less than 3.0 sec. The San Andreas 84th percentile spectrum is near the 144-year return period UHRS at short periods, and near the 950-year return period UHRS at a period of 10 sec.

Because Pardee Dam is at near-fault distances from the Waters Peak-Green Springs Run fault, the effect of forward rupture directivity should be considered in the ground motions. Earthquake rupture directivity is a catch-all term generally used to describe the focusing of wave energy along a fault in the direction of rupture, as well as the effects of this phenomenon. In earthquakes on shallow crustal faults, rupture directivity effects cause spatial variations in ground motion amplitude and duration around earthquakes; and differences between the strike-normal and strike-parallel components of horizontal ground motion amplitudes, which also have spatial variation around the fault (Somerville et al. 1997). These variations are generally stronger with increasing spectral period. Most ground motion models do not account for rupture directivity, so the current standard of practice is to apply rupture directivity adjustment models to response spectrum for shallow crustal earthquakes.

The DSHA spectrum for the Waters Peak-Green Springs Run fault was adjusted for fault directivity using the model of Bayless and Somerville, developed as part of the NGA-West2 Directivity Working Group (Spudich et al. 2013), which is an update to the widely used model of Somerville et al. (1997). The Bayless and Somerville (BS13) model is a function of magnitude, rupture distance, fraction of the fault

rupture that lies between the hypocenter and site, and angle between the direction of fault rupture and the direction of waves travelling from fault to the site. Figure 5-24 shows the adjustments to the spectrum for fault normal directivity effects and the values are provided in Table 5-12.

Table 5-10. Pardee Dam DSHA Inputs

NGA-West2 Parameters	Waters Peak – Green Springs Run Fault	San Andreas Fault	Calaveras Fault
M	6.5	8.0	7.25
R_{RUP} (km)	0.17	155	112
R_{JB} (km)	0.0	155	112
R_X (km)	0.19	155	112
F_{RV}	0	0	0
F_N	1*	0	0
F_{HW}	1	0	0
Z_{TOR} (km)	0	0	0
Dip	65	90	90
V_{S30} (m/sec)	1,300 ± 100	1,300 ± 100	1,300 ± 100
$Z_{1.0}$ (km)	0.001	0.001	0.001
$Z_{2.5}$ (km)	0.328	0.328	0.328
W (km)	16.6	13	15

R_{RUP} = Closest distance to coseismic rupture
R_{JB} = Closest distance to surface projection of coseismic rupture
R_X = Horizontal distance from top of rupture measured perpendicular to fault strike
F_{RV} = Reverse fault flag (1 = reverse fault)
F_N = Normal fault flag (1 = normal fault)
* (Normal faulting weighted 0.5, strike-slip faulting weighted 0.5)
F_{HW} = Hanging Wall flag (1 = in hanging wall, 0 = in foot wall)
Z_{TOR} = Depth to top of coseismic rupture
Dip = Average dip of rupture plane (degrees)
V_{S30} = The time average shear-wave velocity over a subsurface depth of 30 m
$Z_{1.0}$ = Depth to Vs=1.0 km/sec
$Z_{2.5}$ = Depth to Vs=2.5 km/sec
W = fault width

Table 5-11. Pardee Dam DSHA Spectra (Enveloped Hard Rock)

	Waters Peak – Green Springs Run Fault - Median	San Andreas Fault – 84th Percentile	Calaveras Fault – 84th Percentile
Period (sec)	**SA (g)**	**SA (g)**	**SA (g)**
0.01 (PGA)	0.496	0.0603	0.0548
0.020	0.569	0.0668	0.0552
0.030	0.716	0.0791	0.0597
0.050	0.923	0.0923	0.0722
0.075	1.12	0.102	0.0871
0.100	1.12	0.0984	0.0963
0.150	1.12	0.0966	0.1049
0.200	0.973	0.0924	0.1063
0.250	0.825	0.0905	0.1039
0.300	0.703	0.0887	0.1002
0.400	0.551	0.0837	0.0905
0.500	0.440	0.0771	0.0808
0.750	0.297	0.0613	0.0606
1.000	0.208	0.0466	0.0450
1.500	0.120	0.0337	0.0301
2.000	0.0801	0.0257	0.0219
3.000	0.0457	0.0185	0.0141
4.000	0.0301	0.0152	0.0101
5.000	0.0214	0.0125	0.00772
7.500	0.00986	0.00905	0.00478
10.000	0.00624	0.00654	0.00315

Table 5-12. Pardee Dam DSHA Fault Normal Spectra

	Waters Peak – Green Springs Run Fault - Median
Period (sec)	**SA (g)**
0.01 (PGA)	0.496
0.020	0.569
0.030	0.716
0.050	0.923
0.075	1.116
0.100	1.119
0.150	1.121
0.200	0.973
0.250	0.825
0.300	0.703
0.400	0.551
0.500	0.440
0.750	0.297
1.000	0.208
1.500	0.120
2.000	0.0929
3.000	0.0607
4.000	0.0400
5.000	0.0291
7.500	0.0135
10.000	0.00864

HAZARD CLASS	SLIP RATE: Very High (9 mm/yr or greater)	High (8.9 to 1.1 mm/yr)	Moderate (1.0 to 0.1 mm/yr)	Low (Less than 0.1 mm/yr)
Extremely High	84th	84th	67th to 84th	50th to 84th
High	84th	84th	50th to 84th	50th to 84th
Significant	67th to 84th	50th to 84th	50th to 67th	50th
Low	50th	50th	50th	50th

DSOD Hazard Matrix
September 2017

Figure 5-19. DSOD Hazard Matrix

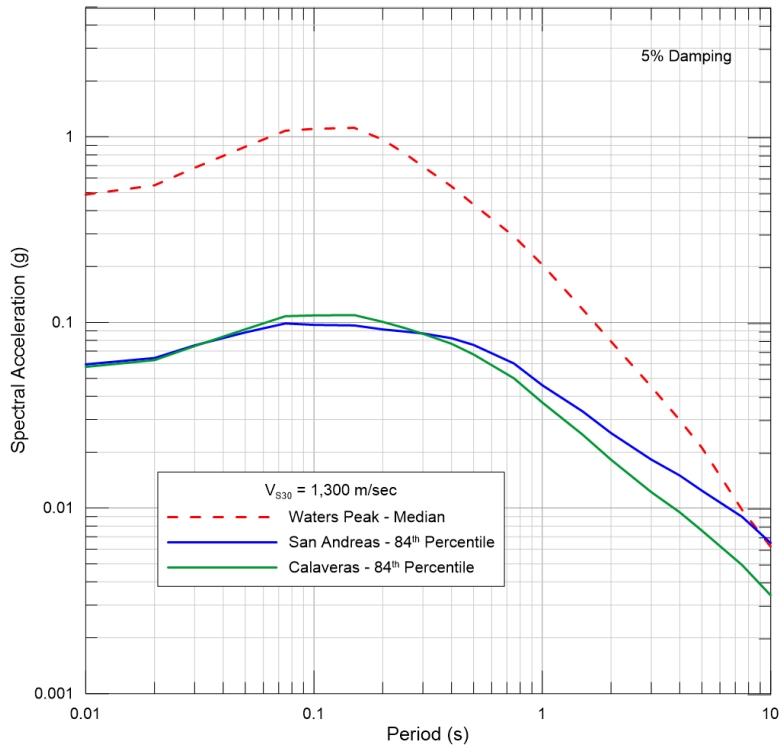

Figure 5-20. Pardee Dam DSHA Spectra Summary

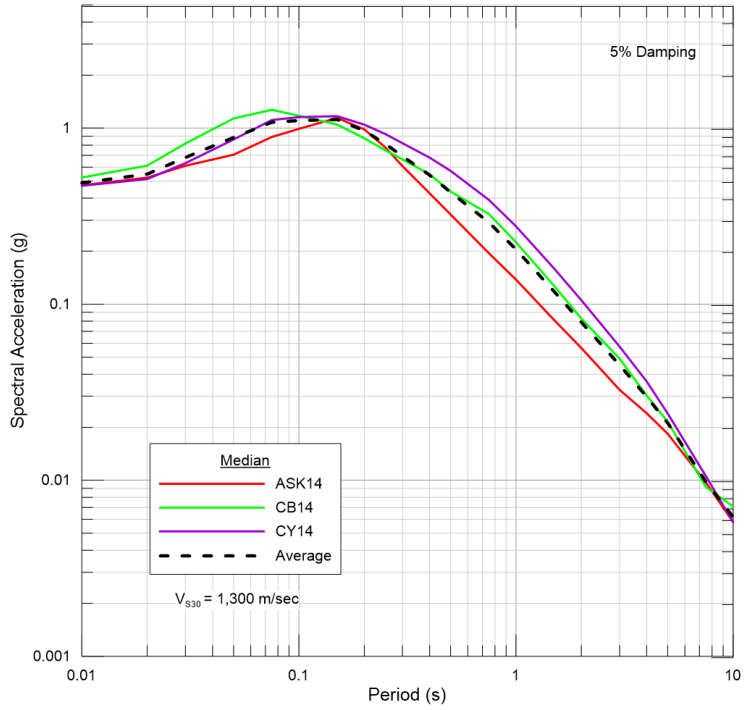

Figure 5-21. Pardee Dam Sensitivity to the Selection of Ground Motion Models for the 5%-Damped Median Waters Peak-Green Springs Run Fault DSHA Spectra

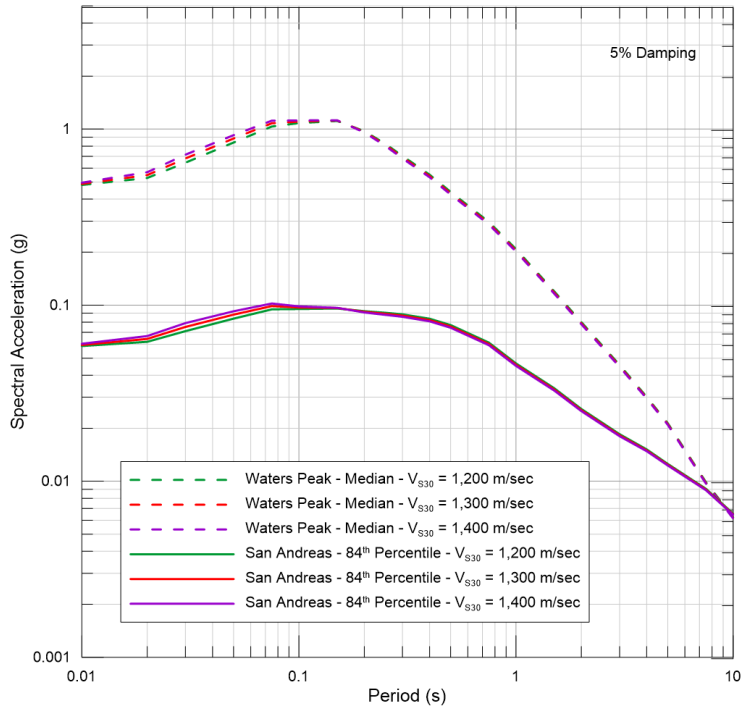

Figure 5-22. Pardee Dam Sensitivity to the Selection of V_{S30} for the DSHA Spectra

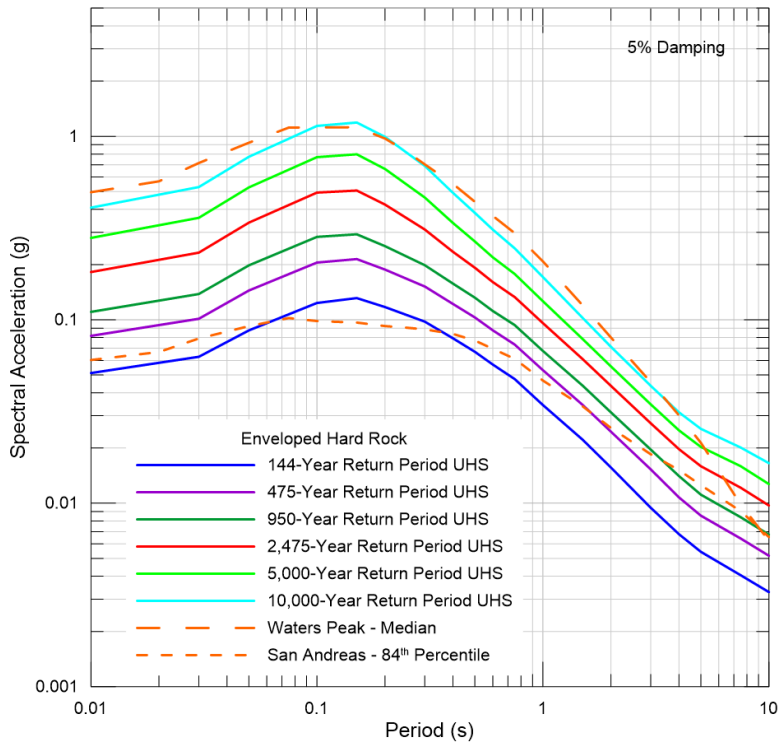

Figure 5-23. Pardee Dam Comparison of 5%-Damped Uniform Hazard Response Spectra and Deterministic Spectra

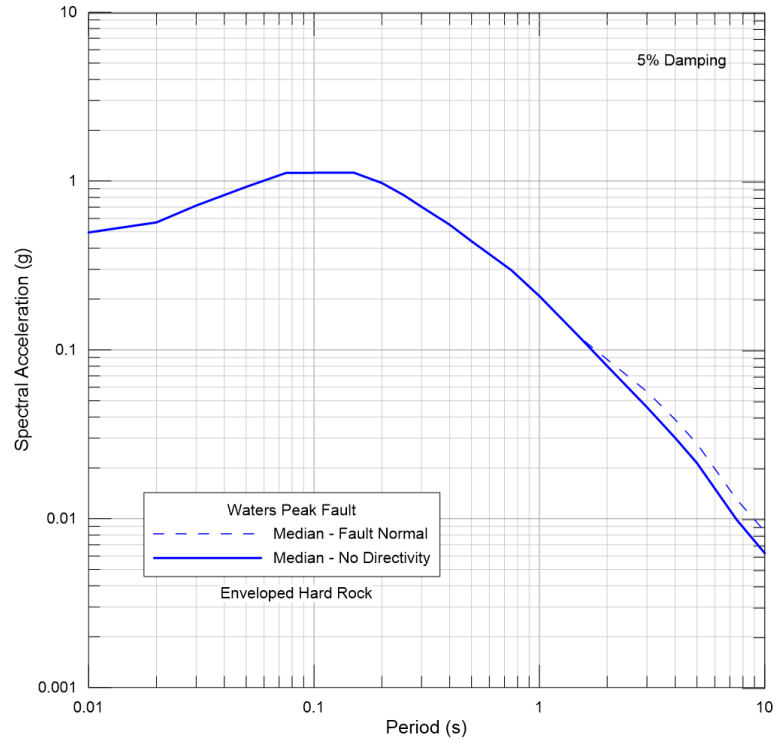

Figure 5-24. Pardee Dam DSHA Spectra Adjusted for Fault Normal Directivity

5.3 Camanche Dam PSHA Results

The PSHA at Camanche Dam was calculated for a site condition with a V_{S30} of 760 ± 100 m/sec (Section 4.2.2). The V_{S30} range is to account for the epistemic uncertainty in the adopted value in addition to the spatial variability in V_{S30} at the dam site. The figures shown and deaggregations are for a V_{S30} of 660 m/sec; however, these deaggregations would be similar for the other V_{S30} values.

The results of the PSHA are presented in terms of ground motion as a function of annual exceedance frequency. This frequency is the reciprocal of the average return period. Figures 5-25 and 5-26 show the mean, median (50th percentile), 5th, 15th, 85th, and 95th percentile hazard curves for the PGA and 1.0 sec spectral accelerations (SA). The fractiles indicate the range of uncertainties about the mean hazard. At a return period of 10,000 years, there is a factor of 1.9 difference between the 5th and 95th percentile hazard at PGA (Figure 5-25) and a factor of 1.8 at 1.0 sec SA (Figure 5-26). The PGA and 1.0 sec SA for select return periods and fractiles are listed in Table 5-13.

The contributions of the various seismic sources to mean PGA and 1.0 sec SA hazard are shown on Figures 5-27 and 5-29. The fractional contribution of seismic sources as a percent of the total mean hazard is presented on Figures 5-28 and 5-30. At PGA and return period less than about 1,000-years, the more distant, highly active faults, such as the San Andreas, Calaveras and Hayward, contribute the most to the total mean hazard. The SNGV background zone is the most significant source at longer return periods. The faults of the Foothills fault system are a significant contributor to the total mean hazard at longer return periods (i.e. 10,000-years). Figure 5-28 shown the fractional contributions of significant sources as well as the combined hazard for the Foothills fault system faults, for all other faults, and for all background sources. At a return period of 10,000-years, the Foothills fault system and background sources contribute equally, about 40-percent each (Figure 5-28). At 1.0 sec SA, the San Andreas fault is the most significant contributor to the total mean hazard over most return periods, with the Calaveras and Hayward faults also significant contributors (Figures 5-29 and 5-30). Like at PGA, the Foothills fault system contributes to the total mean hazard at long return periods.

Figures 5-31 to 5-36 illustrate the proportional contributions after deaggregating the mean PGA and 1.0 sec SA hazard by magnitude, distance and epsilon bins for 950-, 2,475- and 10,000-year return periods. Epsilon is the difference between the logarithm of the ground motion amplitude and the mean logarithm of ground motion (for that M and R) measured in units of the standard deviation (σ) of the logarithm of the median ground motion. Therefore, an epsilon greater than zero represents an above-average ground motion. Also included in Figures 5-31 to 5-36 is a plot with the magnitude deaggregation for all distances combined. The hazard at PGA and a return period of 950-years is trimodal, with contributions from the background seismicity at distances less than 40 km and magnitudes less than **M** 7.0, faults such as the Calaveras and Hayward at 50 to 110 km and magnitudes **M** 6.0 to 7.6, and the San Andreas fault at 145 km and magnitudes 7.8 to 8.6 (Figure 5-31). At longer return periods the seismic sources at distances less than 30 km and magnitudes **M** 5.0 to 7.0, such as the background seismicity and Foothills fault system contribute the most to the hazard, though the more distant sources are apparent (Figures 5-32 and 5-33). At 1.0 sec SA the hazard is trimodal for all return periods, though with the San Andreas fault being the most apparent source, at 145 km and **M** 7.5 to 8.8 (Figure 5-35). Based on the magnitude and distance bins (e.g., Figures 5-31 to 5-36), the controlling earthquakes as defined by the modal magnitude **M***, distance D*, and epsilon ε* can be calculated. Table 5-14 lists the **M***, D*, and ε* for PGA and 1.0 sec SA at the return periods of interest. Table 5-15 lists the **M*** and D* when the epsilons are combined for each magnitude-distance bin. Table 5-16 lists the mean $\bar{M}$, $\bar{D}$, $\bar{\varepsilon}$ values. Also provided are the mean $\bar{M}$ and $\bar{D}$ for the significant contributing sources (Table 5-17).

The sensitivities of the PGA and 1.0 sec SA hazard to selection of ground-motion models are shown on Figures 5-37 and 5-38. Each hazard curve shown is calculated using only that model. The ground motion models are general similar, though the ASK14 and CB14 model gives slightly higher ground motions at PGA, while the ASK14 model give the highest ground motions at 1.0 sec SA.

Sensitivity of the unform and gridded background seismicity for the seismic sources zones at PGA is shown on Figure 5-39. Given the relatively low seismicity in the region, the uniform seismicity for the SNGV contributes the most to the total mean hazard over most return periods of interest, though the CRGVB and WL uniform zones contribute at shorter return periods. For the SNGV, WL and CRGVB seismic zones the uniform seismicity contributes more to the total mean hazard, than the smoothed

seismicity, again, due to the relatively low seismicity in the region. For the CR seismic zone, the uniform and smoothed seismicity contribute similarly to the total mean hazard, as a result of the relatively high rate of seismicity.

The UHRS for a range of return periods from 144- to 10,000-years and a V_{S30} of 660 m/sec are shown on Figure 5-40 and the values given in Table 5-18. These UHRS reflect the geometric mean of expected horizontal ground motions as predicted by the ground-motion models. Figure 5-41 shows the range in epistemic uncertainty in the 2,475-year return period UHRS. The return period of PGA at the 95th percentile level computed from the mean hazard curve is 5,800-years and at 1.0 sec SA value the return period is 5,050-years. The 5th and 95th percentile UHRS differ by an average factor of 2.1. These ranges represent the uncertainty modeled in the PSHA based on our current knowledge of all inputs. Additional information on seismic sources or future refinement of ground-motion models would likely decrease the range of uncertainty, but the mean may shift within this range.

The sensitivity of the UHRS to the selection of V_{S30} is shown on Figure 5-42. A V_{S30} of 660 m/sec gives the largest ground motions for all periods and is the recommend UHRS at Camanche. The difference in the UHRS is around 10-percent at PGA between a V_{S30} of 660 m/sec and 860 m/sec, but near 20-percent for periods greater than 0.3 sec. All UHRS values are provided in Tables 5-18 to 5-20.

Because Camanche Dam is at near-fault distances from the Foothills fault system, the effect of forward rupture directivity was explored. Fault directivity is discussed in more detail in Section 5.4. The PSHA was run with fault directivity for the Foothills fault system using the model of Bayless and Somerville, developed as part of the NGA-West2 Directivity Working Group (Spudich et al. 2013), which is an update to the widely used model of Somerville et al. (1997). In the PSHA, directivity had minimal effect at Camanche dam, less than 1 percent at a period of 10 sec, and is therefore not included in the in the tables or figures below. This is due in large part to the randomization of the hypocenter in the PSHA code and that dip-slip faults generally have lower directivity effects than strike-slip faults.

Table 5-13. Camanche Dam Summary of Horizontal Probabilistic Ground Motions (V_{S30} = 660 m/sec)

Return Period (years)	PGA (g) Mean [5th, 95th percentile]	1.0 Sec SA (g) Mean [5th, 95th percentile]
144	0.0658 [0.0538, 0.0784]	0.0631 [0.0499 0.0782]
475	0.101 [0.0812, 0.122]	0.0977 [0.0751, 0.124]
950	0.128 [0.102, 0.157]	0.122 [0.0933, 0.159]
2,475	0.178 [0.137, 0.227]	0.166 [0.123, 0.216]
5,000	0.228 [0.169, 0.298]	0.205 [0.150, 0.267]
10,000	0.290 [0.208, 0.387]	0.249 [0.181, 0.327]

Table 5-14. Camanche Dam Modal Magnitude, Distance and Epsilon

Period (sec)	Return Period:	144-year	475-year	950-year	2,475-year	5,000-year	10,000-year
PGA	M*	6.9	7.9	6.1	5.9	6.1	6.1
	D* (km)	95.0	145.0	15.0	15.0	15.0	15.0
	ε*	1.5	1.5	-0.5	0.5	0.5	0.5
1.0 sec SA	M*	6.9	7.7	7.9	7.9	8.1	8.1
	D* (km)	95.0	145.0	145.0	145.0	145.0	145.0
	ε*	1.5	1.5	1.5	1.5	1.5	> 2.0

Table 5-15. Camanche Dam Modal Magnitude and Distance (combined epsilon)

Period (sec)	Return Period:	144-year	475-year	950-year	2,475-year	5,000-year	10,000-year
PGA	M*	6.9	7.9	6.1	6.1	6.1	6.1
	D* (km)	95.0	145.0	15.0	15.0	15.0	15.0
1.0 sec SA	M*	7.9	7.9	7.9	7.9	7.9	8.1
	D* (km)	145.0	145.0	145.0	145.0	145.0	145.0

Table 5-16. Camanche Dam Mean Magnitude, Distance and Epsilon

Period (Sec)	Return Period:	144-year	475-year	950-year	2,475-year	5,000-year	10,000-year
PGA	$\bar{M}$	6.6	6.6	6.5	6.3	6.2	6.1
	$\bar{D}$ (km)	88.1	73.8	62.5	47.3	36.7	28.5
	$\bar{\varepsilon}$	1.0	1.2	1.2	1.2	1.2	1.3
1.0 sec SA	$\bar{M}$	6.9	7.0	7.1	7.1	7.1	7.1
	$\bar{D}$ (km)	112.2	106.3	102.9	97.8	93.3	88.1
	$\bar{\varepsilon}$	1.3	1.7	1.8	2.0	2.0	2.1

Table 5-17. Camanche Dam Mean Magnitude and Distance for Significant Seismic Sources

Period (sec)	Source	Return Period:	144-year	475-year	950-year	2,475-year	5,000-year	10,000-year
PGA	Waters Peak-Green Springs Run	M*	5.9	6.0	6.1	6.1	6.2	6.3
		D* (km)	28.1	26.0	24.6	23.0	20.7	19.6
	Ione	M*	5.9	5.9	5.9	6.0	6.0	6.1
		D* (km)	13.5	13.4	13.3	13.1	12.7	12.4
	SNGV	M*	5.6	5.6	5.6	5.6	5.7	5.7
		D* (km)	55.4	42.9	36.6	31.3	24.5	20.9
	San Andreas (Unseg)	M*	7.8	7.9	8.0	8.0	8.1	8.2
		D* (km)	143.2	142.0	141.6	141.3	141.0	140.9
1.0 sec SA	Waters Peak-Green Springs Run	M*	6.0	6.2	6.2	6.2	6.3	6.4
		D* (km)	27.5	24.3	24.3	23.0	21.8	20.6
	Ione	M*	5.9	6.0	6.0	6.1	6.1	6.2
		D* (km)	13.3	13.0	13.0	12.8	12.7	12.4
	SNGV	M*	5.9	5.9	5.9	6.0	6.0	6.1
		D* (km)	69.3	43.8	43.6	35.9	29.3	23.9
	San Andreas (Unseg)	M*	7.6	7.9	7.9	7.9	8.0	8.0
		D* (km)	149.3	143.9	143.9	142.9	142.3	141.8

Table 5-18. Camanche Dam 5%-Damped Mean Horizontal UHRS (V_{S30} = 660 m/sec)

Return Period:	144-year	475-year	950-year	2,475-year	5,000-year	10,000-year
Period (sec)	**SA (g)**	**SA (g)**	**SA (g)**	**SA (g)**	**SA (g)**	**SA (g)**
0.010 (PGA)	0.0658	0.101	0.128	0.178	0.228	0.290
0.030	0.0726	0.113	0.144	0.202	0.259	0.332
0.050	0.0901	0.142	0.184	0.261	0.339	0.438
0.100	0.129	0.206	0.267	0.382	0.499	0.645
0.150	0.146	0.230	0.295	0.419	0.544	0.704
0.200	0.148	0.230	0.293	0.412	0.530	0.683
0.300	0.138	0.212	0.267	0.365	0.460	0.578
0.400	0.124	0.190	0.238	0.322	0.400	0.496
0.500	0.112	0.171	0.215	0.29	0.359	0.441
0.600	0.0993	0.152	0.190	0.255	0.315	0.386
0.750	0.0846	0.130	0.163	0.220	0.271	0.331
1.000	0.0631	0.0977	0.122	0.166	0.205	0.249
1.500	0.0412	0.0646	0.0815	0.110	0.136	0.166
2.000	0.0298	0.0468	0.0595	0.0810	0.100	0.122
3.000	0.0182	0.0293	0.0373	0.0515	0.0638	0.0782
4.000	0.0126	0.0208	0.0267	0.0369	0.0464	0.0572
5.000	0.00959	0.0157	0.0207	0.0292	0.0366	0.0456
7.500	0.00643	0.0106	0.0141	0.0209	0.0270	0.0342
10.000	0.00482	0.00794	0.0106	0.0158	0.0210	0.0270

Table 5-19. Camanche Dam 5%-Damped Mean Horizontal UHRS (V_{S30} = 760 m/sec)

Return Period:	144-year	475-year	950-year	2,475-year	5,000-year	10,000-year
Period (sec)	**SA (g)**	**SA (g)**	**SA (g)**	**SA (g)**	**SA (g)**	**SA (g)**
0.010 (PGA)	0.0617	0.095	0.121	0.168	0.215	0.274
0.030	0.0691	0.107	0.137	0.193	0.249	0.320
0.050	0.0868	0.138	0.178	0.253	0.330	0.428
0.100	0.122	0.196	0.255	0.366	0.480	0.624
0.150	0.135	0.214	0.275	0.392	0.511	0.664
0.200	0.134	0.209	0.267	0.377	0.486	0.626
0.300	0.123	0.188	0.237	0.325	0.410	0.515
0.400	0.110	0.167	0.210	0.284	0.353	0.437
0.500	0.0984	0.150	0.188	0.254	0.314	0.386
0.600	0.0862	0.132	0.166	0.223	0.276	0.338
0.750	0.0738	0.113	0.142	0.192	0.236	0.289
1.000	0.0547	0.0844	0.106	0.144	0.177	0.217
1.500	0.0355	0.0557	0.0706	0.0953	0.117	0.143
2.000	0.0256	0.0403	0.0516	0.0704	0.0869	0.106
3.000	0.0156	0.0253	0.0324	0.0444	0.0554	0.068
4.000	0.0110	0.0179	0.0232	0.0323	0.0402	0.050
5.000	0.00853	0.0137	0.018	0.0254	0.0322	0.0398
7.500	0.00585	0.00949	0.0126	0.0185	0.0240	0.0306
10.000	0.00448	0.00727	0.00962	0.0142	0.0189	0.0242

Table 5-20. Camanche Dam 5%-Damped Mean Horizontal UHRS (V_{S30} = 860 m/sec)

Return Period:	144-year	475-year	950-year	2,475-year	5,000-year	10,000-year
Period (sec)	**SA (g)**	**SA (g)**	**SA (g)**	**SA (g)**	**SA (g)**	**SA (g)**
0.010 (PGA)	0.0583	0.0899	0.114	0.159	0.204	0.260
0.030	0.0659	0.103	0.132	0.186	0.239	0.308
0.050	0.0838	0.133	0.173	0.247	0.322	0.419
0.100	0.117	0.187	0.244	0.352	0.462	0.602
0.150	0.126	0.200	0.258	0.368	0.480	0.625
0.200	0.123	0.192	0.246	0.346	0.447	0.576
0.300	0.111	0.170	0.214	0.293	0.370	0.465
0.400	0.0984	0.150	0.188	0.254	0.316	0.392
0.500	0.0871	0.133	0.167	0.226	0.280	0.344
0.600	0.0765	0.117	0.147	0.198	0.245	0.300
0.750	0.0653	0.101	0.126	0.170	0.210	0.256
1.000	0.0482	0.0746	0.094	0.127	0.157	0.192
1.500	0.0314	0.0491	0.0618	0.0837	0.103	0.126
2.000	0.0225	0.0355	0.0453	0.0620	0.0768	0.094
3.000	0.0140	0.0229	0.0295	0.0404	0.0508	0.0623
4.000	0.0101	0.0163	0.0213	0.0298	0.0371	0.0460
5.000	0.00803	0.0128	0.0169	0.0239	0.0304	0.0376
7.500	0.00564	0.00913	0.0121	0.0178	0.0231	0.0295
10.000	0.00436	0.00705	0.00931	0.0137	0.0182	0.0234

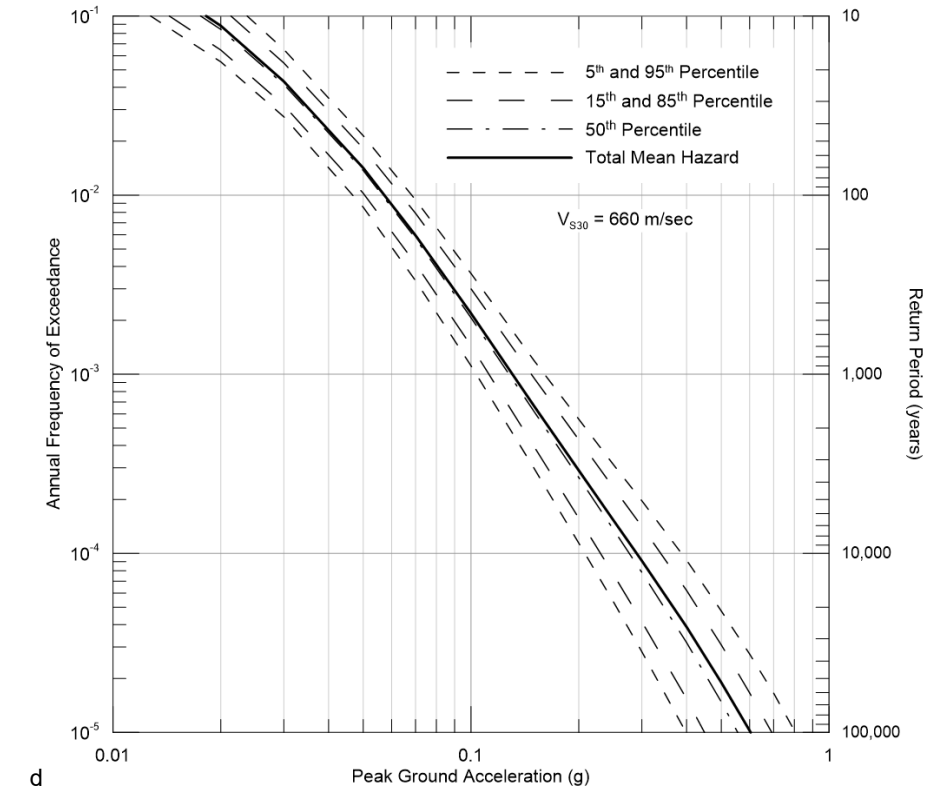

Figure 5-25. Camanche Dam Seismic Hazard Curves for Peak Ground Acceleration

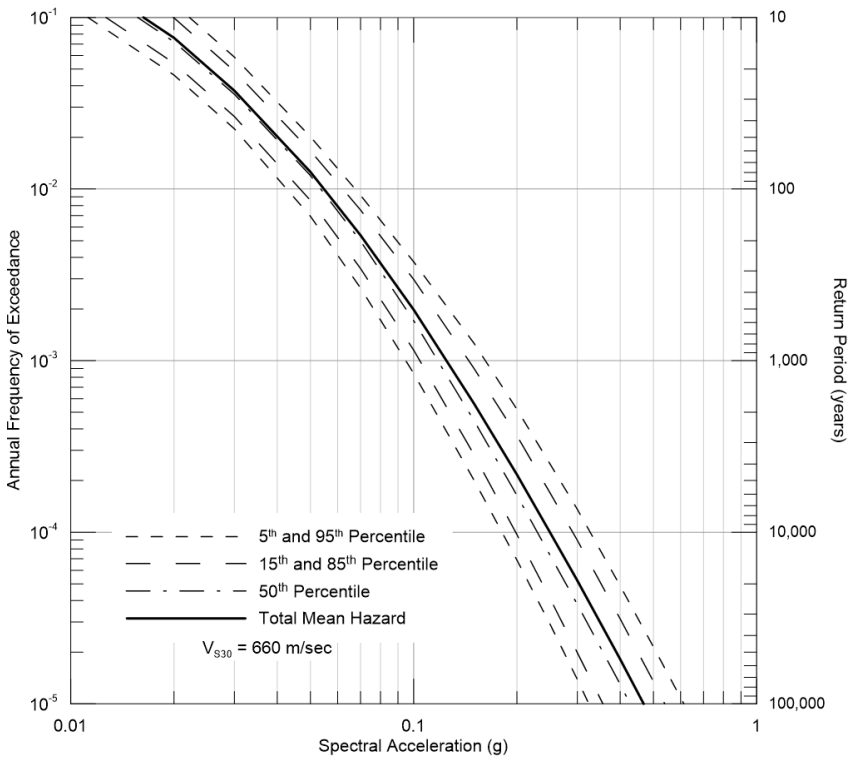

Figure 5-26. Camanche Dam Seismic Hazard Curves for 1.0 Sec Spectral Acceleration

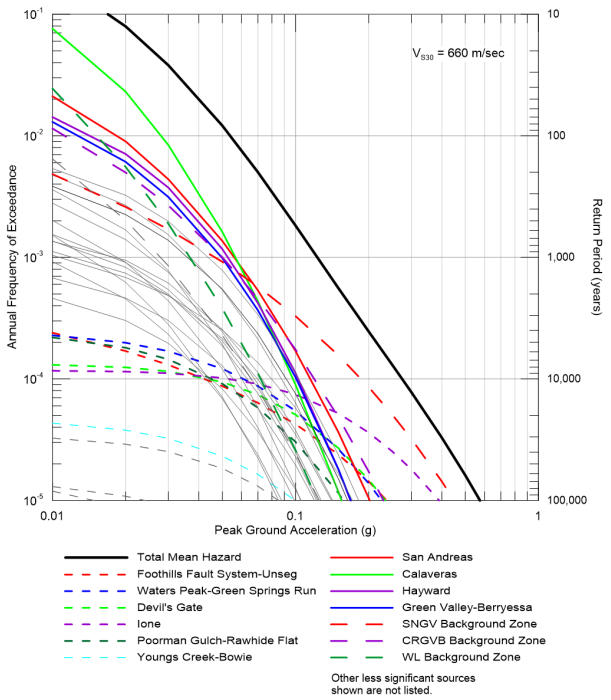

Figure 5-27. Camanche Dam Seismic Source Contributions to Mean Horizontal Peak Ground Acceleration Hazard

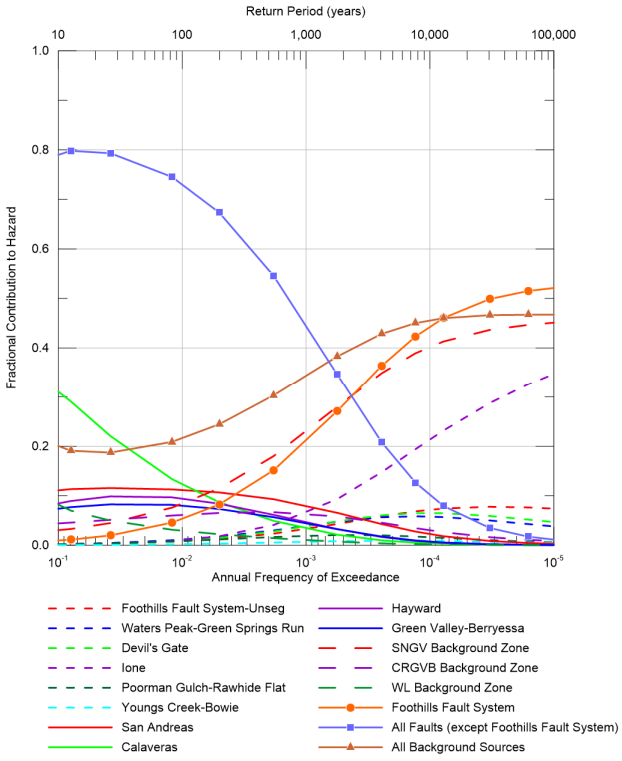

Figure 5-28. Camanche Dam Seismic Source Fractional Contributions to Mean Horizontal Peak Ground Acceleration Hazard

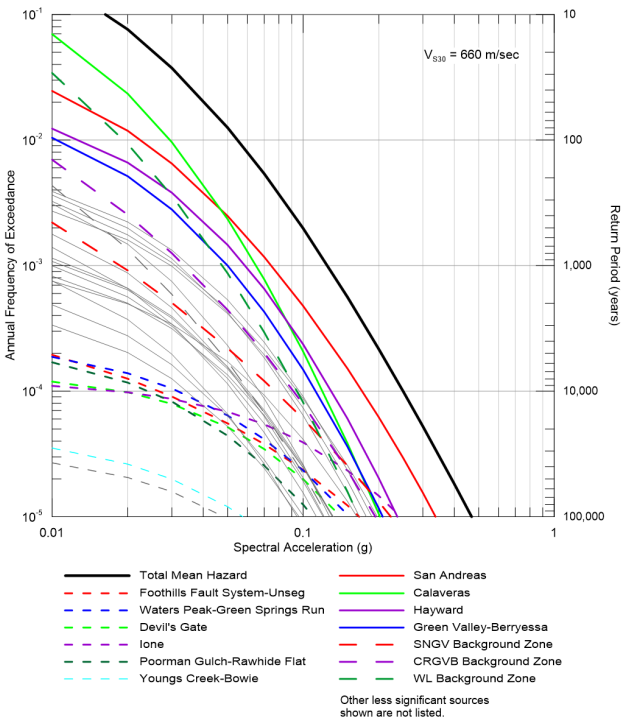

Figure 5-29. Camanche Dam Seismic Source Contributions to Mean Horizontal 1.0 Sec Spectral Acceleration Hazard

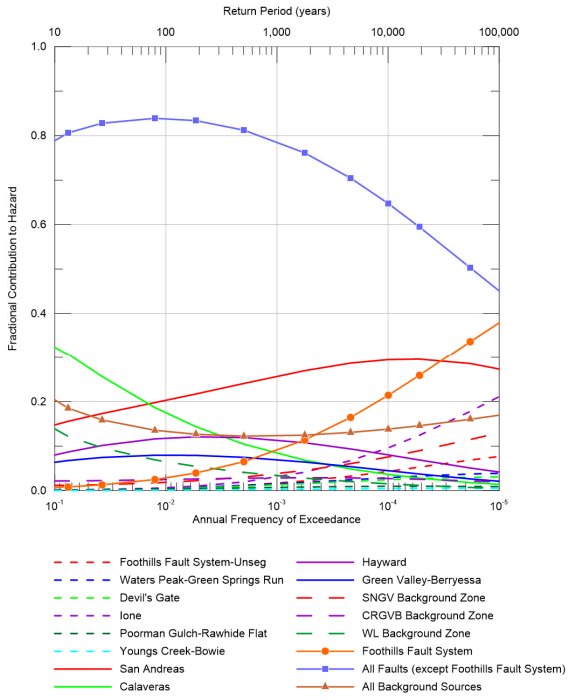

Figure 5-30. Camanche Dam Seismic Source Fractional Contributions to Mean Horizontal 1.0 Sec Spectral Acceleration Hazard

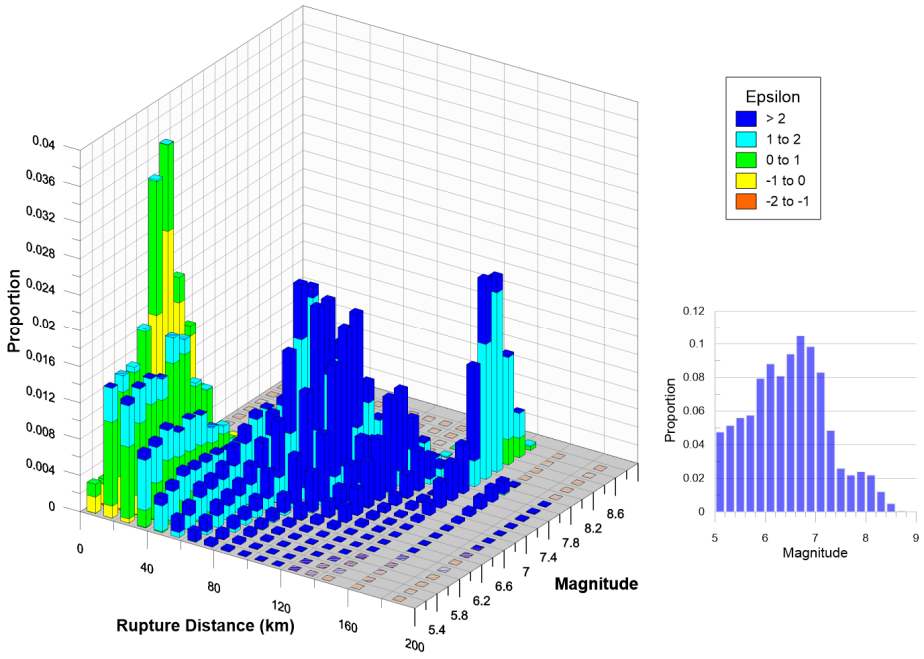

Figure 5-31. Camanche Dam Magnitude and Distance Contributions to the Mean Horizontal Peak Ground Acceleration Hazard at 950-Year Return Period

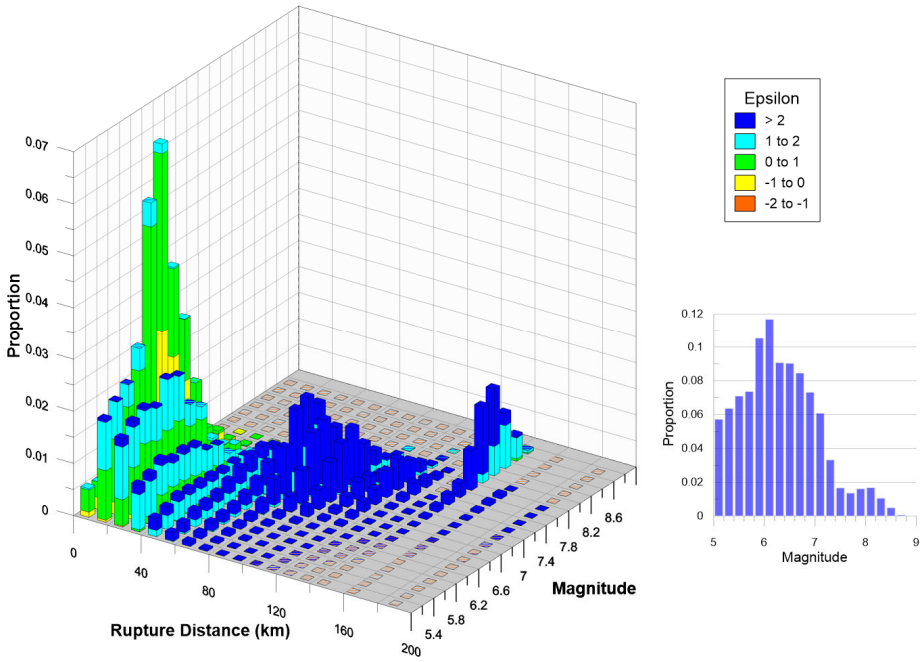

Figure 5-32. Camanche Dam Magnitude and Distance Contributions to the Mean Horizontal Peak Ground Acceleration Hazard at 2,475-Year Return Period

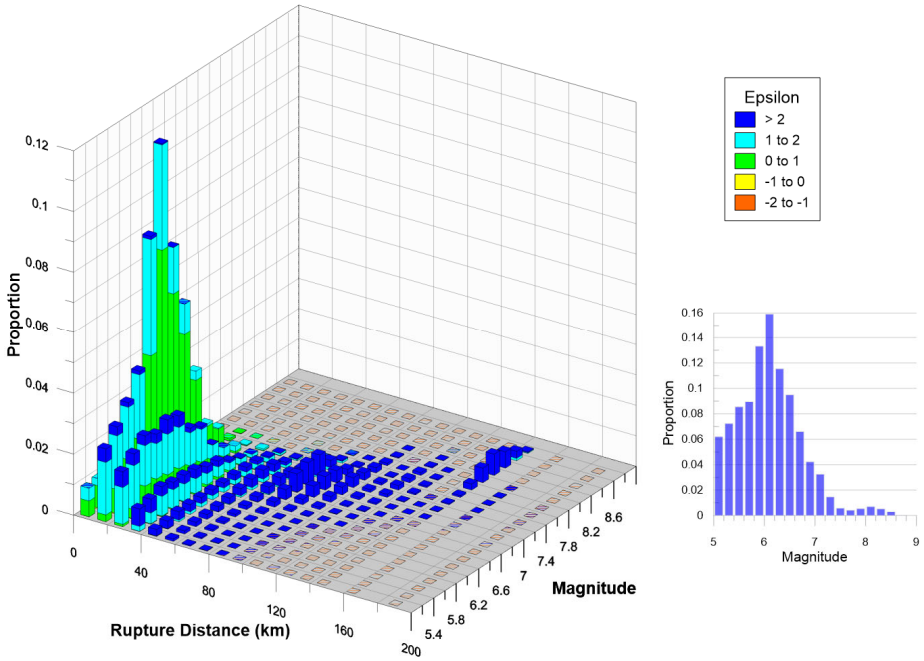

Figure 5-33. Camanche Dam Magnitude and Distance Contributions to the Mean Horizontal Peak Ground Acceleration Hazard at 10,000-Year Return Period

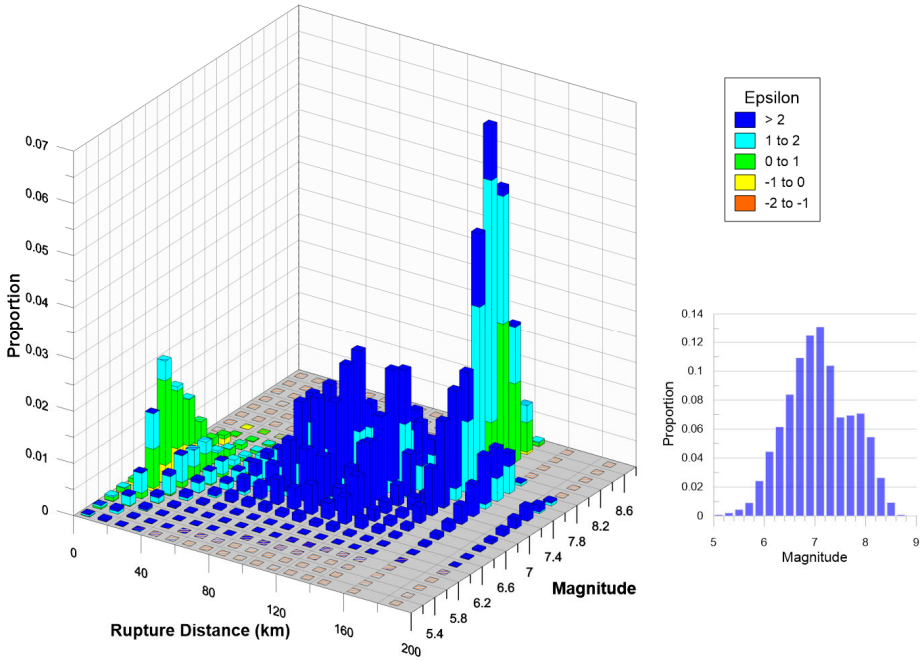

Figure 5-34. Camanche Dam Magnitude and Distance Contributions to the Mean Horizontal 1.0 Sec Spectral Acceleration Hazard at 950-Year Return Period

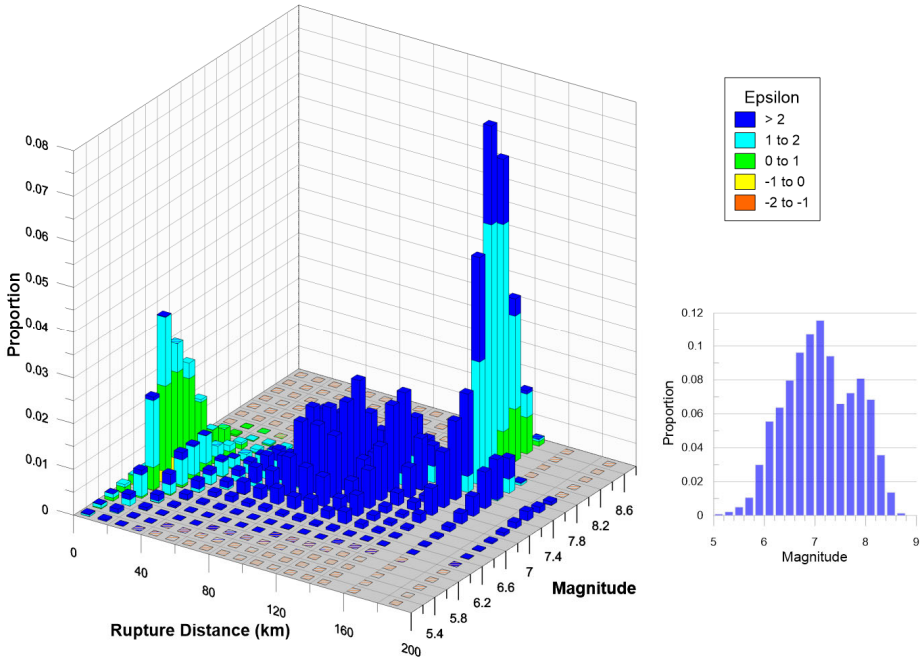

Figure 5-35. Camanche Dam Magnitude and Distance Contributions to the Mean Horizontal 1.0 Sec Spectral Acceleration Hazard at 2,475-Year Return Period

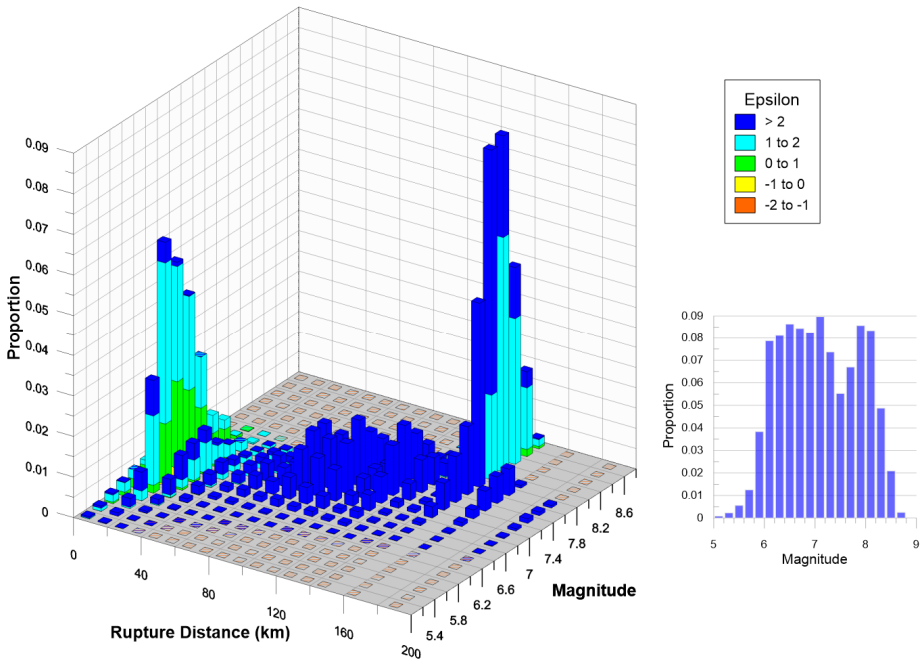

Figure 5-36. Camanche Dam Magnitude and Distance Contributions to the Mean Horizontal 1.0 Sec Spectral Acceleration Hazard at 10,000-Year Return Period

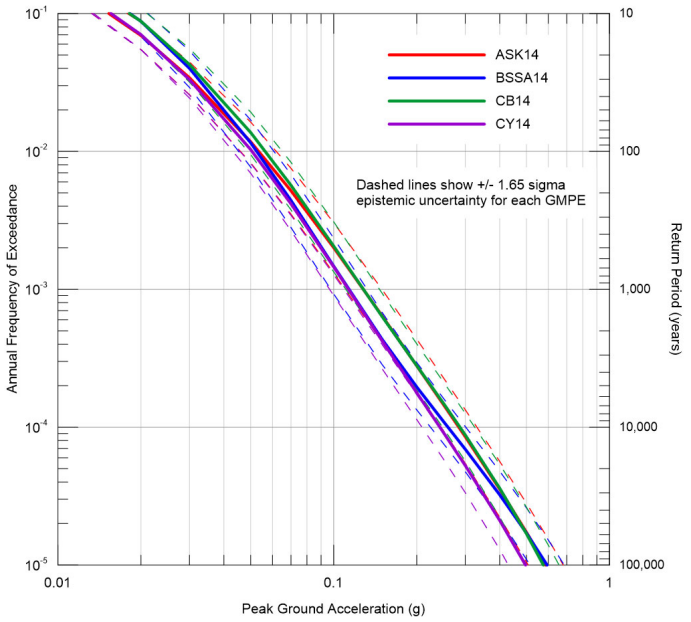

Figure 5-37. Camanche Dam Sensitivity of the Peak Ground Acceleration Hazard to the Selection of Ground Motion Models

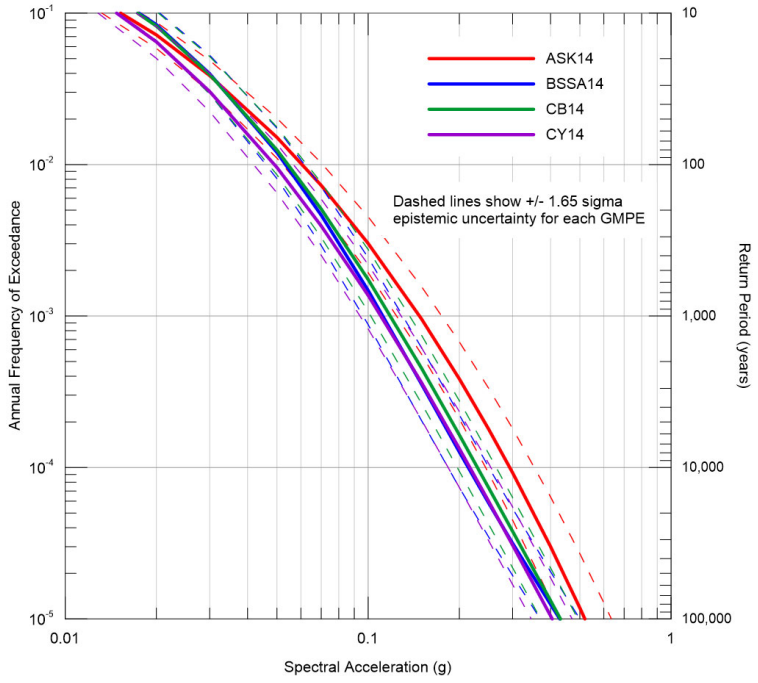

Figure 5-38. Camanche Dam Sensitivity of the 1.0 Sec Spectral Acceleration Hazard to the Selection of Ground Motion Models

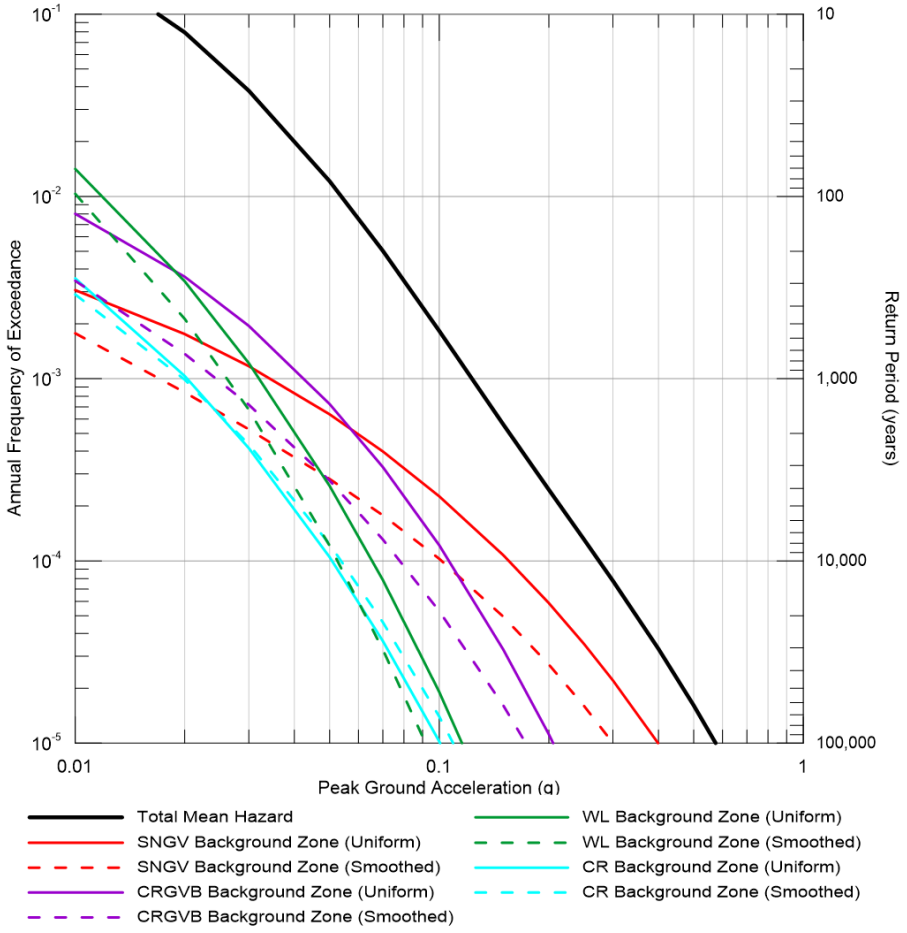

Figure 5-39. Camanche Dam Sensitivity of Horizontal Peak Ground Acceleration Hazard to Background Seismicity

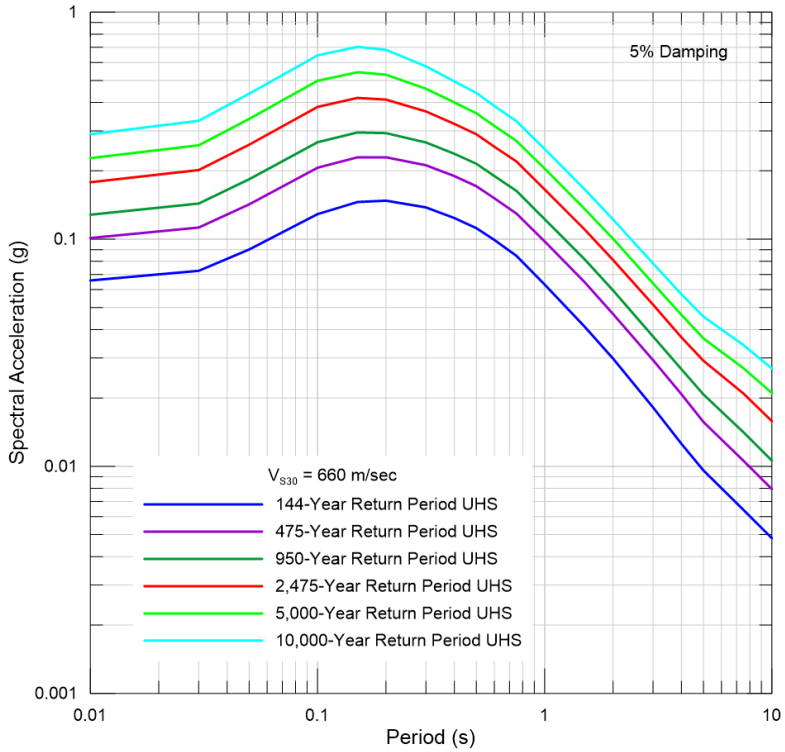

Figure 5-40. Camanche Dam 5%-Damped Uniform Hazard Response Spectra

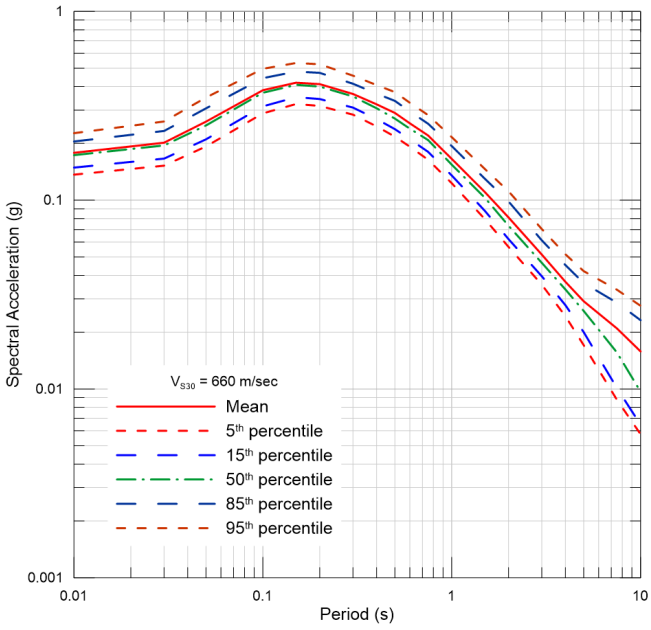

Figure 5-41. Camanche Dam 5%-Damped Mean and Fractile UHRS at a Return Period of 2,475-Years

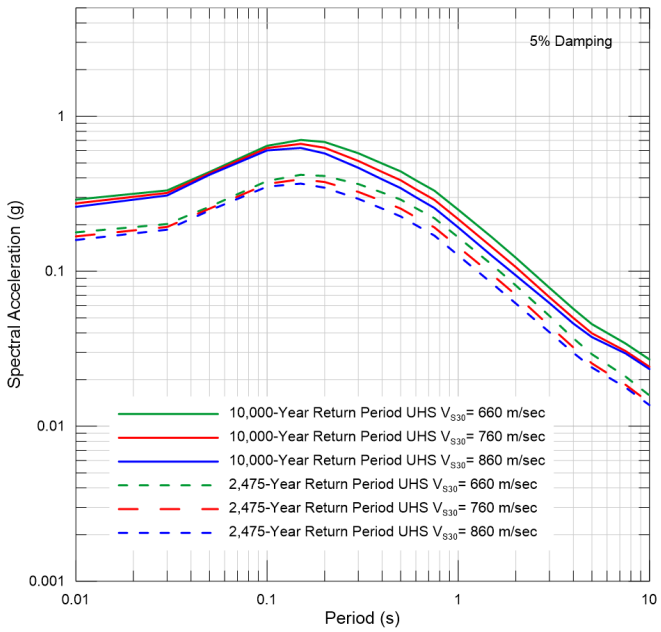

Figure 5-42. Camanche Dam Sensitivity of the 2,475- and 10,000-Year Return Period UHRS to the Selection of V_{S30}

5.3.1 Comparison with USGS National Seismic Hazard Maps

In 1996, the USGS released a “landmark” set of National Hazard Maps for earthquake ground shaking, which was a significant improvement from previous maps they had developed (Frankel et al., 1996). These maps were the result of the most comprehensive analyses of seismic sources and ground motion prediction ever undertaken on a national scale. These maps were subsequently updated by Petersen et al. (2020). The maps are the basis for the National Earthquake Hazard Reduction Program (NEHRP) risk -targeted maximum considered earthquake (MCE_R) maps, which are used in the International Building Code. The most recent maps are for a range of V_{S30} values. For a 2,475-year return period and site class B/C (V_{S30} 760 m/sec), the latest 2018 National Seismic Hazard Maps indicate a PGA of 0.20 g and a 1.0 sec SA of 0.17 g for the dam site.

For comparison purposes the site-specific hazard was calculated for a V_{S30} of 760 m/sec. For a 2,475-year return period, the site-specific PGA is 0.17 g with the 5th and 95th percentile values of 0.13 g and 0.21 g, respectively, for a V_{S30} of 760 m/sec. The site-specific 1.0 sec SA is 0.14 g with the 5th and 95th percentile values of 0.11 and 0.19 g, respectively. The differences are most likely due to the background seismicity. For the USGS maps in California, the background seismicity is based on a statewide seismic rate. That is, the overall rates of earthquakes allocated to the gridded source zones do not directly depend on the observed historical occurrence and rates of earthquakes in the site region, but rather are based on a state-wide rate of earthquakes and a state-wide solution of earthquake rates modeled to occur on fault sources. Whereas in this site-specific study the background seismicity rates are based on more regional seismotectonic zones.

5.4 Camanche Dam DSHA Results

Deterministic analyses were performed for the Waters Peak-Green Springs Run and Ione faults. These are the closest faults to Camanche Dam. The dam lies in the hanging wall of the Ione fault. The San Andreas and Calaveras faults are capable of large magnitude earthquakes, so they were also considered due to their potential to impact the long period ground motions.

Camanche Dam is operated by EBMUD under the jurisdiction of the California DSOD and FERC. DSOD has adopted a “consequence-hazard” matrix (Figure 5-18) that establishes guidelines for selecting the percentile level of ground motions to be used in the seismic safety evaluation of dams (DSOD, 2018). Following this approach, 50th to 84th percentile ground motions are required for Extremely High hazard class dams such as Camanche Dam and given the low slip rate (less than 0.1 mm/yr) for the Waters Peak-Green Springs Run and Ione faults. The 84th percentile would be required for the San Andreas fault, given its very high slip rate (greater than 9 mm/yr).

FERC guidelines (FERC, 2018) allow the percentile level of ground motions to be determined from the average slip rate of the fault. For faults with slip rates greater or equal than 0.9 mm/yr the 84th percentile is to be used, for faults with slip rates less than or equal to 0.3 mm/yr the median (50th percentile) can be used. For faults with slip rates between 0.3 to 0.9 mm/yr FERC (2018) provides the following equation to determine the percentile to be used:

$$\varepsilon = \frac{Log_{10}(\frac{slip\ rate}{0.3})}{Log_{10}(3)}$$

Following FERC guidelines the 50th percentile could be used for the Waters Peak-Green Springs Run and Ione faults, while the 84th percentile would be required for the San Andreas fault.

Based on the very low slip rate for the Water Peak-Green Springs Run and Ione faults, and the criteria for both DSOD and FERC the median 5%-damped horizontal acceleration spectrum was computed. The mean characteristic magnitude of **M** 6.5 was selected based on the unsegmented rupture of the Foothills fault system with the fault geometry based on the Waters Peak-Green Springs Run or Ione. A **M** 8.0 at a rupture distance of 141 km was used for the 84th percentile San Andreas fault, and a **M** 7.25 at a rupture distance of 97.3 km was used for the 84th percentile Calaveras fault in the DSHA calculations. All input parameters for the DSHA are given in Table 5-21. The same ground-motion models as used in the PSHA were used in the DSHA (see Section 4.3).

Figure 5-43 shows the DSHA spectra. The Ione fault gives the largest ground motions for periods less than 1.5 sec, with the San Andreas fault controlling at longer periods. Figure 5-44 shows the median horizontal acceleration response spectra from each ground-motion model and the lognormal mean of the ground-motion models for the Ione fault. CB14 gives the highest ground motions over all periods, while the ASK14 model gives the lowest ground motions over periods less than 3.0 sec.

Sensitivity to the selection of V_{S30} is shown on Figure 5-45. A V_{S30} of 660 m/sec gives the largest ground motions for all periods and is the recommended spectrum at Camanche. The recommended spectrum is the envelop of the V_{S30} and these values are provided in Table 5-22.

The median spectrum for the Ione fault and 84th percentile spectrum for the San Andreas fault are compared to the UHRS on Figure 5-46. The median spectrum for the Ione fault is near the 2,475-year return period UHRS for periods less 0.3 sec, but less than the 144-year return period UHRS at 10 sec. The 84th percentile spectrum for the San Andreas fault is near the 144-year return period UHRS for periods less 0.3 sec, but near the 950-year return period UHRS at longer periods. These differences are due to different spectral slopes. The UHRS is being impacted by moderate size earthquakes of the Foothills fault system and background sources at short periods, while the longer periods are being impacted by the larger magnitude earthquakes of the San Andreas fault and the other more distant high slip rate faults.

Because Camanche Dam is at near-fault distances from the Ione fault, the effect of forward rupture directivity should be considered in the ground motions. Earthquake rupture directivity is a catch-all term generally used to describe the focusing of wave energy along a fault in the direction of rupture, as well as the effects of this phenomenon. In earthquakes on shallow crustal faults, rupture directivity effects cause spatial variations in ground motion amplitude and duration around earthquakes; and differences between the strike-normal and strike-parallel components of horizontal ground motion amplitudes, which also have spatial variation around the fault (Somerville et al. 1997). These variations are generally stronger with increasing spectral period. Most ground motion models do not account for rupture directivity, so the current standard of practice is to apply rupture directivity adjustment models to response spectrum for shallow crustal earthquakes.

The DSHA spectrum for the Ione fault was adjusted for fault directivity using the model of Bayless and Somerville, developed as part of the NGA-West2 Directivity Working Group (Spudich et al. 2013), which is an update to the widely used model of Somerville et al. (1997). The Bayless and Somerville (BS13) model is a function of magnitude, rupture distance, fraction of the fault rupture that lies between the hypocenter and site, and angle between the direction of fault rupture and the direction of waves travelling from fault to the site. Figure 5-47 shows the adjustments to the spectrum for fault normal directivity effects and the values are provided in Table 5-23.

Table 5-21. Camanche Dam DSHA Inputs

NGA-West2 Parameters	Waters Peak – Green Springs Run Fault	Ione Fault	San Andreas Fault	Calaveras Fault
M	6.5	6.5	8.0	7.25
R_{RUP} (km)	14.5	13.0	141.0	97.3
R_{JB} (km)	14.5	9.9	141.0	97.3
R_X (km)	14.5	13.9	141.0	97.3
F_{RV}	0	0	0	0
F_N	1*	1*	0	0
F_{HW}	0	1	0	0
Z_{TOR} (km)	0	0	0	0
Dip	65	75	90	90
V_{S30} (m/sec)	760 ± 100	760 ± 100	760 ± 100	760 ± 100
$Z_{1.0}$ (km)	0.045	0.045	0.045	0.045
$Z_{2.5}$ (km)	0.607	0.607	0.607	0.607
W (km)	16.6	15.5	13	15

R_{RUP} = Closest distance to coseismic rupture
R_{JB} = Closest distance to surface projection of coseismic rupture
R_X = Horizontal distance from top of rupture measured perpendicular to fault strike
F_{RV} = Reverse fault flag (1 = reverse fault)
F_N = Normal fault flag (1 = normal fault)
* (Normal faulting weighted 0.5, strike-slip faulting weighted 0.5)
F_{HW} = Hanging Wall flag (1 = in hanging wall, 0 = in foot wall)
Z_{TOR} = Depth to top of coseismic rupture
Dip = Average dip of rupture plane (degrees)
V_{S30} = The time average shear-wave velocity over a subsurface depth of 30 m
$Z_{1.0}$ = Depth to Vs=1.0 km/sec
$Z_{2.5}$ = Depth to Vs=2.5 km/sec
W = fault width

Table 5-22. Camanche Dam DSHA Spectra (V_{S30} = 660 m/sec)

	Waters Peak – Green Springs Run Fault - Median	Ione Fault - Median	San Andreas Fault – 84th Percentile	Calaveras Fault – 84th Percentile
Period (sec)	**SA (g)**	**SA (g)**	**SA (g)**	**SA (g)**
0.01 (PGA)	0.156	0.181	0.0769	0.0696
0.020	0.159	0.185	0.0770	0.0700
0.030	0.174	0.203	0.0814	0.0753
0.050	0.219	0.257	0.0936	0.0909
0.075	0.277	0.327	0.108	0.111
0.100	0.318	0.374	0.118	0.125
0.150	0.366	0.422	0.130	0.139
0.200	0.368	0.421	0.138	0.143
0.250	0.342	0.388	0.145	0.143
0.300	0.308	0.348	0.149	0.139
0.400	0.253	0.285	0.144	0.126
0.500	0.211	0.238	0.137	0.113
0.750	0.143	0.161	0.112	0.0861
1.000	0.104	0.117	0.0868	0.0649
1.500	0.0627	0.0708	0.0639	0.0438
2.000	0.0433	0.0493	0.0490	0.0319
3.000	0.0251	0.0279	0.0345	0.0205
4.000	0.0164	0.0179	0.0264	0.0147
5.000	0.0114	0.0122	0.0209	0.0110
7.500	0.00529	0.00554	0.0142	0.00659
10.000	0.00306	0.00323	0.00971	0.00424

Table 5-23. Camanche Dam DSHA Fault Normal Spectra

	Ione fault - Median
Period (sec)	**SA (g)**
0.01 (PGA)	0.181
0.020	0.185
0.030	0.203
0.050	0.257
0.075	0.327
0.100	0.374
0.150	0.422
0.200	0.421
0.250	0.388
0.300	0.348
0.400	0.285
0.500	0.238
0.750	0.161
1.000	0.117
1.500	0.0708
2.000	0.0571
3.000	0.0369
4.000	0.0236
5.000	0.0166
7.500	0.00754
10.000	0.00444

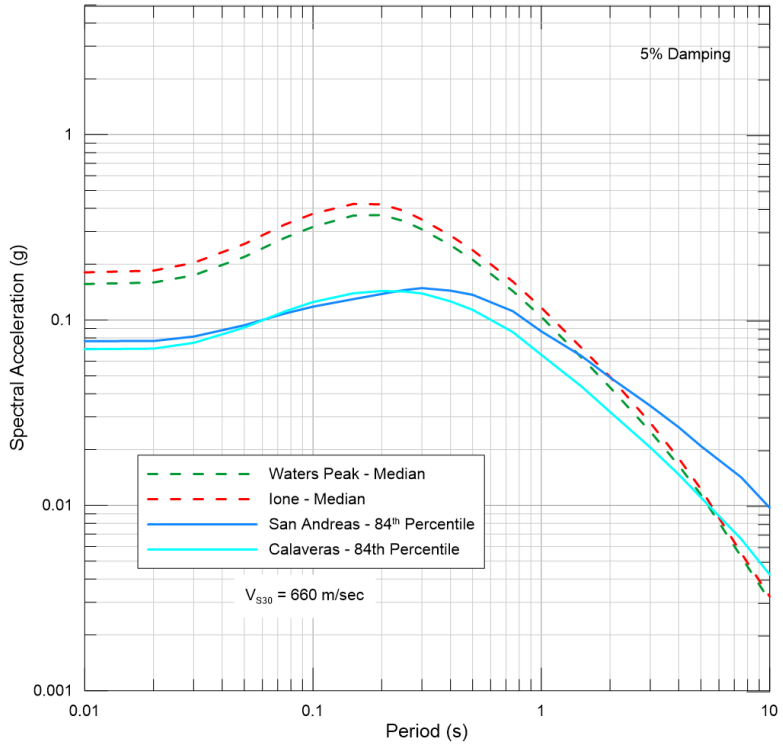

Figure 5-43. Camanche Dam DSHA Spectra Summary

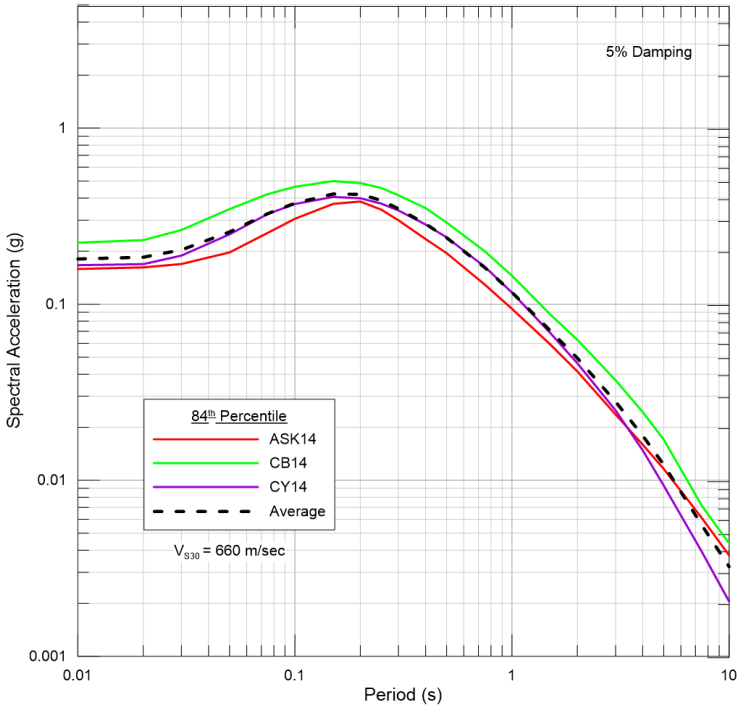

Figure 5-44. Camanche Dam Sensitivity to the Selection of Ground Motion Models for the 5%-Damped 84th Percentile DSHA Spectra for the Ione Fault

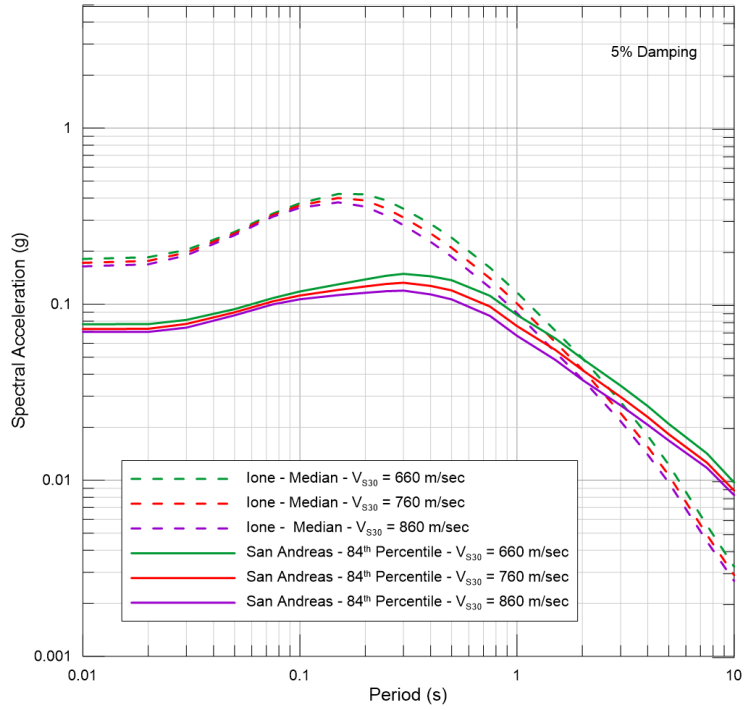

Figure 5-45. Camanche Dam Sensitivity to the Selection of V_{S30} for the DSHA Spectra

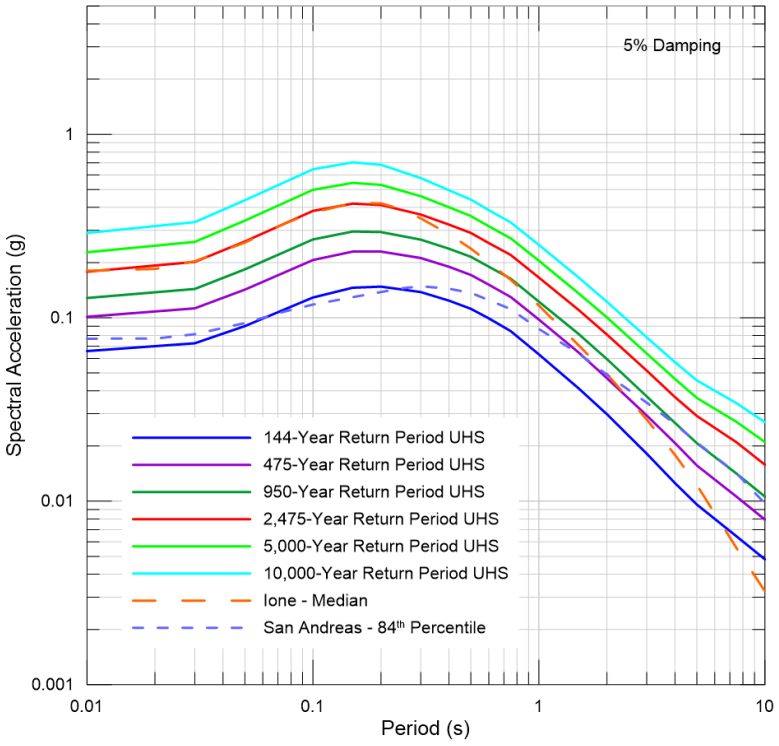

Figure 5-46. Camanche Dam Comparison of 5%-Damped Uniform Hazard Response Spectra and Deterministic Spectra for the Ione Fault

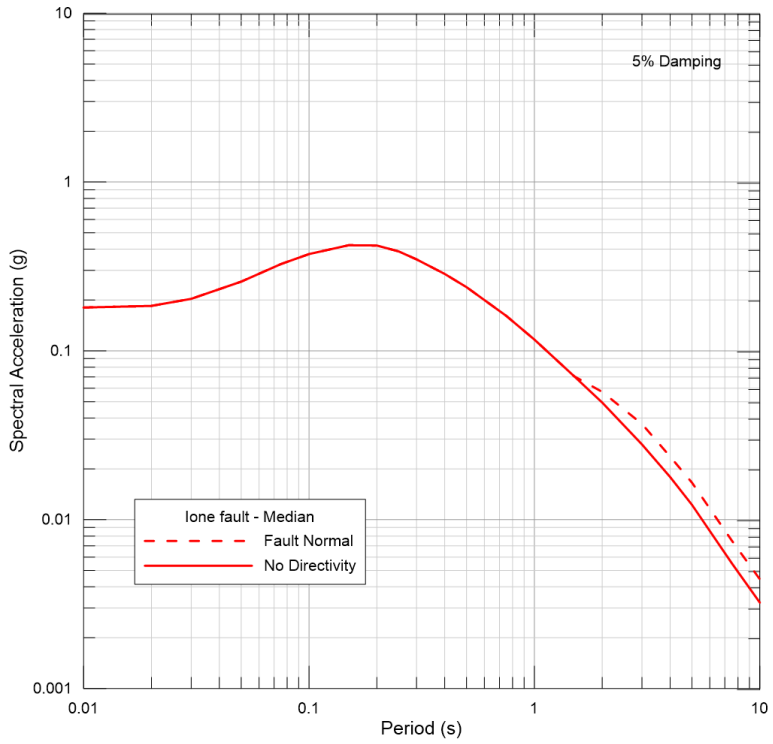

Figure 5-47. Camanche Dam DSHA Spectra Adjusted for Fault Normal Directivity

6. ASCE7-16

The criteria for site-specific design ground motions is provided in the engineering standard ASCE 7-16, Chapter 21 *Site-Specific Ground Motion Procedures for Seismic Design*, Section 21.2.

ASCE 7-16 requires the use of maximum direction ground motions. Ground motion prediction models (i.e., NGA-West2) provide the geometric mean (specifically GMRotD50) of the horizontal components. Scaling factors have been developed (e.g., Shahi and Baker, 2014) to convert to maximum direction. These scale factors are applied to the 2,475-year UHRS and 84th percentile deterministic spectra.

ASCE 7-16 also requires the development of risk-targeted maximum considered earthquake response spectra determined from the PSHA. Previous building codes have used the 2,475-year return period (2% in 50-year exceedance frequency) ground motions as the probabilistic maximum considered earthquake (MCE). ASCE 7-16 requires estimation of ground motions that are expected to achieve a 1% probability of collapse in 50 years. To obtain these probabilistic ground motions, the hazard curve is iteratively integrated with a lognormal probability density function representing the collapse fragility. For a site-specific analysis, ASCE 7-16 Chapter 21 provides two methods to calculate the probabilistic ground motions. Method 1 corrects the site-specific 2,475-year return period UHRS to risk-targeted ground motions by applying a risk coefficient, C_R. These risk-coefficients have been calculated for the continental U.S. by the USGS and are based on the 2014 USGS hazard curves, which are the basis for the 2014 USGS National Seismic Hazard Maps. Method 2 computes the risk-targeted ground motions by directly integrating the site-specific hazard curve with a collapse fragility function. For this study, Method 1 was used to compute the risk-targeted maximum considered earthquake (MCE_R) and design response spectrum (DRS).

As in previous versions (ASCE 7-10 and CBC 2016), ASCE 7-16 caps the probabilistic ground motions with the site-specific deterministic ground motions; thus the site-specific MCE_R is the minimum of the probabilistic MCE_R and the deterministic MCE. The site-specific DRS is the maximum of two-thirds the MCE_R and 80% of the general code spectra for the appropriate site class.

6.1 Camanche Dam

6.1.1 MCE_R and DRS

The procedure described above was followed to obtain site-specific MCE_R and DRS for Camanche Dam. Figures 6-1 to 6-4 illustrate the development of the site-specific MCE_R and DRS.

Figure 6-1 shows the conversion of the 84th percentile deterministic spectra from geometric mean to maximum direction. The scaling factors of Shahi and Baker (2014) are used. Previous versions of ASCE 7, included a minimum deterministic lower limit response spectrum which the site-specific deterministic MCE_R spectrum could not fall below. This has been modified according to ASCE 7-16 Supplement 1, such that if the largest spectral response acceleration of the resulting maximum direction deterministic response spectrum is less than 1.5 times the short period site coefficient, F_a, then the maximum direction deterministic response spectrum is scaled by a factor such that the maximum response spectral acceleration value is equal to 1.5 times F_a. F_a is determined by using Table 11.4.1 for Site Classes A, B, C, and D with the value of S_S, the spectral response acceleration parameter at short periods, taken as 1.5. The corresponding value of F_a in this table is 1.2, therefor the deterministic maximum response spectral acceleration value should not be less than 1.8 g. The site-specific deterministic MCE is shown on Figure 6-1.

Figure 6-2 shows the adjustment of the site-specific 2,475-year return period mean UHRS to the maximum direction and the application of the risk coefficients to obtain the probabilistic MCE_R response spectrum. First, the maximum direction scaling factors are applied and then the risk-coefficient. The risk coefficient, C_R, is defined as C_{RS} at periods less than or equal to 0.2 sec and C_{R1} for periods greater than or equal to 1.0 sec, with linear interpolation used to define C_R for periods between 0.2 and 1.0 sec. For this project, C_{RS} equals 0.966 and C_{R1} equals 0.955.

After determining the site-specific probabilistic (2,475-year) and deterministic MCE_R (Table 6-1), the two are compared and the minimum taken, which for this project is the probabilistic MCE_R (Figure 6-3). In accordance with ASCE 7-16, two-thirds of the site-specific MCE_R is compared with 80% of the ASCE 7-16 code general DRS at Site Class C (Table 6-1), with the maximum of these being the site-specific DRS as shown in Figure 6-4. Finally, the site-specific MCE_R is adjusted so that it is not less than 150-percent of the DRS. The values for the site-specific MCE_R and DRS are provided in Table 6-2.

Table 6-1. Camanche Dam Site-Specific MCE_R, DRS and 80% General Design Response Spectrum

	Deterministic MCE_R	Probabilistic MCE_R	80% General Design Response Spectrum
Period (sec)	**SA (g)**	**SA (g)**	**SA (g)**
0.010	0.724	0.205	0.137
0.020	0.742	0.218	0.153
0.030	0.822	0.232	0.169
0.040	0.936	0.266	0.186
0.050	1.051	0.300	0.202
0.060	1.172	0.328	0.218
0.070	1.293	0.356	0.234
0.080	1.396	0.384	0.250
0.090	1.481	0.412	0.266
0.100	1.565	0.440	0.283
0.112	1.619	0.451	0.302
0.140	1.741	0.477	0.302
0.200	1.800	0.482	0.302
0.250	1.676	0.458	0.302
0.300	1.516	0.430	0.302
0.400	1.262	0.382	0.302
0.500	1.064	0.343	0.302
0.561	0.987	0.318	0.302
0.700	0.808	0.275	0.242
0.800	0.704	0.248	0.212
0.900	0.624	0.222	0.188
1.000	0.544	0.196	0.170
1.500	0.333	0.131	0.113
2.000	0.232	0.0959	0.0848
3.000	0.132	0.0615	0.0565
4.000	0.0839	0.0445	0.0424
5.000	0.0576	0.0351	0.0339
6.000	0.0453	0.0313	0.0283
7.000	0.0328	0.0275	0.0242
8.000	0.0244	0.0244	0.0212
9.000	0.0200	0.0219	0.0188
10.000	0.0156	0.0195	0.0170

Table 6-2. Camanche Dam Site-Specific ASCE 7-16 Response Spectra

	DRS	MCE_R
Period (sec)	**SA (g)**	**SA (g)**
0.010	0.137	0.206
0.020	0.153	0.230
0.030	0.169	0.254
0.040	0.186	0.278
0.050	0.202	0.303
0.060	0.219	0.328
0.070	0.237	0.356
0.080	0.256	0.384
0.090	0.274	0.412
0.100	0.293	0.440
0.112	0.302	0.453
0.140	0.318	0.477
0.200	0.321	0.482
0.250	0.305	0.458
0.300	0.302	0.453
0.400	0.302	0.453
0.500	0.302	0.453
0.561	0.302	0.453
0.700	0.242	0.363
0.800	0.212	0.318
0.900	0.188	0.283
1.000	0.170	0.254
1.500	0.113	0.170
2.000	0.0848	0.127
3.000	0.0565	0.0848
4.000	0.0424	0.0636
5.000	0.0339	0.0509
6.000	0.0283	0.0424
7.000	0.0242	0.0363
8.000	0.0212	0.0318
9.000	0.0188	0.0283
10.000	0.0170	0.0254

6.1.2 Design Acceleration Parameters

Design acceleration parameters as per ASCE 7-16, Section 21.4 are provided in Table 6-3. The site-specific S_{DS} is taken as the 0.2 sec SA, except not less than 90 percent of the SA at any period greater than 0.2 sec. The maximum SA occurs at 0.2 sec. ASCE 7-16 requires the parameter S_{D1} be taken as the maximum value of the product, T*SA, for periods from 1 to 2 sec for sites with V_{S30} > 366 m/s. In this period band the maximum value of T*SA occurs at 1.0-sec period and is equal to 1.0*0.170 = 0.170 g. The parameters S_{MS} and S_{M1} are 1.5 times S_{DS} and S_{D1}, respectively. PGA_M is the lesser of the geometric mean PGA of the deterministic and probabilistic hazard, that is the PGA not adjusted for maximum direction or risk targeted. However, according to ASCE7-16, the deterministic geometric mean PGA shall not be taken as lower than 0.5*F_{PGA}, where F_{PGA} is determined to be 1.2 for this site.

Table 6-3. Camanche Dam Site-Specific Design Acceleration Parameters per Sect. 21.4 of ASCE 7-16

	Spectral Value (g)
S_{DS}	0.321
S_{D1}	0.170
S_{MS}	0.482
S_{M1}	0.254
PGA_M	0.178

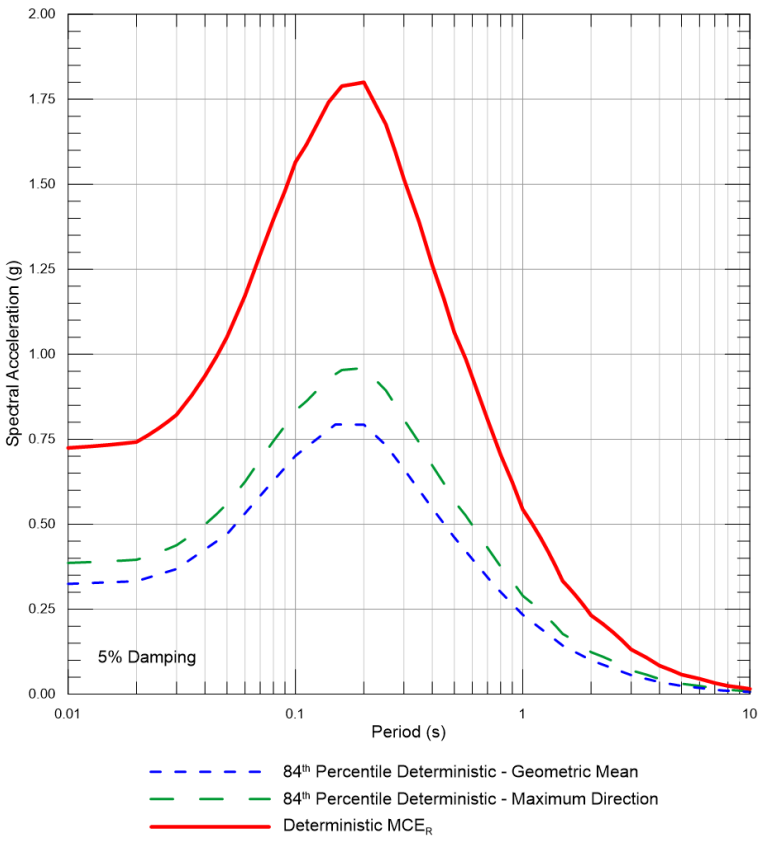

Figure 6-1. Camanche Dam Deterministic MCE Ground Motions

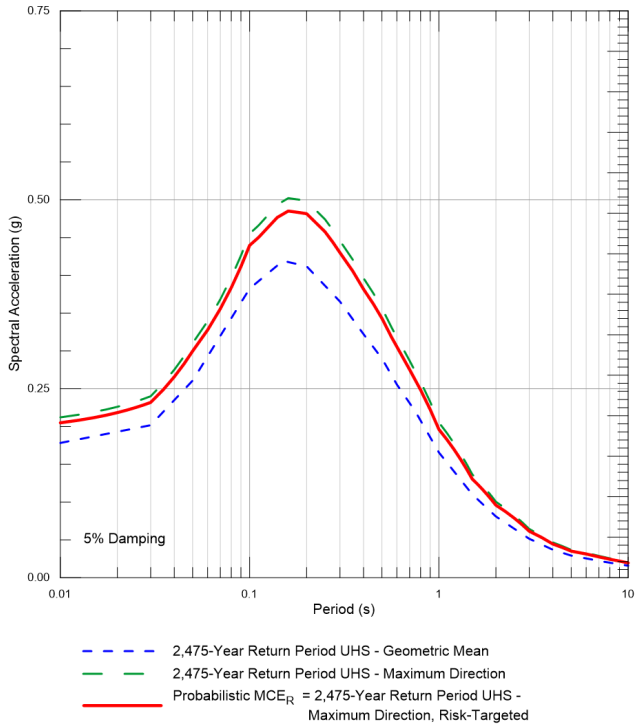

Figure 6-2. Camanche Dam Probabilistic MCE_R Ground Motions

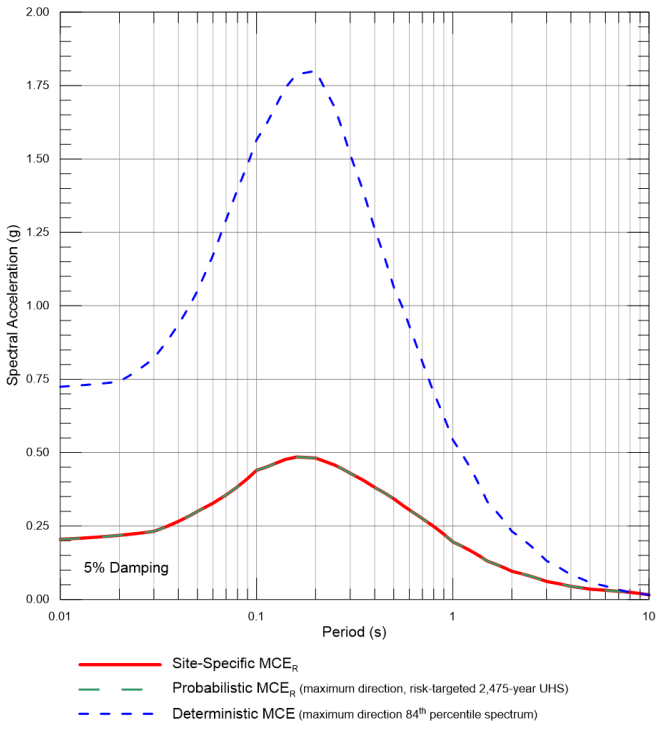

Figure 6-3. Camanche Dam Site-Specific MCE_R

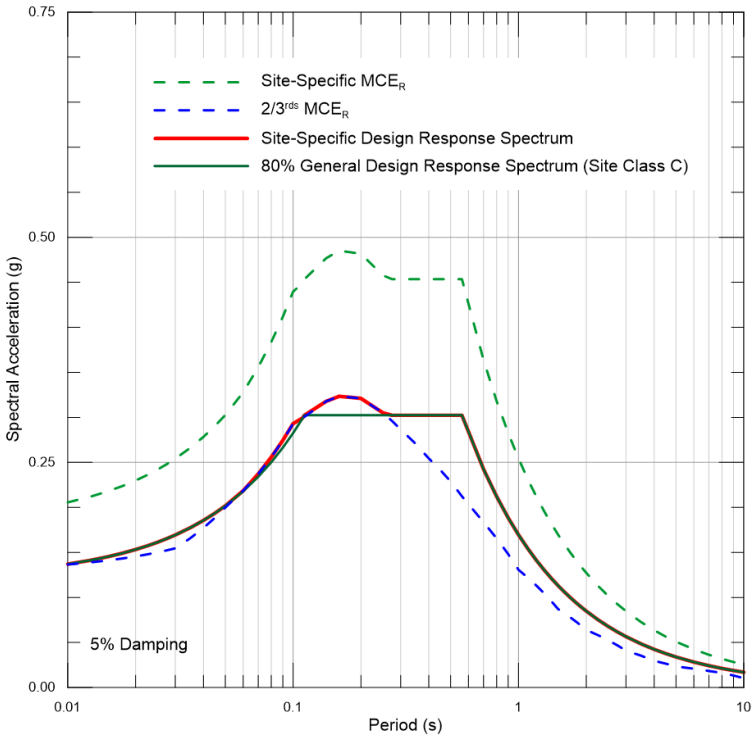

Figure 6-4. Camanche Dam Design Response Spectra

6.2 Pardee Dam

6.2.1 MCE$_R$ and DRS

The procedure described above was followed to obtain site-specific MCE$_R$ and DRS for Pardee Dam. Figures 6-5 to 6-8 illustrate the development of the site-specific MCE$_R$ and DRS.

Figure 6-5 shows the conversion of the 84th percentile deterministic spectra from geometric mean to maximum direction. The scaling factors of Shahi and Baker (2014) are used. Previous versions of ASCE 7, included a minimum deterministic lower limit response spectrum which the site-specific deterministic MCE$_R$ spectrum could not fall below. This has been modified according to ASCE 7-16 Supplement 1, such that if the largest spectral response acceleration of the resulting maximum direction deterministic response spectrum is less than 1.5 times the short period site coefficient, F_a, then the maximum direction deterministic response spectrum is scaled by a factor such that the maximum response spectral acceleration value is equal to 1.5 times F_a. F_a is determined by using Table 11.4.1 for Site Classes A, B, C, and D with the value of S_S, the spectral response acceleration parameter at short periods, taken as 1.5. The corresponding value of F_a in this table is 0.9, therefor the deterministic maximum response spectral acceleration value should not be less than 1.35 g. The site-specific deterministic MCE is shown on Figure 6-5.

Figure 6-6 shows the adjustment of the site-specific 2,475-year return period mean UHRS to the maximum direction and the application of the risk coefficients to obtain the probabilistic MCE$_R$ response spectrum. First, the maximum direction scaling factors are applied and then the risk-coefficient. The risk coefficient, C_R, is defined as C_{RS} at periods less than or equal to 0.2 sec and C_{R1} for periods greater than or equal to 1.0 sec, with linear interpolation used to define C_R for periods between 0.2 and 1.0 sec. For this project, C_{RS} equals 0.970 and C_{R1} equals 0.956.

After determining the site-specific probabilistic (2,475-year) and deterministic MCE_R (Table 6-4), the two are compared and the minimum taken, which for this project is the probabilistic MCE_R (Figure 6-7). In accordance with ASCE 7-16, two-thirds of the site-specific MCE_R is compared with 80% of the ASCE 7-16 code general DRS at Site Class B (Table 6-4), with the maximum of these being the site-specific DRS as shown in Figure 6-8. Finally, the site-specific MCE_R is adjusted so that it is not less than 150-percent of the DRS. The values for the site-specific MCE_R and DRS are provided in Table 6-5.

Table 6-4. Pardee Dam Site-Specific MCE_R, DRS and 80% General Design Response Spectrum

	Deterministic MCE_R	Probabilistic MCE_R	80% General Design Response Spectrum
Period (sec)	**SA (g)**	**SA (g)**	**SA (g)**
0.010	1.062	0.210	0.0844
0.020	1.220	0.239	0.0962
0.030	1.546	0.268	0.108
0.040	1.776	0.330	0.120
0.050	2.006	0.391	0.132
0.060	2.186	0.427	0.143
0.070	2.367	0.463	0.155
0.080	2.463	0.498	0.167
0.092	2.479	0.542	0.181
0.110	2.499	0.574	0.181
0.140	2.530	0.586	0.181
0.200	2.230	0.499	0.181
0.250	1.900	0.435	0.181
0.300	1.633	0.367	0.181
0.400	1.298	0.279	0.181
0.461	1.145	0.248	0.181
0.600	0.921	0.191	0.139
0.700	0.794	0.169	0.119
0.800	0.688	0.149	0.105
0.900	0.603	0.131	0.0929
1.000	0.518	0.114	0.0836
1.500	0.300	0.0723	0.0558
2.000	0.233	0.0517	0.0418
3.000	0.153	0.0326	0.0279
4.000	0.100	0.0237	0.0209
5.000	0.0729	0.0192	0.0167
6.000	0.0577	0.0175	0.0139
7.000	0.0423	0.0157	0.0119
8.000	0.0321	0.0143	0.0105
9.000	0.0272	0.0131	0.00929
10.000	0.0222	0.0120	0.00836

Table 6-5. Pardee Dam Site-Specific ASCE 7-16 Response Spectra

	DRS	MCE_R
Period (sec)	**SA (g)**	**SA (g)**
0.010	0.140	0.210
0.020	0.159	0.239
0.030	0.179	0.268
0.040	0.220	0.330
0.050	0.261	0.391
0.060	0.285	0.427
0.070	0.308	0.463
0.080	0.332	0.498
0.092	0.361	0.542
0.110	0.383	0.574
0.140	0.390	0.586
0.200	0.332	0.499
0.250	0.290	0.435
0.300	0.245	0.367
0.400	0.186	0.279
0.461	0.181	0.272
0.600	0.139	0.209
0.700	0.119	0.179
0.800	0.105	0.157
0.900	0.0929	0.139
1.000	0.0836	0.125
1.500	0.0558	0.0836
2.000	0.0418	0.0627
3.000	0.0279	0.0418
4.000	0.0209	0.0314
5.000	0.0167	0.0251
6.000	0.0139	0.0209
7.000	0.0119	0.0179
8.000	0.0105	0.0157
9.000	0.00929	0.0139
10.000	0.00836	0.0125

6.2.2 Design Acceleration Parameters

Design acceleration parameters as per ASCE 7-16, Section 21.4 are provided in Table 6-6. The site-specific S_{DS} is taken as the 0.2 sec SA, except not less than 90 percent of the SA at any period greater than 0.2 sec. The maximum SA occurs at 0.2 sec. ASCE 7-16 requires the parameter S_{D1} be taken as the maximum value of the product, T*SA, for periods from 1 to 2 sec for sites with V_{S30} > 366 m/s. In this period band the maximum value of T*SA occurs at 1.0-sec period and is equal to 1.0*0.0836 = 0.0836 g. The parameters S_{MS} and S_{M1} are 1.5 times S_{DS} and S_{D1}, respectively. PGA_M is the lesser of the geometric mean PGA of the deterministic and probabilistic hazard, that is the PGA not adjusted for maximum direction or risk targeted. However, according to ASCE7-16, the deterministic geometric mean PGA shall not be taken as lower than 0.5*F_{PGA}, where F_{PGA} is determined to be 0.9 for this site.

Table 6-6. Pardee Dam Site-Specific Design Acceleration Parameters per Sect. 21.4 of ASCE 7-16

	Spectral Value (g)
S_{DS}	0.332
S_{D1}	0.0836
S_{MS}	0.499
S_{M1}	0.125
PGA_M	0.182

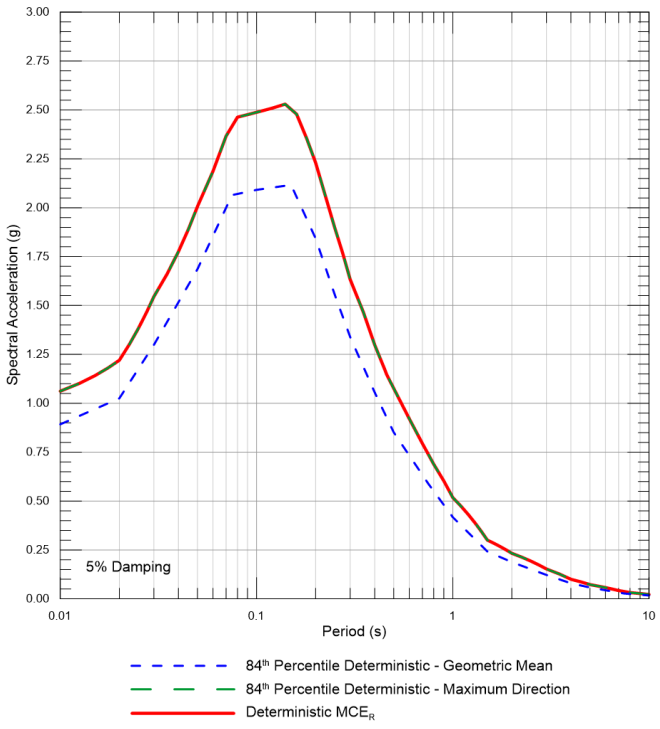

Figure 6-5. Pardee Dam Deterministic MCE Ground Motions

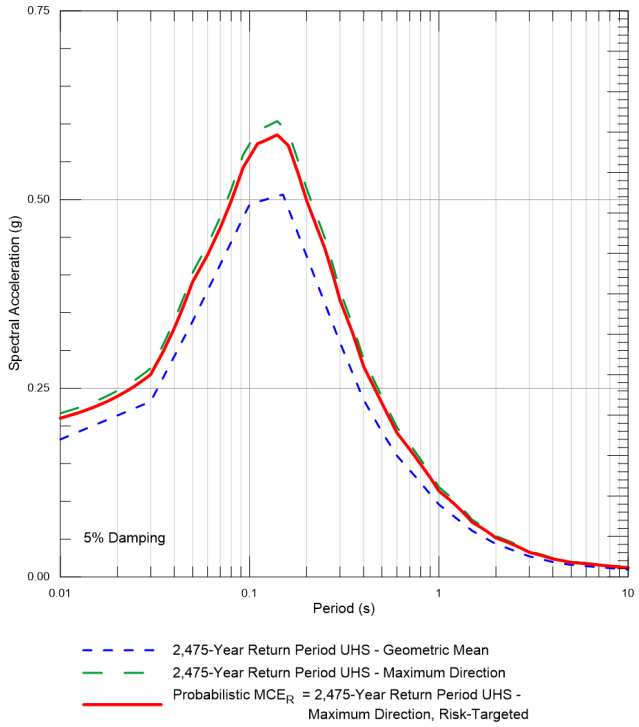

Figure 6-6. Pardee Dam Probabilistic MCE_R Ground Motions

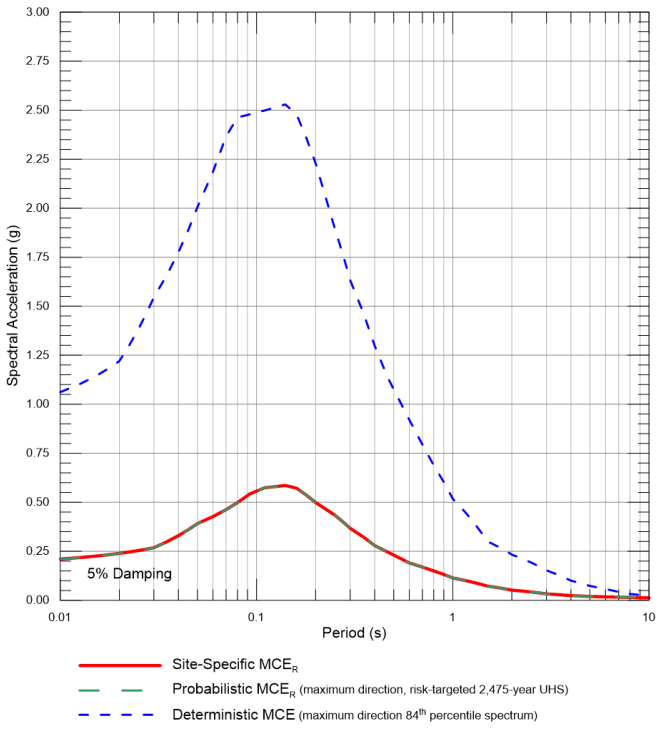

Figure 6-7. Pardee Dam Site-Specific MCE_R

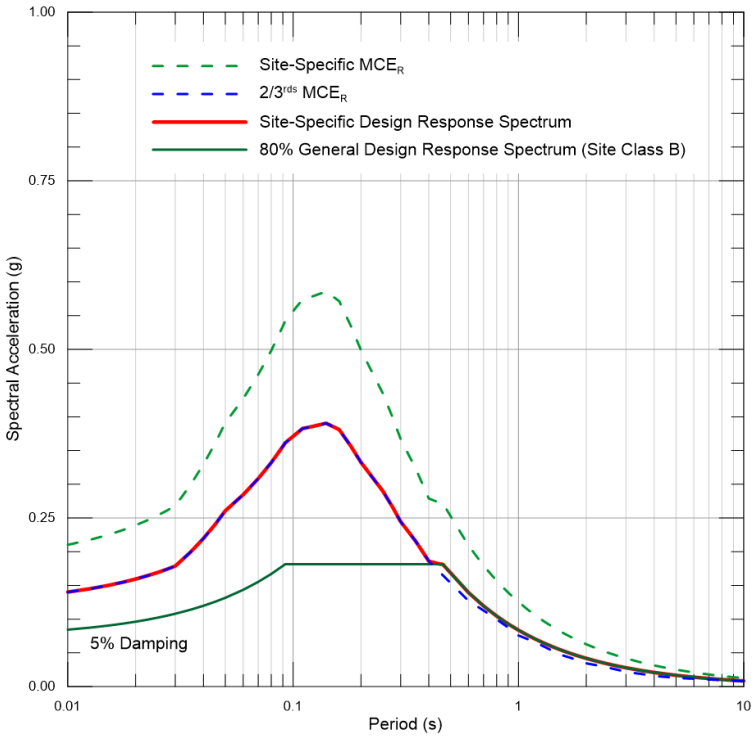

Figure 6-8. Pardee Dam Design Response Spectra

7. Conclusions

At the request of the East Bay Municipal Utility District (EBMUD), a site-specific seismic hazard analysis has been performed at the Pardee and Camanche Dams, located in the western foothills of the Sierra Nevada. As both dams are regulated by FERC and DSOD, the hazard analysis was performed to conform with Chapter 13 of FERC's Engineering Guidelines (FERC, 2018), as well as DSOD's Inspection and Reevaluation Protocols (DSOD, 2018). Both dams are classified as a High-Hazard Dams according to FERC criteria, and the dam hazard is classified as Extremely High by the California DSOD.

Pardee Dam and spillway is founded on the Gopher Ridge metavolcanics, which is described as predominantly massive, strong and hard, and provides a competent foundation for the dam. Based on downhole P- and S-wave measurements from three borings at the Pardee Dam site, as well as seismic refraction surveys, a V_{S30} of 1,300 $\pm$ 100 m/sec was estimated for the dam foundation bedrock.

Camanche Dam was excavated directly into the Miocene-Pliocene Mehrten Formation, which varies in rock type from mudflow or agglomerate, to conglomerate, sandstone, siltstone, and claystone. Downhole seismic velocity measurements in the Mehrten Formation were collected from sixteen wells at the Main Dam, Dike 2 and Dike 5. The V_{S30} of 760 m/sec $\pm$ 100 m/sec was estimated for the dam foundation bedrock.

The NGA-West2 ground motion models by ASK14, BSSA14, CB14, CY14 were used in the PSHA and DSHA, equally weighted, except for faults for which the site lies in the hanging wall, then only the ground motion models by ASK14, CB14, CY14 were used, equally weighted, following FERC guidelines. Based on interaction with FERC for dams in extensional tectonic regions, normal faults were modeled as a strike-slip fault and a normal fault, each equally weighted. For Pardee Dam, the hazard was run for 760 m/sec, then adjusted to hard rock site conditions using the linear site adjustment factors of Al Atik et al. (2022).

The PSHA at Pardee Dam is controlled by the more distant, highly active faults, such as the San Andreas, Calaveras and Hayward at short return periods, but the faults of the Foothills fault system contribute the most to the total mean hazard at return periods greater than 1,000-years. The recommended UHRS are the envelope of the UHRS calculated for the range of V_{S30} values. The PGA at return period of 2,475-years is 0.182 g and at 10,000-years is 0.409 g. The 1.0 sec SA values are 0.0959 g and 0.171 g at return periods of 2,475- and 10,000-years, respectively. The recommended DSHA spectrum is the median enveloped over the range of V_{S30} values for the Waters Peak-Green Spring Run fault, modeled as a **M** 6.5 at a rupture distance of 0.17 km. The PGA is 0.496 g and the 1.0 sec SA value is 0.208 g. The Waters Peak-Green Springs Run fault median spectrum is near the 10,000-year return period UHRS for periods less than 3.0 sec. Fault Normal directivity for the median Waters Peak-Green Spring Run fault has also been provided.

The PSHA at Camanche Dam is controlled by the more distant, highly active faults, such as the San Andreas, Calaveras and Hayward at short return periods, but the SNGV background source controls the hazard at long return periods at PGA. At 1.0 sec SA the San Andreas fault is the most significant contributor to the total mean hazard over most return periods. The recommended UHRS are the envelope of the UHRS calculated for the range of V_{S30} values, in this case a V_{S30} of 660 m/sec. The PGA at return period of 2,475-years is 0.178 g and at 10,000-years is 0.290 g. The 1.0 sec SA values are 0.166 g and 0.249 g at return periods of 2,475- and 10,000-years, respectively. The recommended DSHA spectrum is the median enveloped over the range of V_{S30} values (i.e. V_{S30} of 660 m/sec) for the Ione fault, modeled as a **M** 6.5 at a rupture distance of 13.0 km. The PGA is 0.181 g and the 1.0 sec SA value is 0.117 g. However, for structures sensitive to long-periods, the 84th percentile San Andreas should also be utilized, as it controls the DSHA for periods greater than 1.5 sec. The median spectrum for the Ione fault is near the 2,475-year return period UHRS for periods less 0.3 sec, but less than the 144-year return period UHRS at 10 sec. The 84th percentile spectrum for the San Andreas fault is near the 144-year return period UHRS for periods less 0.3 sec, but near the 950-year return period UHRS at longer periods. Fault Normal directivity for the median Ione fault has also been provided.

Site-spefic DRS and MCE_R spectra and design acceleration parameters have been developed per the engineering standard ASCE 7-16, Chapter 21 *Site-Specific Ground Motion Procedures for Seismic Design*, Section 21.2.

8. References

Abrahamson, N.A. and Silva, W.J., 1997, Empirical response spectral attenuation relations for shallow crustal earthquakes: Seismological Research Letters, v. 68, p. 94-127.

Abrahamson, N.A., Silva, W.J., and Kamai, R., 2014, Summary of the ASK14 ground-motion relation for active crustal regions: Earthquake Spectra, v. 30, p. 1025-1055.

Aki, K., 1983, Seismological evidence in support of the existence of “Characteristic Earthquakes”: Earthquake Notes, v. 54, p. 60-61.

Al Atik, A., Gregor, N.J., Abrahamson, N.A., and Kottke, A.R., 2022, GMPE-consistent hard-rock site adjustment factors for Western North America: Earthquake Spectra, Vol. 38, p.2371–2397

Al Atik, L. and Youngs, R.R., 2014, Epistemic uncertainty for NGA-West2 models: Earthquake Spectra, v. 30, p. 1301-1318.

Anderson, L.W. and Piety, L.A., 2001, Geologic seismic source characterization of the San Luis-O'Neill area, eastern Diablo Range, California for B.F. Sisk and O'Neill Forebay dams, San Luis Unit, Central Valley Project, California: U.S. Bureau of Reclamation, Seismotectonic Report 2001-2, 76 p

Anderson, J.G., 1979, Estimating the seismicity from geological structure for seismic risk studies: Bulletin of the Seismological Society of America, v. 69, p. 135-158.

Anderson, L.W. and Ake, J.P., 2008, Probabilistic seismic hazard analysis for Folsom Dam and Mormon Island Auxiliary Dam – Auburn-Folsom South Unit, American River Division, Central Valley Project, California: Seismotectonic Report 2008-3.

ASCE 7-16, 2016, Minimum design loads and associated criteria for buildings and other structures: American Society of Civil Engineers, Reston, Virginia.

ASCE 7-16, 2018, Minimum design loads and associated criteria for buildings and other structures, Supplement 1: American Society of Civil Engineers, Reston, Virginia.

Atwater, B.F. 1982. Geologic maps of the Sacramento-San Joaquin Delta, California: U.S. Geological Survey Miscellaneous Field Studies Map MF-1401.

Atwater, T., 1970, Implications of plate tectonics for the Cenozoic tectonic evolution of western North America: Geological Society of America Bulletin, v. 81, p. 3513-3536.

Bakun, W.H. and Lindh, A.G., 1985, Potential for future damaging shocks on the Calaveras fault, California: U.S. Geological Survey, Open-File Report 85-754, 266-279 p.

Bakun, W.H., 1980, Seismic activity on the southern Calaveras fault in central California: Bulletin of the Seismological Society of America, v. 70, p. 1,181-1,197.

Bakun, W.H., Clark, M.M., Cockerham, R.S., Ellsworth, W.L., Lindh, A.G., Prescott, W.H., Shakal, A.F. and Spudich, P., 1984, The 1984 Morgan Hill, California, earthquake: Science, v. 225, p. 288-291.

Bateman, P.C. and Eaton, J.P., 1967, Sierra Nevada Batholith: Science, v. 158, p. 1407-1410.

Bechtel Corporation, 1961, Camanche Dam and Reservoir Geologic Report, East Bay Municipal Utility District Mokelumne River Development

Berger, G. W., T. L. Sawyer, and J. R. Unruh, 2010, Single- and multigrain luminescence dating of sediments related to the Greenville fault, eastern San Francisco Bay area, California: Bulletin of the Seismological Society of America, 100, 1051–1072

Bindi, D., Massa, M., Luzi, L., Ameri, G., Pacor, F., Puglia, R., and Augliera, P., 2014, Pan-European ground-motion prediction equations for the average horizontal component of PGA, PGV, and 5%-damped PSA at spectral periods up to 3.0 s using the RESOURCE dataset: Bulletin of Earthquake Engineering, v. 12, p. 391 – 442.

Boore, D.M., Stewart, J.P., Seyhan, E., and Atkinson, G.M., 2014, NGA-West2 equations for predicting PGA, PGV, and 5%-damped PSA for shallow crustal earthquakes: Earthquake Spectra, v. 30, p. 1057-1085.

Bormann, J.M., Hammond, W.C. Kreemer, C. and Blewitt, G., 2012, Using GPS measurements of active crustal deformation to estimate slip rates on the Honey Lake/Warm Springs and Mohawk Valley fault systems, Northern Walker Lane: Friends of the Pleistocene, 2012 Pacific Cell, Field Trip Guidebook entitled “Neotectonics of the Lake Tahoe and Carson and Sierra Valleys”, compiled by: Gordon Seitz, p. 226-231.

Campbell, K.W. and Bozorgnia, Y., 2014, NGA-West2 ground motion model for the average horizontal components of PGA, PGV, and 5%-damped linear acceleration response spectra: Earthquake Spectra, v. 30, p. 1087-1115.

Cao, T., Bryant, W.A, Rowshandel, B., Branum, D., Wills, C.J., 2003, The revised 2002 California probabilistic seismic hazard maps, June 2003: California Geological Survey, http://www.consrv.ca.gov/CGS/rghm/psha/fault_parameters/pdf/2002_CA_Hazard_Maps.pdf

California Division of Oil and Gas (CDOG). 1982. Oil and gas fields, Northern California: Volume 3 of Publication TR10. State of California.

Chiou, B-S.J. and Youngs, R.R., 2014, Update of the Chiou and Youngs NGA ground motion model for average horizontal component of peak ground motion and response spectra: Earthquake Spectra, v. 30, p. 1117-1153.

Clahan, K.B., Wagner, D., Bezore, S., Saucedo, G., and Gutierrex, C., 2005, New geologic mapping of the northern San Francisco Bay region: Implications and findings for Quaternary faulting: U.S. Geological Survey National Earthquake Research Program, Northern California Earthquake Hazards, Research Summaries, FY2005, 2p.

Clark, L.D., 1960, Foothills fault system, western Sierra Nevada, California: Geological Society of America Bulletin, v. 71, p. 483-496.

Cockerham, R.S. and Eaton, J.P., 1987, The earthquake and its aftershocks, April 24 through September 30, 1984, *in* The Morgan Hill Earthquake of April 24, 1984, Hoose, S.A. (ed.): U.S. Geological Survey Bulletin 1639, p. 15-28.

Cornell, C.A., 1968, Engineering seismic risk analysis: Bulletin of the Seismological Society of America, v. 58, p. 1583-1606.

d’Alessio, M.A., I.A. Johanson, R. Bürgmann, D.A. Schmidt, and M.H. Murray. 2005. Slicing up the San Francisco Bay Area: Block kinematics and fault slip rates from GPS-derived surface velocities: Journal of Geophysical Research 110, doi:10.1029/2004JB003496, 19 pp

Division of Safety of Dams (DSOD), 2018, Inspection and Reevaluation Protocols, California Department of Water Resources, Published Date, September 28, 2018.

Dixon, T.H., Miller, M., Farina, F., Wang, H., and Johnson, D., 2000. Present-day motion of the Sierra Nevada block and some tectonic implications for the Basin and Range Province, North American Cordillera: Tectonics, v. 19, p. 1-24.

Du, Y. and Aydin, A., 1992, Three-dimensional characteristics of dike intrusion along the northern Iceland rift from inversion of geodetic data: Tectonophysics, v. 204, p. 111-121.

EBMUD/GEI Consultants, 2013, Supporting Technical Information Document for Pardee Dam.

EPRI/DOE/NRC, 2012, Central and eastern United States seismic source characterization for nuclear facilities: U.S. Nuclear Regulatory Commission Report, NUREG- 2115; EPRI Report 1021097, 6 Volumes; DOE Report# DOE/NE-0140, Washington, D.C.

Federal Energy Regulatory Commission (FERC), 2018, Engineering Guidelines for The Evaluation of Hydropower Projects, Chapter 13 – Evaluation of Earthquake Ground Motions: Division of Dam Safety and Inspections, Office of Energy Projects, Washington DC.

Felzer, K.R., 2008, Calculating California seismicity rates, Appendix I *in* the Uniform California Earthquake Rupture Forecast, version 2: U.S. Geological Survey Open-File Report 2007-1437I.

Field, E.H., Biasi, G.P., Bird, P., Dawson, T.E., Felzer, K.R., Jackson, D.D., Johnson, K.M., Jordan, T.H., Madden, C., Michael, A.J., Milner, K.R., Page, M.T., Parsons, T., Powers, P.M., Shaw, B.E., Thatcher, W.R., Weldon, R.J., II, and Zeng, Y., 2013, Uniform California earthquake rupture forecast, version 3 (UCERF3)—The time-independent model: U.S. Geological Survey Open-File Report 2013–1165, 97 p., California Geological Survey Special Report 228, and Southern California Earthquake Center Publication 1792, http://pubs.usgs.gov/of/2013/1165/.

Frankel, A., 1995, Mapping seismic hazard in the central and eastern United States: Seismological Research Letters, v. 66, p. 8-21.

Frankel, A., C. Mueller, T. Barnard, D. Perkins, E.V. Leyendecker, N. Dickman, S. Hanson, and M. Hopper, 1996. National seismic-hazard maps; documentation June 1996: U.S. Geological Survey Open-File Report 96-532, 110 p.

Graymer, R.W., Bryant, W., McCabe, C.A., Hecker, S., and Prentice, C.S., 2006, Map of Quaternary-active faults in the San Francisco Bay region: U. S. Geological Survey Scientific Investigations Map 2919, one sheet, scale 1:275,000.

Hale, C., Abrahamson, N., Bozorgnia, Y., 2018, Probabilistic seismic hazard analysis code verification: PEER Report 2018/03, Pacific Earthquake Engineering Research Center, University of California, Berkeley, 139 p.

Hammond, W.C. and Thatcher, W., 2007. Crustal deformation across the Sierra Nevada, northern Walker Lane, Basin and Range transition, western United States measured with GPS, 2000-2004. Journal of Geophysical Research-Solid Earth v. 112, B05411, doi: 10.1029/2006JB004625.

Hanks, T.C., and Bakun, W.H., 2014, M-logA models and other curiosities: Bulletin of the Seismological Society of America, v. 104, p. 2604-2610.

Hanks, T.C. and Kanamori, H. 1979, A moment magnitude scale: Journal of Geophysical Research, v. 84, p. 2348-2350.

Hanson, K.L. and Wesling, J.R., 2006, Mapping of the West Napa fault zone for input into the Northern California Quaternary fault database: USGS NEHRP Northern California Earthquake Hazards Research Summaries FY2005: 3rd Annual Northern California Earthquake Hazards Workshop, January 18-19, 2006, Workshop Report, p. 38-39.

Hanson, K.L. and Wesling, J.R., 2007, Mapping of the West Napa fault zone for input into the Northern California Quaternary fault database: USGS NEHRP Northern California Earthquake Hazards Research Summaries FY2006: 3rd Annual Northern California Earthquake Hazards Workshop, January 18-19, 2007, Workshop Report, 2 p.

Hart, E.W., 1981, Pleasanton and related faults (Dublin Quadrangle vicinity): California Division of Mines and Geology Fault Evaluation Report FER-109.

HCG, 1997, Preliminary design report, Volumes VII, Pardee Dam site, Geotechnical and Geological Data report.

Hill, D. P., Eaton, J. P., Ellsworth, W. L., Cockerham, R. S., Lester, F. W., and Corbett, E. J., 1991, The seismotectonic fabric of central California, *in* Slemmons, D. B., Engdahl, E. R., Zoback, M. R., and Blackwell, D. D. (eds.): Neotectonics of North America, Decade of North American Geology: Geological Society of America, p. 107-132.

Idriss, I.M., 2014, An NGA-West2 empirical model for estimating the horizontal spectral values generated by shallow crustal earthquakes: Earthquake Spectra, v. 30, p. 1155-1177.

Irwin, W.P., 1990, Geology and plate tectonic development, in The San Andreas Fault System, California, Wallace, R.E. (ed.), U.S. Geological Survey Professional Paper 1515, p. 61-80.

Jacobs Associates/AMEC/Quest Structures, 2013, Pardee Outlet Tower Seismic Evaluation: unpublished consultant report prepared for EBMUD.

Jennings, C.W., 1994, Fault activity map of California and adjacent areas with locations and ages of recent volcanic eruptions: California Division of Mines and Geology, 1:750,000.

Keefer, D.I. and Bodily, S.E., 1983, Three-point approximations for continuous random variables: Management Science, v. 26, p. 595-609.

Kelson, K.I., 2001, Geologic characterization of the Calaveras fault as a potential seismic source, San Francisco Bay area, California, in Engineering Geology Practice in Northern California, Ferriz, H. and Anderson, R. (eds.), AEG Special Publication 12 / California Geological Survey Bulletin 210, p. 179-192.

LaForge, R. and Ake, J., 1999, Probabilistic seismic hazard analysis: Central Valley Project, Folsom Unit, Mormon Island Auxiliary Dam: U.S. Bureau of Reclamation Seismotectonic Report 94-3, 109 p.

Lahr, K.M., Lahr, J.C., Lindh, A.G., Bufe, C.G. and Lester, F.W., 1976, The August 1975 Oroville earthquakes: Bulletin of the Seismological Society of America. Vol. 66, pp. 1085-1099.

LCI, 2020, Pardee Dam – Foothills Fault System Study, Amador and Calaveras Counties, CA: unpublished report prepared for East Bay Municipal Utility District.

Lienkaemper, J.J., 2012, Recently active traces of the Berryessa section and adjacent sections of the Green Valley Fault Zone, California: A Digital Database: U.S. Geological Survey Data Series 710, 12 p.

Lienkaemper, J. and Brown, J., 2009, Preliminary investigation of factors affecting the seismic potential of the Bartlett Springs fault zone, northern California: American Geophysical Union, Fall Meeting 2009, abstract #S51B-1403

Lienkaemper, J.J., J.N. Baldwin, R. Turner, R.R. Sickler, and J. Brown. 2013. A record of large earthquakes during the past two millennia on the Southern Green Valley fault, California: Bulletin of the Seismological Society of America, Vol. 103, No. 4, pp. 2386-2403.

Lienkaemper, J. J., 2010, Recently active traces of the Bartlett Springs Fault, California; a digital database: U.S. Geological Survey Data Series 541, 10 p. and data.

Lienkaemper, J.J. and Galehouse, J.S., 1997, Revised long-term creep rates on the Hayward fault, Alameda and Contra Costa Counties, California: U.S. Geological Survey Open-File Report 97-690, 18 p.

Lienkaemper, J.J. Schwartz, D.P., Kelson, K.I., Lettis, W.R., Simpson, G.D., Southon, J.R. Wanket, J.A., Williams, P.L., 1999, Timing of paleoearthquakes on the northern Hayward fault – preliminary evidence in El Cerrito, California: U.S. Geological Survey Open-File Report 99-318, p. 34.

Lienkaemper, J.J., 1992, Map of recently active traces of the Hayward fault, Alameda and Contra Costa counties, California: U.S. Geological Survey Miscellaneous Field Studies Map MF-2196, 1:24,000.

Minster J. B. and Jordan, T. H., 1987, Vector constraints on western U. S. deformation from space geodesy; Neotectonics and plate motion: Journal of Geophysical Research, v. 92, p. 4798-4804

Molnar, P., 1979, Earthquake recurrence intervals and plate tectonics: Bulletin of the Seismological Society of America, v. 69, p. 115-133.

O'Connell, D.R.H., Unruh, J.R., and Block, L.V., 2001, Source characterization and ground-motion modeling of the 1892 Vacaville-Winters earthquake sequence, California: Bulletin of the Seismological Society of America, v. 91, p. 1471-1497

Oppenheimer, D. H., and Lindh, A. G., 1992, The potential for earthquake rupture of the northern Calaveras fault, *in* Proceedings of the Second Conference on Earthquake Hazards in the Eastern San Francisco Bay Area, California Division of Mines and Geology Special Publication, v. 113, p. 233– 240.

Oppenheimer, D.H. and Macgregor-Scott, N., 1992, The seismotectonics of the eastern San Francisco Bay region, *in* Proceedings of the Second Conference on Earthquake Hazards in the Eastern San Francisco Bay Area, Borchardt, G., Hirschfeld, S.E., Lienkaemper, J.J., McClellan, P., Williams, P.L. and Wong, I.G. (eds.), California Division of Mines and Geology Special Publication 113, p. 11-16.

Oppenheimer, D.H., Bakun, W.H., and Lindh, A.G., 1990, Slip partitioning of the Calaveras fault, California, and prospects for future earthquakes: Journal of Geophysical Research, v. 95, p. 8483-8498.

Pacific Gas and Electric Company (PG&E), 1994, Characterization of potential earthquake sources for Ralston Afterbay Dam: FERC Project No. 2079, State Dam No. 1030-4.

Page, B.M., 1982, The Calaveras fault zone of California—An active pl. boundary element, *in* Hart, E.W., Hirschfeld, S.E., and Schulz, S.S., eds., Proceedings of Conference on Earthquake Hazards in the Eastern San Francisco Bay Area: California Department of Conservation, Division of Mines and Geology Special Publication 62, p. 175-184.

Page, W.D. and Sawyer, T.L., 2001, Use of geomorphic profiling to identify Quaternary faults within the northern and central Sierra Nevada, California: Association of Engineering Geologists Special Volume, "Engineering Geology Practice in Northern California", Ferriz, H. and Anderson, R. (eds.), p. 275-293.

Page, W.D. and Sawyer, T.L., 2007, Overview of late Cenozoic faulting in the Sierra Nevada foothills (including a reassessment of faults near New Bullards Bar Dam): unpublished consulting report prepared by Pacific Gas & Electric and Piedmont GeoSciences, Inc.

Petersen, M.D., Shumway, A.M., Powers, P.M., Mueller, C.S., Moschetti, M.P., Frankel, A.D, Rezaeian, S., McNamara, D.E., Luco, N., Boyd, O.S., Rukstales, K.S., Jaiswal, K.S., Thompson, E.M., Hoover., S.M., Clayton, B.S., Field, E.H. and Zeng, Y., 2020, The 2018 update of the US National Seismic Hazard Model: Overview of model and implications: Earthquake Spectra, v. 36, p. 5-41.

Rizzo, 2018,.Eighth FERC part 12D Independent consultant safety inspection, Camanche Dam and hydroelectric facility: FERC Project No. 2916-CA, State Dam No. 31-016|NATDAM No. CA00173

Rogers, J.D. and Halliday, J.M., 1992, Exploring the Calaveras-Las Trampas fault junction in the Danville-San Ramon area, *in* Proceedings of the Second Conference on Earthquake Hazards in the Eastern San Francisco Bay Area, Borchardt, G., Hirschfeld, S.E., Lienkaemper, J.J., McClellan, P., Williams, P.L. and Wong, I.G. (eds.), California Department of Conservation, Division of Mines and Geology, p. 261-270.

Saucedo, G.J., Bedford, D.R., Raines, G.L., Miller, R.J., and Wentworth, C.M., 2000, GIS data for the geologic map of California: California Department of Conservation, California Geological Survey

Schaff, D.P., Bokelmann, G.H.R., Beroza, G.C., Waldhauser, F. and Ellsworth, W.L., 2002, High-resolution image of Calaveras fault seismicity: Journal of Geophysical Research, v. 107, p. ESE 5 1-16.

Schwartz, D. P., Swan, F. H., III, Harpster, R. E., Rogers, T. H., and Hitchcock, D. E., 1977, Surface faulting potential, Earthquake evaluation studies of the Auburn dam area: Woodward-Clyde Consultants Report for U. S. Bureau of Reclamation, v. 2, 135 p.

Schwartz, D.P. and Coppersmith, K.J., 1984, Fault behavior and characteristic earthquakes--examples from the Wasatch and San Andreas fault zones: Journal of Geophysical Research, v. 89, p. 5681-5698.

Schwartz, D.P., Joyner, W.B., Stein, R.S., Brown, R.D., McGarr, A.F., Hickman, S.H., and Bakun, W.H., 1996, Review of seismic-hazard issues associated with the Auburn Dam Project, Sierra Nevada foothills, California: U.S. Geological Survey Open-File Report 96-11.

Shahi, S.K. and Baker, J.W., 2014, NGA-West2 Models for ground motion directionality: Earthquake Spectra, v. 30, p. 1285-1300.

Somerville, P.G., Smith, N.F., Graves, R.W., and Abrahamson, N.A., 1997, Modification of empirical strong ground motion attenuation relations to include the amplitude and duration effects of rupture directivity: Seismological Research Letters, v. 68, p. 199-222.

Sowers, J.M., Noller, J.S., and Unruh, J.R., 1992, Quaternary deformation and blind thrusting on the east front of the Diablo Range near Tracy: Proceedings of the Second Conference on Earthquake Hazards in the Eastern San Francisco Bay Area: California Division of Mines and Geology Special Publication 113, p. 377-384.

Spudich, P., Bayless, J.R., Baker, J.W., Chiou, B.S.J., Rowshandel, B., Shahl, S.K., and Somerville, P., 2013, Final Report of the NGA-West2 Directivity Working Group: PEER Report No. 2013/09, Pacific Earthquake Engineering Research Center, University of California, Berkeley, CA.

Sterling, R. 1992. Intersection of the Stockton and Vernalis faults, southern Sacramento Valley, California. In Structural Geology of the Sacramento Basin, V.B. Chervon and W.F. Edmondson, eds., pp. 143-151. American Association of Petroleum Geologists Miscellaneous Publication 41, Pacific Section.

Stover, C.W. and Coffman, J.L., 1993, Seismicity of the United States, 1568-1989 (Revised):U.S. Geological Survey Professional Paper 1527, 415 p.

Svarc, J.L, Savage, J.C., Prescott, W.H., and Ramelli, A.R., 2002. Strain accumulation and rotation in western Nevada, 1993-2000: Journal of Geophysical Research, v. 107, p. ETC 2-1 – ETG 2-13.

Terra/GeoPentech, 2010, Camanche Embankment Safety Review, Summary Report: unpublished report prepared for East Bay Municipal Utility District.

Thatcher, W., Foulger, G.R., Julian, B.R., Svarc, J., Quilty, E., and Bawden, G.W., 1999. Present-day deformation across the Basin and Range Province, western United States: Science, v. 283, p. 1714-1718Toppozada, T.R. and Borchardt, G., 1998, Re-evaluation of the 1836 "Hayward fault" and 1838 San Andreas fault earthquakes: Bulletin of the Seismological Society of America, v. 88, p. 140-159.

Thrust Fault Subgroup. 1999. Thrust faults as seismic sources in the San Francisco Bay Area: report submitted to the Working Group on Northern California Earthquake Probabilities

Toppozada, T.R. and Borchardt, G., 1998, Re-evaluation of the 1836 "Hayward fault" and 1838 San Andreas fault earthquakes: Bulletin of the Seismological Society of America, v. 88, p. 140-159.

U.S. Geological Survey (USGS) *and California Geological Survey, Quaternary fault and fold database for the United States: https://www.usgs.gov/natural-hazards/earthquake-hazards/faults.*

Unruh, J.R., and Hitchcock, C.S., 2009, Characterization of Potential Seismic Sources in the Sacramento-San Joaquin Delta, California: Final Technical Report submitted to the U.S. Geological Survey National Earthquake Hazard Reduction Program, Award Number 08HQGR0055, 45 p

Unruh, J.R., and Hitchcock, C.S., 2015, Detailed mapping and analysis of fold deformation above the West Tracy Fault, southern San Joaquin-Sacramento Delta, northern California: Collaborative research with Lettis Consultants and InfraTerra: Final technical report: U.S. Geological Survey National Earthquake Hazards Reduction Program Award Number G14AP00069, 46 p

Unruh, J.R., and Sawyer, T.L., 1998, Paleoseismic investigation of the northern Greenville fault, eastern San Francisco Bay Area, California: U.S. Geological Survey Final Technical Report for the National Earthquake Hazards Reduction Program, Award # 1434-HQ-97-GR-03146, 34 p

Unruh, J. and J. Humphrey, 2017. Seismogenic deformation between the Sierran microplate and Oregon Coast block, California, USA: Geology, v.45, p.415-418.

Unruh, J.R. and Lettis, W.R., 1998, Kinematics of transpressional deformation in the eastern San Francisco Bay region, California: Geology, v. 26, p. 19-22.

Unruh, J.R. and Moores, E.M., 1992, Quaternary blind thrusting on the southwestern Sacramento Valley, California: Tectonics, v. 11, p. 192-203.

URS Corporation/Jack R. Benjamin & Associates, 2008, Delta risk management strategy (DRMS), Phase 1 Draft 2, Topical Area Seismology: technical memorandum prepared for California Department of Water Resources.

U.S. Army Corps of Engineers, 1995, Geologic and Seismologic Investigation (Fault Study), New Hogan Dam and Reservoir (New Hogan Lake), Calaveras River, California.

Wakabayashi, J. and Smith, D.L., 1994, Evaluation of recurrence intervals, characteristic earthquakes, and slip rates associated with thrusting along the Coast Range-Central Valley geomorphic boundary, California: Bulletin of the Seismological Society of America, v. 84, p. 1960-1970.

Wallace, R.E., 1990, The San Andreas Fault System, California: U.S. Geological Survey Professional Paper 1515, 283 p.

Weber-Band, J. 1998. Neotectonics of the Sacramento–San Joaquin Delta area, east-central Coast Ranges, California. Unpublished Ph.D., University of California, Berkeley, 216 pp.

Weichert, D.H., 1980, Estimation of the earthquake recurrence parameters for unequal observation periods for different magnitudes: Bulletin of the Seismological Society of America, v. 70, p. 1337-1346.

Wells, D.L. and Coppersmith, K.J., 1994, New empirical relationships among magnitude, rupture length, rupture width, rupture area, and surface displacement: Bulletin of the Seismological Society of America, v. 84, p. 974-1002.

Wentworth, C. W., and M. D. Zoback, 1990, Structure of the Coalinga area and thrust origin of the earthquake, in The Coalinga, California, Earthquake of May 2, 1983, edited by M. J. Rymer, and W. L. Ellsworth, U.S. Geol. Surv. Prof. Pap., 1487, 41–68.

Wesnousky, S.G., 1986, Earthquakes, Quaternary faults, and seismic hazard in California: Journal of Geophysical Research, v. 91, p. 12,587-12,631.

WGCEP (Working Group for California Earthquake Probabilities), 2008, The uniform earthquake rupture forecast, version 2 (UCERF2): U.S. Geological Survey Open-File Report 2007-1437.

Wong, I.G. and Ely, R.W., 1983, Historical seismicity and tectonics of the Coast Ranges-Sierra block boundary: Implications to the 1983 Coalinga earthquakes; *in* Bennet, J. and Sherburne, R. (eds.), The 1983 Coalinga, California Earthquakes: California Division of Mines and Geology Special Publication 66, p. 89-104

Wong, I.G., Ely, R.W., and Kollman, A.C., 1988, Contemporary seismicity and tectonics of the northern and central Coast Ranges-Sierran block boundary zone, California: Journal of Geophysical Research, v. 93, p. 7813-7833.

Woodward-Clyde Consultants, 1978, Foothills fault system study: Appendix C.4 of volume 6, Stanislaus Nuclear Project, Site Suitability-Site Safety Report: Report to the Pacific Gas and Electric Company, 166 p.

Youngs, R.R. and Coppersmith, K.J., 1985, Implications of fault slip rates and earthquake recurrence models to probabilistic seismic hazard estimates: Bulletin of the Seismological Society of America, v. 75, p. 939-964

Youngs, R.R., K.J. Coppersmith, C.L. Taylor, M.S. Power, L.A. Di Silvestro, M.L. Angell, N.T. Hall, J.R. Wesling, and L. Mualchin. 1992. A comprehensive seismic hazard model for the San Francisco Bay Region, *in* Proceedings of the Second Conference on Earthquake Hazards in the Eastern San Francisco Bay Area, Borchardt, G., S.E. Hirschfeld, J.J. Lienkaemper, P. McClellan, P.L. Williams, and I.G. Wong.(eds.), California Division of Mines and Geology Special Publication 113, pp. 431-441.

Youngs, R.R., Swan, F.H., Power, M.S., Schwartz, D.P., and Green, R.K., 2000, Probabilistic analysis of earthquake ground shaking hazard along the Wasatch Front, Utah, *in* P.L. Gori and W.W. Hays (eds.), Assessment of Regional Earthquake Hazards and Risk Along the Wasatch Front, Utah: U.S. Geological Survey Professional Paper 1500-K-R, p. M1-M74.

Appendix A Fault Tables

Table A1. Source Parameters for Foothills Fault System

Fault	Probability of Activity	Rupture Scenario	Rupture Length (km)	Seismogenic Depth (km)	Dip[1] (deg.)	Fault Type / Sense of Slip	Magnitude	Slip Rate[2] (mm/yr)	Approximate Age of Youngest Offset	Notes
Sierran Foothills fault system	1.0	Floating earthquake (0.2)		10 (0.3) 15 (0.4) 20 (0.3)	N: 45 W (0.3) 55 W (0.4) 65 W (0.3)	Normal (0.4)	6.2 (0.3) 6.5 (0.4) 6.8 (0.3)	N: 0.018 (0.2) 0.030 (0.6) 0.044 (0.2)		We have adopted the segments of the Foothills fault system is described in LCI (2020), with additional segments with documented or suspected late Quaternary activity as described in Anderson and Ake (2008). We also include a floating earthquake version. The geometry follows the Quaternary faults shown in Saucedo et al.(2000), with a "floating earthquake", based on a surface rupture length of 20 km and a depth of 15 km. Under the normal branch of the model, slip is assumed to be dominantly normal. Under the Dextral-oblique branch of the model, slip is assumed have a significant right-lateral strike slip component (Anderson and Ake, 2008).
		East Branch (0.9)	20		DO: 65 W (0.3) 75 W (0.4) 85 W (0.3)	Dextral-Oblique(0.6)		DO: 0.030 (0.2) 0.044 (0.6) 0.090 (0.2)		
		West Branch (0.1)	20				6.2 (0.3) 6.5 (0.4) 6.8 (0.3)			
		Individual Segments (0.8)								
	1.0	Mormon Island	26	10 (0.3) 15 (0.4) 20 (0.3)	Same as above	Same as above	6.4 (0.3) 6.7 (0.4) 7.0 (0.3)	N: 0.003 (0.2) 0.004 (0.6) 0.006 (0.2) DO: 0.004 (0.2) 0.013 (0.6) 0.007 (0.2)	Late Cenozoic ?	
	1.0	West Branch-Bear Mtn	30	10 (0.3) 15 (0.4) 20 (0.3)			6.5 (0.3) 6.8 (0.4) 7.1 (0.3)	N: 0.003 (0.2) 0.004 (0.6) 0.006 (0.2) DO: 0.004 (0.2) 0.013 (0.6) 0.007 (0.2)	Late Cenozoic ?	
	1.0	Hancock Creek	21	10 (0.3) 15 (0.4) 20 (0.3)			6.3 (0.3) 6.6 (0.4) 6.9 (0.3)	N: 0.003 (0.2) 0.004 (0.6) 0.006 (0.2) DO: 0.004 (0.2) 0.013 (0.6) 0.007 (0.2))	Late Cenozoic ?	
	1.0	Waters Peak -	62	10 (0.3) 15 (0.4)	50 NE (0.3) 65 NE (0.4)		6.0 (0.3) 6.4 (0.4)	0.004 (0.3) 0.010 (0.4)		

Fault	Probability of Activity	Rupture Scenario	Rupture Length (km)	Seismogenic Depth (km)	Dip[1] (deg.)	Fault Type / Sense of Slip	Magnitude	Slip Rate[2] (mm/yr)	Approximate Age of Youngest Offset	Notes
		Green Springs Run		20 (0.3)	80 NE (0.3)		7.0 (0.3)	0.045 (0.3)		
	0.5	Devils Gate	39	6 (0.3) 10 (0.4) 15 (0.3)	60 SW (0.3) 75 SW (0.4) 90 (0.3)		5.8 (0.3) 6.0 (0.4) 6.5 (0.3)	0.002 (0.3) 0.020 (0.4) 0.050 (0.3)		
	0.5	Ione	20	10 (0.3) 15 (0.4) 20 (0.3)	60 SW (0.3) 75 SW (0.4) 90 (0.3)		6.0 (0.3) 6.2 (0.4) 6.5 (0.3)	0.002 (0.3) 0.030 (0.4) 0.010 (0.3)		
	1.0	Youngs Creek - Bowie Flat	64	10 (0.3) 15 (0.4) 20 (0.3)	55 NE (0.3) 70 NE (0.4) 85 NE (0.3)		6.0 (0.3) 6.4 (0.4) 7.0 (0.3)	0.001 (0.3) 0.002 (0.4) 0.008 (0.3)		
	0.2	Haupt Creek	17	10 (0.3) 15 (0.4) 20 (0.3)	55 NE (0.3) 70 NE (0.4) 85 NE (0.3)		6.0 (0.3) 6.2 (0.4) 6.4 (0.3)	0.00003 (0.3) 0.0006 (0.4) 0.005 (0.3)		
	1.0	Poorman Gulch - Rawhide Flat	61	10 (0.3) 15 (0.4) 20 (0.3)	55 NE (0.3) 70 NE (0.4) 85 NE (0.3)		6.0 (0.3) 6.4 (0.4) 7.0 (0.3)	0.002 (0.3) 0.009 (0.4) 0.050 (0.3)		
	0.2	Slate Creek	34	10 (0.3) 15 (0.4) 20 (0.3)	55 NE (0.3) 70 NE (0.4) 85 NE (0.3)		6.0 (0.3) 6.2 (0.4) 6.6 (0.3)	0.0005 (0.3) 0.010 (0.4) 0.050 (0.3)		

[1] Inclination of fault plane, measured from the horizontal.
[2] N – normal, DO – Dextral-Oblique

Table A2. Source Parameters for Bay Area Faults Included in the Hazard Analysis

Fault Name	Probability of Activity[1]	Rupture Scenario[2]	Segment Name	Rupture Length (km)	Depth[3] (km)	Dip[4] (deg)	Sense of Slip[5]	Characteristic Magnitude[6]	Slip Rate (mm/yr) or Recurrenece Interval[7] (yrs)	Notes
San Andreas (Northern and Central)	1.0	Unsegmented (0.5)	1906	464	13 ± 3	90	SS	8.0	24 ± 3	Characterization based on WGCEP (2008) and Field et al. (2013). Unsegmented rupture scenario is a repeat of the 1906 **M** 7.9 San Francisco earthquake.
		Two Segments (0.15)	Offshore + North Coast	301	11 ± 2	90	SS	7.7	24 ± 3	
			Peninsula + Santa Cruz Mountains	163	13 ± 2	90	SS	7.5	17 ± 4	
		Three Segments (0.15)	Offshore + North Coast	301	11 ± 2	90	SS	7.7	24 ± 3	
			Peninsula	100	13 ± 2	90	SS	7.3	17 ± 4	
			Santa Cruz Mountains	63	15 ± 2	90	SS	7.1	17 ± 4	
		Floating Earthquake (0.2)	N/A	N/A	13 ± 3	90	SS	6.9	24 ± 3	
Calaveras	1.0	Unsegmented (0.05)	Northern + Central + Southern Calaveras+Paicines	180	12 ± 2	90	SS	7.4	4 (0.2) 6 (0.4) 15 (0.3) 20 (0.1)	Characterization of WGCEP (2008) modified by recent paleoseismic data of Kelson (written communication, 2006).
		Three Segments (0.05)	Northern Calaveras	48	13 ± 2	90	SS	6.8	6 ± 2	
			South + Central Calaveras	79	11 ± 2	90	SS	6.5	15 ± 3	
			Paicines	60	13 ± 2	90 ± 15	SS	7.1	12 ± 3	
		Four Segments (0.2)	Northern Calaveras	48	13 ± 2	90	SS	6.8	6 ± 2	
			Central Calaveras	52	11 ± 2	90	SS	6.5	15 ± 3	
			Southern Calaveras	26	11 ± 2	90	SS	5.8	15 ± 3	
			Paicines	60	13 ± 2	90 ± 15	SS	7.1	12 ± 3	
		Segment + Floating Earthquake (0.3)	Northern Calaveras	48	13 ± 2	90	SS	6.8	6 ± 2	
			Floating Earthquake on Central + South Calaveras	N/A	11 ± 2	90	SS	6.2	15 ± 3	
			Paicines	60	13 ± 2	90 ± 15	SS	7.1	12 ± 3	
		Floating Earthquake (0.4)	N/A	N/A	11 ± 2	90	SS	6.2	4 (0.2) 6 (0.4) 15 (0.3) 20 (0.1)	
Hayward – Rodgers Creek	1.0	Unsegmented (0.05)	Hayward + Rodgers Creek-Healdsburg	185	12 ± 2	90	SS	7.5	9 ± 2	Characterization based on WGCEP (2008) model. Recurrence intervals from Field et al (2013).
		Two Segment (A) (0.1)	North Hayward + Rodgers Creek-Healdsburg	131	12 ± 2	90	SS	7.4	9 ± 2	
			Southern Hayward	54	12 ± 2	90	SS	6.9	**SR (0.2)** 9 ± 2 **RI (0.8)** 129 (0.2) 168 (0.6) 217 (0.2)	
		Two Segment (B) (0.3)	Rodgers Creek-Healdsburg	82	12 ± 2	90	SS	7.1	**SR (0.2)** 9 ± 2 **RI (0.8)** 135 (0.2) 325 (0.6) 785 (0.2)	
			Hayward	107	12 ± 2	90	SS	7.2	9 ± 2	

Fault Name	Probability of Activity[1]	Rupture Scenario[2]	Segment Name	Rupture Length (km)	Depth[3] (km)	Dip[4] (deg)	Sense of Slip[5]	Characteristic Magnitude[6]	Slip Rate (mm/yr) or Recurrenece Interval[7] (yrs)	Notes
		Three Segment (0.5)	Rodgers Creek-Healdsburg	82	12 ± 2	90	SS	7.1	**SR (0.2)** 9 ± 2 **RI (0.8)** 180 (0.2) 230 (0.6) 300 (0.2)	
			North Hayward	53	12 ± 2	90	SS	6.9	**SR (0.5)** 9 ± 2 **RI (0.5)** 206 (0.2) 318 (0.6) 492 (0.2)	
			Southern Hayward	54	12 ± 2	90	SS	6.9	**SR (0.2)** 9 ± 2 **RI (0.8)** 175 (0.2) 211 (0.6) 270 (0.2)	
		Floating Earthquake (0.05)	N/A	N/A	12 ± 2	90	SS	6.9	9 ± 2	
Green Valley (GVF)-Berryessa (BF)-Hunting Creek (HCF) system	1.0	Model 1: HCF not included (0.5)								Characterization based on mapping by J. Lienkameper, documented in Lienkaemper (2010) and Lienkaemper (2012), and on Field et al., (2013). Changes from earlier (WGCEP, 2008 and prior) models, include combining Concord and Green Valley faults into a single Green Valley fault and including the Berryessa fault in the Green Valley fault system. Finally, the Hunting Creek fault serves as a "fuse" between GVF and the Bartlett Springs fault to the north; it can rupture with either system but tends to impede throughgoing rupture involving both faults (Lienkaemper and Brown, 2009; J. Lienkaemper, pers. comm., 2012). Thus, in this model, HCF is only included in the GVF system half the time. Rupture lengths are from Lienkaemper mapping.
		Unsegmented (0.3)	GVF+BF	94	13 ± 3	90	SS	7.0	5 ± 3	
		Segmented (0.7)	GVF	74	13 ± 3			6.9	5 ± 3	
			BF	22	13 ± 3			6.5	5 ± 3	
		Model 2: HCF included (0.5)								
		Unsegmented (0.1)	GVF+BF+HCF	126	13 ± 3	90	SS	7.3	5 ± 3	
		Two Segments (0.2)	GVF	74	13 ± 3	90	SS	6.9	5 ± 3	
			BF+HCF	50	13 ± 3	90	SS	7.0	5 ± 3	
		Two Segments (0.2)	GVF+BF	94	13 ± 3	90	SS	7.0	5 ± 3	
			HCF	32	13 ± 3	90	SS	6.7	5 ± 3	
		Three Segments (0.5)	GVF	74	13 ± 3	90	SS	6.9	5 ± 3	
			BF	22	13 ± 3	90	SS	6.5	5 ± 3	
			HCF	32	13 ± 3	90	SS	6.7	5 ± 3	
Greenville **Model 1 (0.8): Adopts Unruh and Sawyer (1998) and Lienkaemper et al. (2013) fault length**	1.0	Unsegmented (1.0)	N/A	57	15 ± 3	90	SS	6.9	1 (0.2) 2 (0.6) 3 (0.2)	Model assumes that slip on the Greenville fault primarily is derived from Ortigalita fault (up to about 2.5 mm/yr) via left-stepover across the Mt. Oso anticline. Model assumes that most if not all of the Greenville fault slip is transferred to the Concord fault across Mt. Diablo anticline. Fault length of 57 km measured from west end of Mt. Oso anticline to latitude of epicenter of 1980 Livermore earthquake (SE end of Mt. Diablo anticline). Holocene slip rate of about 2 mm/yr on northern segment of fault reported by Berger et al. (2010) applies only to the main trace of the fault and is assumed to be a minimum rate for the entire zone because there is a second, unstudied splay to the east at the latitude of Livermore Valley.
Model 2 (0.2): Adopts UCERF3 fault length (Field et al. 2013)		Unsegmented –Floating (0.2)	N/A	80	15 ± 3	90	SS	6.5 (0.2) 6.8 (0.6) 7.1 (0.2)	0.7 (0.2) 1.5 (0.6) 2.3 (0.5)	Model adopts 80-km-long fault geometry of the UCERF3 model (Field et al. 2013). Northern segment of the fault extends north of the 1980 Livermore earthquake epicenter and apparently includes the trace of the late Cretaceous-early Tertiary Clayton fault. The southern segment of the model fault source continues south of Mt. Oso anticline and includes traces of the Greenville fault in San Antonio
		Segmented (0.8)	Northern	51	15 ± 3	90	SS	6.8	1 (0.2) 2 (0.6) 3 (0.2)	

Fault Name	Probability of Activity[1]	Rupture Scenario[2]	Segment Name	Rupture Length (km)	Depth[3] (km)	Dip[4] (deg)	Sense of Slip[5]	Characteristic Magnitude[6]	Slip Rate (mm/yr) or Recurrenece Interval[7] (yrs)	Notes
			Southern	29	15 ± 3	90	SS	6.7	0.1 (0.2) 0.5 (0.6) 1.0 (0.2)	Valley that have poor geomorphic expression and appear to be significantly less active than the northern segment. Late Quaternary slip rate for the southern segment is not known; the distribution on slip rate was adopted to span an order of magnitude below that of the northern segment. Slip rate for floating EQ based on moment balance with segmented model.
Quinto Fault (GV 8)	1.0	Unsegmented (1.0)	N/A	19.4	6	25 W	R	6.6	0.4 (0.2) 0.5 (0.6) 0.6 (0.2)	Based on characterization of Field et al. (2013)
Southern Midland	0.9	Unsegmented (0.1)	N/A	30	top: 1.0 bottom:1 5 ± 5	60 W (0.5) 70 W (0.5)	RO	6.7	0.02 (0.2) 0.06 (0.6) 0.2 (0.2)	Activity and rate is inferred from displacement of late Tertiary (and possibly early Pleistocene) strata in seismic reflection profiles (Weber-Band, 1998) and displacement of basal peat (Holocene) inferred from analysis of Atwater (1982) data (URS/JRB, 2008) and examined in Unruh and Hitchcock (2009). Unruh and Hitchcock preferred slip rate is 0.4±0.2 mm/yr. URS/JRB (2008) considered a rate of 1.0 mm/yr with 0.3 weight to allow for possible dextral slip. Unruh and Hitchcock (2009) consider dextral slip to be minor, so we include the 1.0 mm/yr rate with lower weight. Tip of fault is inferred by CDOG (1982) to extend above the base of the Tertiary Markley Formation to depths of about 1.0 km, and possibly shallower. Minimum fault depth not constrained by data in CDOG (1982).
		Floating Earthquake (0.9)	N/A	N/A	top: 1.0 bottom:1 5 ± 5	60 W (0.5) 70 W (0.5)	RO	6.0 (0.3) 6.25 (0.4) 6.5 (0.3)	0.02 (0.2) 0.06 (0.6) 0.2 (0.2)	
Midway/ Black Butte	1.0	Floating Earthquake (1.0)	N/A	31	14 ± 3	70 W ± 10	RO	6.25 (0.2) 6.5 (0.4) 6.75 (0.4)	0.1 (0.3) 0.5 (0.4) 1.0 (0.3)	The Black Butte fault is a documented late Quaternary-active reverse (oblique?) fault (Sowers et al., 1992) that appears to be related to the late Cenozoic dextral Midway fault by a short left-restraining bend. Limited data are available on slip rate and rupture behavior. The slip rate estimate is based on uplift of middle to early Pleistocene pediment surface across the Black Butte fault (Sowers et al., 1992) and an inferred H:V ratio for the components of slip of ≤ 3:1.
Mt Diablo	1.0	Unsegmented (0.5)	N/A	31	top: 5 (0.5); 1 (0.5) bottom: 16	30 NE (0.2) 45 NE (0.6) 50 NE (0.2)	R	6.8	1.0 (0.2) 3.0 (0.6) 5.0 (0.2)	Characterization from Unruh (personal communication, 2006). Fault tip inferred to approach within 5 km (0.5) to 1 km (0.5) of the surface based on restorable cross section, and on map-scale relationships between surface faults and fold axis.
		Segmented (0.5)	Mt. Diablo North	12	top: 4 (0.5); 2 (0.5) bottom: 16	30 NE (0.2) 45 NE (0.6) 50 NE (0.2)	R	6.4	1.0 (0.2) 3.0 (0.6) 5.0 (0.2)	North: Fault tip inferred to approach within 4 km (0.5) to 2 km (0.5) of the surface based on model in restorable cross section.
			Mt. Diablo South	19	top: 5 (0.5); 1 (0.5) bottom: 16	30 NE (0.2) 45 NE (0.6) 50 NE (0.2)	R	6.6	1.0 (0.2) 3.0 (0.6) 5.0 (0.2)	South: Fault tip inferred to approach within 5 km (0.5) to 1 km (0.5) of the surface based on model in restorable cross section, and map-scale relationships between surface faults and fold axis.

Fault Name	Probability of Activity[1]	Rupture Scenario[2]	Segment Name	Rupture Length (km)	Depth[3] (km)	Dip[4] (deg)	Sense of Slip[5]	Characteristic Magnitude[6]	Slip Rate (mm/yr) or Recurrenece Interval[7] (yrs)	Notes
Mt. Oso	0.7	Unsegmented (1.0)	N/A	25	15 ± 2	45 ± 15 NE	R	6.7	0.5 (0.2) 1.5 (0.6) 2.5 (0.2)	Inferred thrust fault occupying the contractional stepover between the Ortigalita and Greenville faults. NE-dipping rupture geometry inferred from the SW-vergence of the Mt. Oso anticline and analogy to Mt. Diablo thrust (J. Unruh, Wm. Lettis and Associates, *Pers. Comm.*, 2006). Activity based on slip transfer from the northern Ortigalita to the southern Greenville. Fault tip at 5 km depth
Ortigalita	1.0	Segmented (0.3)	Northern Ortigalita	40	15 ± 3	90	SS	6.9	0.5 (0.15) 1.0 (0.35) 2.0 (0.35) 2.5 (0.15)	Characterization revised from Cao et al. (2003) using mapping and paleoseismic data from Anderson and Piety (2001) to modify the lengths and slip rates for the north and south segments of the fault. They estimate a slip rate of 1.0-2.0 mm/yr for the northern section based on abundant geomorphic evidence for probable latest Pleistocene and Holocene displacement and, paleoseismic trench investigations that indicate that Quaternary deposits estimated to be between 10 ka and 25 ka, are right laterally offset between about 13 and 25 m by the Cottonwood Arm segment of the Ortigalita fault. They note the southern segment appears much less active and accordingly, they assign a lower slip rate of 0.2 to 1.0 mm/yr to this segment.
			Southern Ortigalita	60	15 ± 3	90	SS	7.1	0.2 (0.2) 0.6 (0.6) 1.0 (0.2)	
		Segmented + Floating Earthquake (0.7)	Northern Ortigalita	40	15 ± 3	90	SS	6.9	0.5 (0.15) 1.0 (0.35) 2.0 (0.35) 2.5 (0.15)	
			Floating Earthquake on Southern Ortigalita	60	15 ± 3	90	SS	6.6	0.2 (0.2) 0.6 (0.6) 1.0 (0.2)	
Pittsburgh-Kirby Hills	1.0	Unsegmented (0.4)	N/A	28	20 ± 5	80 E ± 10	SS	6.9	0.3 (0.4) 0.5 (0.4) 0.7 (0.2)	Characterization from the Thrust Fault Subgroup of the 1999 Working Group.
		Floating Earthquake (0.6)	N/A	N/A	20 ± 5	80 E ± 10	SS	6.3	0.3 (0.4) 0.5 (0.4) 0.7 (0.2)	
West Napa	1.0	Unsegmented (0.15)	St. Helena/Dry Creek + West Napa	52	15 ± 3	90	SS	7.0	1.0 (0.3) 2.0 (0.3) 3.0 (0.3) 4.0 (0.1)	Characterization is based on compilation and mapping of the West Napa fault by Hanson and Wesling (2006 and 2007) and Clahan et al. (2005) conducted in support of the USGS Quaternary fault database for Northern California (Graymer et al., 2006). The slip rate for the West Napa is not well constrained, but was previously considered to be on the order of 1 mm/yr (1 ± 1 mm/yr, Cao et al., 2003). Several recent studies and observations suggest the slip rate is higher. These include: 1) more detailed mapping of the fault zone (Hanson and Wesling, 2006, 2007) that shows that the fault is better expressed geomorphically than had been recognized previously with evidence for recent (< 600 to 700 years B. P.) displacement; 2) comparison of slip budgets between the regions north and south of Carquinez Strait suggests that a significant amount of slip is being transferred from the North Calaveras fault to the West Napa fault via the Cull Canyon/Laffette/Reliz Valley fault zone; and 3) a recent analysis of GPS data with the preferred model indicating a rate of 4 ± 3 mm/yr (d'Alessio et al., 2005).
		Floating Earthquake (0.35)	N/A	N/A	15 ± 3	90	SS	6.5	0.5 (0.1) 1.0 (0.3) 2.0 (0.3) 3.0 (0.2) 4.0 (0.1)	
		Segmented (0.15)	St. Helena/Dry Creek	24	15 ± 3	90	SS	6.7	0.5 (0.2) 1.0 (0.5) 2.0 (0.2) 3.0 (0.1)	
			West Napa	38	15 ± 3	90	SS	6.9	0.5 (0.2) 1.0 (0.5) 2.0 (0.2) 3.0 (0.1)	
		Segmented + Floating Earthquake (0.35)	Floating Earthquake on West Napa	N/A	15 ± 3	90	SS	6.4	0.5 (0.2) 1.0 (0.5) 2.0 (0.2) 3.0 (0.1)	
			St. Helena/Dry Creek	24	15 ± 3	90	SS	6.7	0.5 (0.2) 1.0 (0.5) 2.0 (0.2) 3.0 (0.1)	

Fault Name	Probability of Activity[1]	Rupture Scenario[2]	Segment Name	Rupture Length (km)	Depth[3] (km)	Dip[4] (deg)	Sense of Slip[5]	Characteristic Magnitude[6]	Slip Rate (mm/yr) or Recurrenece Interval[7] (yrs)	Notes
CRSB North of Delta	1.0	Multisegment (0.1)	Mysterious Ridge	35	13 ± 2	25 W ± 5	R	6.8	1.0 (0.7) 3.5 (0.3)	Characterization revised from Working Group on California Earthquake Potential (1996) using data from O'Connell et al. (2001). Fault tip of Mysterious Ridge, Trout Creek, and Gordon Valley at depths of 7, 9, and 8 km, respectively. Segment lengths have an uncertainty of ± 5 km.
			Trout Creek + Gordon Valley	38	13 ± 2	25 W ± 10	R	6.8	0.5 (0.3) 1.25 (0.6) 2.0 (0.1)	
		Segmented (0.9)	Mysterious Ridge	35	13 ± 2	25 W ± 5	R	6.8	1.0 (0.7) 3.5 (0.3)	
			Trout Creek	20	13 ± 2	20 W ± 5	R	6.5	0.5 (0.3) 1.25 (0.6) 2.0 (0.1)	
			Gordon Valley	18	13 ± 2	30 W ± 5	R	6.5	0.5 (0.3) 1.25 (0.6) 2.0 (0.1)	
Maacama-Garberville	1.0	Unsegmented (1.0)	N/A	182	12	90	SS	7.5	9.0 ± 2.0	Cao et al. (2003) updated based on characterization of Field et al. (2013)
Vernalis	0.8	Floating Earthquake (1.0)	N/A	46	15 ± 3	70 W ± 10	RO	6.25 (0.2) 6.5 (0.4) 6.75 (0.4)	0.07 (0.3) 0.25 (0.4) 0.5 (0.3)	Quaternary activity of the Vernalis fault is inferred from the distribution of older Quaternary deposits (CDMG 1:25,000 San Jose quadrangle) that indicate differential uplift across the fault. Sterling (1992) describes stratigraphic and structural relationships imaged by seismic reflection data indicating "movement as recently as late Pliocene." The slip rate is estimated to be comparable to the estimated rate for the West Tracy fault.
West Tracy	1.0	Floating Earthquake (1.0)	N/A	12	14 ± 3	70 W ± 10	RO	6.25 (0.2) 6.5 (0.4) 6.75 (0.4)	0.07 (0.3) 0.25 (0.4) 0.5 (0.3)	Late Quaternary activity of the West Tracy fault is inferred from the presence of a surface scarp in probable Quaternary deposits at the northern end of the fault, and possible west-side-up displacement of Holocene peat deposits documented by geotechnical borings at Clifton Court Forebay (Unruh and Hitchcock, 2015). Long-term average separation rates across the fault measured from Neogene and Quaternary stratigraphic markers ranges between about 0.2-0.4 mm/yr. The distribution in slip rates captures the range in separation rates reported by Unruh and Hitchcock (2015), as well as uncertainty regarding fault dip (interpreted to be steep from analysis of seismic reflection profiles) and obliquity of slip on the structure.

[1] Probability of Activity: Independent seismic source (**M** ≥ 6.0) and repeated displacements in late-Quaternary or historical activity (1.0); Late Pleistocene or inferred association with historical seismicity (0.7); activity inferred from fault geometry considered likely to move under current tectonic regime (0.5). Other values reflect other fault-specific characteristics.

[2] Segmented and unsegmented faults allow for possible independent rupture for sections (or segments) of the fault. Weight assigned according to likelihood of occurrence of rupture scenario.

[3] Seismogenic depth. Unless otherwise stated, weights are 0.4 for the best estimate and 0.3 for the upper and lower bound estimates. A single depth value is weighted 1.0.

[4] Inclination of fault plane, measured from the horizontal. Dips are not varied unless otherwise stated. Weights are 0.4 for the best estimate and 0.3 for the upper and lower bound estimates.

[5] SS – strike-slip; R – reverse; RO – oblique-reverse.

[6] Unless otherwise stated, uncertainties in the best estimate magnitude are ± 0.3 magnitude unit. Weights are 0.2, 0.6, and 0.2 unless otherwise stated. A single magnitude value for floating events is weighted 1.0, unless otherwise noted. Magnitudes for ruptures are calculated from magnitude-area relationships described in Field et al. (2013), with weights HB08 (0.2), Shaw09 (0.4), and EllsB (0.4). Exceptions include floating earthquakes, which are not calculated from fault dimensions.

[7] Slip rate based on paleoseismic data or analogy to similar structures. Unless otherwise stated, weights are 0.2, 0.6, and 0.2

aecom.com